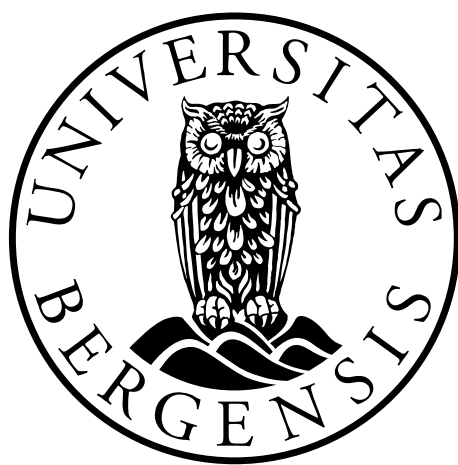

Development of a System for Microdosimetric Assessment of Clinical Proton Treatment Plans via Proton Energy Spectra

Hedda Johanne Askheim



Master Thesis in Medical Technology
Department of Physics and Technology
University of Bergen
June 2024

Acknowledgements

I am truly grateful for the opportunity to write my master thesis at the Department of Physics and Technology at the University of Bergen. I want to thank my supervisors Kristian S. Ytre-Hauge, Andreas T. Samnøy, Camilla H. Stokkevåg, and Helge Henjum for their support and guidance throughout the year.

In January, I got to participate and present my project at the MedFys conference in Oslo. These were some very exciting and inspiring days and it was an honor to be part of the medical physicist community.

Furthermore, this year would not have been the same without my fellow students at the reading hall. Thanks for all discussions, support, advice, all the chit-chat and lunch breaks. A specially thank you goes to Erlend for patiently helping me with FLUKA issues and all other questions.

Finally, I want to thank my friends Martine and Edna for providing me with great playlists with study music this year, Pernille for bringing coffee to reading sessions at the library, Ebba for letting me borrow her iPad and Mathias for always listening. My mum and dad also deserves a thank you for always believing in me and letting me choose freely without any pressure on career choices or results in school. I also want to thank my brother for inspiring me to follow a career path in science and technology.

Abstract

Purpose: The biological effectiveness of proton radiation depends on variables beyond the absorbed dose. In particular, the dose deposition on a micrometer scale may be relevant for subcellular structures such as DNA. Furthermore, the microdosimetric quantity *lineal energy* may represent the pattern of dose deposition in particle tracks more realistically compared to the more frequently used quantity *linear energy transfer*. Today, lineal energy is not available in clinical treatment planning systems. In this project the aim was to develop a system for calculating the lineal energy in proton therapy and use this to map the distribution of lineal energies in the brainstem of a pediatric brain tumor patient.

Methods: Proton treatment plans for a water phantom and a patient case were simulated in the FLUKA Monte Carlo code with scoring of the proton energy spectrum on a voxel-by-voxel basis. Via the proton energy spectrum the *dose-mean lineal energy* (y_d) was calculated with lookup tables, which were generated by interpolating between already existing lineal energy distributions from track structure simulations.

Results: Lookup tables converting between the proton energy and lineal energy was developed for energies 1-100 MeV and allowed for assessment of the lineal energy in volumes (sites) of size 10 nm – 20 μm . Entrance and peak value of y_d in the *spread-out Bragg peak* of water phantom for 10 (~ 18 and ~ 25 keV/ μm) and 100 nm site size (~ 6 and ~ 19 keV/ μm) agreed with values reported in similar studies. For the patient case, the y_d was found to increase from the target region to the brainstem.

Conclusions: A system for microdosimetric assessment of clinical proton treatment plans was developed enabling estimation of y_d in organs at risk. Although the lookup tables must be validated before this tool can be clinically applicable, this work provides a useful framework for further microdosimetric research aiming to find new links between the physics of the proton beam and the observed biological effect.

Table of contents

ACKNOWLEDGEMENTS.....	II
ABSTRACT	III
TABLE OF CONTENTS.....	IV
1. INTRODUCTION	1
1.1 PROJECT OBJECTIVES.....	2
2. THEORY	5
2.1 PROTON THERAPY	5
2.1.1 <i>Dosimetry</i>	5
2.1.2 <i>Interactions of proton with matter</i>	7
2.1.3 <i>Physical properties of a proton beam</i>	9
2.1.4 <i>Treatment planning in proton therapy</i>	12
2.2 RADIOBIOLOGY	14
2.3 MICRODOSIMETRY	19
2.3.2 <i>Microdosimetric quantities</i>	21
2.3.3 <i>Relationship between LET and lineal energy</i>	24
2.3.4 <i>The Microdosimetric-Kinetic Model</i>	26
2.4 MONTE CARLO METHOD AND ITS APPLICATION IN RADIOTHERAPY	27
2.4.1 <i>Monte Carlo radiation transport simulation</i>	28
3. METHODS.....	32
3.1 GENERATION OF LOOKUP TABLES FROM F(E) TO F(Y)	33
3.2 TREATMENT PLANNING	36
3.2.1 <i>Water phantom</i>	36
3.2.2 <i>Patient</i>	37
3.3 MC SIMULATIONS WITH FLUKA	39
3.3.1 <i>Defining the scoring grid</i>	39
3.3.2 <i>Energy spectra scoring in FLUKA</i>	41

3.3.3	<i>Dose and LETd scoring in FLUKA</i>	42
3.4	PROCESSING OF SIMULATION DATA IN PYTHON.....	44
3.4.1	<i>Calculating the energy spectra $f(E)$</i>	44
3.4.2	<i>Microdosimetric calculations</i>	45
4.	RESULTS	47
4.1	LOOKUP TABLES.....	47
4.1.1	<i>Interpolated $y_d(y)$ distributions</i>	47
4.1.2	<i>Interpolated y_D- and y_F - values</i>	53
4.2	WATER PHANTOM	58
4.2.1	<i>Energy spectra in water phantom</i>	58
4.2.2	<i>Microdosimetric calculations in water phantom</i>	61
4.3	PATIENT CASE	66
4.3.1	<i>Plan evaluation</i>	66
4.3.2	<i>Single field evaluation of dose, LETd and microdosimetry</i>	68
5.	DISCUSSION	74
5.1	APPLICABILITY OF THE DEVELOPED SYSTEM.....	74
5.1.1	<i>Limitations of the lookup tables</i>	74
5.1.2	<i>Limitations of the energy scoring</i>	79
5.1.3	<i>Approaches by others</i>	80
5.2	BIOLOGICAL RELEVANCE OF SITE SIZES	83
5.3	MACROSCOPIC (LETD) VERSUS MICRODOSIMETRIC (yD) QUANTITIES FOR RADIATION QUALITY	86
6.	CONCLUSIONS	90
	REFERENCES	91
	APPENDIX A – FLUSCW USER ROUTINE	95
	APPENDIX B – INTERPOLATED YD(Y)	96
	APPENDIX C – PYTHON SCRIPTS AND LOOKUP TABLES	97

Abbreviations

CH	Condensed H istory
CSDA	Continuous Slowing D own A pproximation
CT	Computed T omography
CTV	Clinical T arget V olume
DDF	D istal D ose F all-off
DSB	D ouble- S trand B reaks
DVH	D ose V olume H istogram
GTV	G ross T arget V olume
LET	L inear E nergy T ransfer
MC	M onte C arlo
MCS	M ultiple C oulomb S cattering
MKM	M icrodosimetric K inetic M odel
OAR	O rgan A t R isk
PBS	P encil B eam S canning
PDF	P robability D ensity F unction
PTV	P lanning T arget V olume
RBE	R elative B iological E ffectiveness
ROI	R egion O f I nterest
SOBP	S pread O ut B ragg P eak
SSB	S ingle- S trand B reaks
TPS	T reatment P lanning S ystem
TS	T rack S tructure
VH	V olume H istogram

1. Introduction

Proton therapy is a type of cancer treatment that offer the possibility of achieving an absorbed dose distribution which is highly conformed to the tumor volume, while sparing the surrounding normal tissue compared to conventional radiotherapy using photons. Facilities for proton therapy are being built worldwide and in 2025 two Norwegian proton therapy centers are planned to open. Predictions of the biological effect is crucial in proton therapy because we lack the empirical knowledge on the relationship between amount of radiation given to the patient and the clinical outcome, that we have in conventional radiotherapy after many years of clinical use. In contrast to photons, the effectiveness of protons depends on their energy and this complicates the calculation of the biological effect. Today a conversion factor to relate the doses of photon therapy to doses in proton therapy is used. This generic conversion factor, named the *relative biological effectiveness (RBE)*, was conservatively chosen in the 1970s in order to ensure sufficient dose coverage to the tumor[1, 2]. Even though the biological effectiveness of protons is known to vary within the treatment field[3-5], attempts of modelling the variable RBE with a sufficient clinical accuracy, is yet to succeed. This constant value is still used in clinics, possibly underestimating the dose to normal tissue located behind the tumor.

As the use of proton therapy is emerging around the world, the interest in estimating a variable RBE, is increasing. The *linear energy transfer (LET)*, a physical quantity describing the ionization density of a beam, has often been used as input when trying to model the variable biological effect within a proton treatment field. But as the LET depends on proton energy and the treatment field is composed of many different energies and the LET is based on the energy lost by the particle rather than the energy deposited, this quantity has limitations when trying to predict biological effect. Microdosimetry is a subdiscipline of radiological physics that was developed to try to

overcome the shortcoming of LET in describing biological effects on a subcellular level. It studies the spatial and temporal distribution of energy depositions at a microscopic level by recording these in small volumes termed *sites*. The size of the sites range from the order of several micrometers, resembling the size of a cell colony, and down to the size comparable to that of a DNA-segment in the nanometer scale. The aim is to find better links between the physics and the radiation-induced biological change in both cancer cells and normal tissues by taking the stochastic nature of radiation interaction into account.

The challenge of microdosimetry is that as it considers the randomness of particle interaction with matter, it requires measurements of each energy deposition by a proton track. In a clinical proton treatment field this is an unmanageable task, due to the enormous amount of energy depositions that contributes to the total dose. Today, advanced Monte Carlo (MC) track structure codes allow for obtaining the energy depositions computationally. In theory, one could recalculate the treatment plan with these track structure codes and estimate the lineal energies in the patient. But it is per today not possible nor practical to compute and store the microdosimetric spectra for each clinical voxel[6]. It is therefore of great interest to develop a system for efficient calculation of the lineal energy in a clinical proton treatment plan that does not require the storage of microdosimetric spectra in each voxel.

1.1 Project objectives

The objective of this project is to develop a system for calculating the microdosimetric quantity lineal energy for clinical proton therapy treatment plans. Today this quantity is not available when a treatment plan is made in the treatment planning system (TPS). In this project we want to map the distributions of microdosimetric quantities in an OAR and target volume to enable a more detailed assessment of the biological effectiveness of protons and its potential variation in

this. Further, expanding the plan evaluation regarding normal tissue toxicity from alone assessing the dose constraints for the OARs to include assessment of the spatial distribution of energy depositions in low-dose regions might improve treatment planning by giving further insight into which plan is saving the OAR the most. Furthermore, this system could eventually serve as a tool for calculating lineal energies for input to RBE models to enable a variable RBE along the treatment field.

Previous work at the department provided a mapping of microdosimetric properties of monoenergetic protons of different energies via MC simulations[7]. The lineal energies were found to significantly depend on the site size and the background for this current project was to investigate the significance this variation has in a clinical environment.

In this project it was an ambition to estimate the lineal energy in an OAR located posterior to the tumor, as several studies[5, 8-11] indicate that the RBE might exceed 1.1 in the distal dose falloff and thus implying a risk of elevated toxicity in normal tissues located directly behind the tumor. However, the clinical importance of an elevated RBE is unknown and the inconsistencies in the RBE reported for the same cell lines[10] hinders any consensus on the RBE-weighting factors at any depth in the dose profile. It is clear that more research on the clinical effect of the variable RBE is needed. Microdosimetric assessment of clinical proton beams is possibly a bridge to a further insight into the biological effect in proton therapy.

To achieve this, the following specific objectives was defined:

- Develop a method for scoring the energy spectra, $f(E)$, in small volumes when recalculating a proton treatment plan
- Generate lookup tables containing microdosimetric spectra for a range of clinical relevant proton energies

- Develop a method for using the calculated energy spectra in combination with the lookup tables to compute the lineal energy distribution, $f(y)$, in the volume
- Implement the method in a recalculation of a proton treatment plan for a pediatric brain tumor patient
- Investigate the calculated lineal energies in the brainstem and target volume and study the dependency on site size for the lineal energy

2. Theory

Chapter 2.3 is partly based on chapter 2 in the book of Lindborg et al. *Microdosimetry – Experimental Methods and Applications*[12].

2.1 Proton therapy

2.1.1 Dosimetry

To which extent ionizing radiation causes physical, chemical or biological changes in tissue, foremost depends on the energy deposited per unit mass of tissue, namely the *absorbed dose*, D [13]. It is a fundamental quantity in radiotherapy defined as the quotient of the energy imparted ΔE by ionizing radiation to the matter of mass Δm .

$$D = \frac{\Delta E}{\Delta m} \quad (2.1)$$

When cells experience radiation, a fraction of them will survive and the surviving fraction decreases with increasing absorbed dose. The fraction of cells surviving a specific absorbed dose differs between types of radiation[12]. Because of their higher ionization density, protons are more efficient than photons in killing cancer cells[14]. In treatment planning in proton therapy, the prescribed dose to tumor as well as the dose constraints to any organ at risk (OAR), are based on clinical experience with photon beams[15]. As it was an ambition to apply valuable clinical experience from the many years of photon therapy[1], the concept of relative biological effectiveness (RBE) was developed in the early days of proton therapy. It is the ratio of the two absorbed dose values, $D_{reference}$ and D_{proton} , that result in the same endpoint, the endpoint being any observed biological effect.

$$RBE = \frac{D_{reference}}{D_{proton}} \quad (2.2)$$

A constant RBE of 1.1 is currently assumed for clinical purposes as recommended by the International Commission on Radiation Units (ICRU)[16] and International Atomic Energy Agency (IAEA)[14].

The RBE depends on several physical and biophysical properties, one of them being the radiation quality of the beam, which is often quantified by the physical quantity linear energy transfer (LET). LET describes the ionization density of a charged particle and it is defined as the average energy loss per distance travelled dE/dx . As the energy loss of protons often results in a secondary charged particle that deposits energy elsewhere, the position of the energy loss and the position of the energy deposit is not identical. To compensate for this error, the *restricted LET* is defined as[13]:

$$LET_{\Delta} = \left(\frac{dE}{dx} \right)_{\Delta} \quad (2.3)$$

where the average energy loss per distance, $\frac{dE}{dx}$, only includes energy transfers below a specific limit Δ . A low value of Δ , gives a small distance between the position of the energy loss and the position of the energy deposits.

A clinical proton beam consists of particles with different energies and thus, there will be a spectrum of LET-values in the beam. The distribution in LET can be expressed either as a track length distribution, $t(L)$, or a dose distribution, $d(L)$. The averages of these distributions is used to quantify the radiation quality in a mixed particle field and in proton therapy the *dose average LET* (LET_d) is applied the most:

$$LET_d = \int_0^{\infty} Ld(L)dL \quad (2.4)$$

where $d(L)dL$ represents the fraction of the absorbed dose delivered between L and $L + dL$ [13].

2.1.2 Interactions of proton with matter

When traversing tissue, a proton loses energy by interacting with atomic nuclei and its electrons. The charge of the proton causes it to interact more with the medium it traverses than photons. The large mass of the proton makes it less affected by the medium and enables it to travel further into the body than the lighter electron can. Because the rest mass of the proton is 1832 times greater than the mass of an atomic electron, most protons travel in a nearly straight line[17].

Protons used in radiotherapy typically have kinetic energies between 3 and 300 MeV and they interact with matter in three ways[18]. The most frequent interaction is the electromagnetic (EM) collision with atomic electrons which slows the proton down and after numerous collisions it eventually stops. This interaction will be referred to as *stopping* in this thesis. Stopping is the main cause of dose deposition from protons[17]. When traversing a medium, the path of the protons may be scattered due to the repulsive force from the positively charged atomic nuclei. This concept is referred to as *multiple Coulomb scattering (MCS)*. The third way of interaction is the less frequent one and it is *nuclear reactions*. This is collisions with the nucleus as a whole or with elements of the nucleus like protons, neutrons or alpha particles.

Stopping

In the collision between the proton and the atomic electron, the proton loses energy because some of its energy is transferred to the electron. Whether a collision between a proton and an atomic electron will occur or not and the amount of energy transferred, is stochastic. The fluctuation in total energy loss is nevertheless small because the number of collisions per path length is relatively high. Thus, it makes sense to study the average energy loss of the proton beam per unit path length, dE/dx , called the *stopping power*. The stopping power for a charged particle heavier than an electron that is traversing a medium is described by the *Bethe Bloch formula*. With correction terms added, the stopping power is given as[19]:

$$-\frac{dE}{dx} = 2\pi N_a r_e^2 m_e c^2 \rho \frac{Z z^2}{A \beta^2} \left[\ln \left(\frac{2m_e \gamma^2 v^2 W_{max}}{I^2} \right) - 2\beta^2 - \delta - 2\frac{C}{Z} \right] \quad (2.5)$$

where N_a is Avogadro's number, r_e and m_e is the radius and mass of an electron, c is the speed of light in vacuum, ρ is the density of the absorbing material, Z is the atomic number of the absorbing material, A is the atomic weight of the absorbing material, z is the charge of the incoming particle, β is the relativistic speed of the incoming particle which is the speed of the incoming particle v divided by c ($\beta = \frac{v}{c}$), $\gamma = \frac{1}{\sqrt{1-\beta^2}}$, W_{max} is the maximum energy transfer in a single collision and I is the mean excitation potential of the absorbing medium. Finally δ and C is the density correction term and the shell correction term, respectively.

Multiple Coulomb Scattering

A proton passing nearby a nucleus will experience a repulsive Coulomb force that causes a small deflection in the protons path. Since the nucleus normally is heavier than the proton, the energy transferal in this elastic scattering is negligible. This scattering interaction is irrelevant individually, and this phenomena of MCS is therefore studied from a macroscopic view point. The net effect of the many small deflections of all the protons present in a beam, is a lateral spread of the beam that increases with depth. In proton therapy, MCS affects the spatial distribution of dose in the patient and needs to be taken into account in treatment planning. Furthermore, MCS is utilized in the design of the treatment head to make the beam laterally large enough to cover the tumor volume[17].

Nuclear reactions

A high-energetic proton can overcome the Coulomb barrier and interact with an atomic nucleus through the nuclear force. In this non-elastic collision, the proton can be absorbed by the nucleus and a neutron is ejected. If the proton is not absorbed, it transfers some of its energy to the nucleus, leaving it in an excited state and then

scatters. Proton-induced nuclear reactions can cause secondary particles in form of energetic protons, deuterons or heavier ions. The main effect of nuclear reactions in the context of a therapeutic proton beam, is a small decrease in absorbed dose due to the removal of primary protons[17]. However, this reduction in dose is compensated by the production of secondary particles. According to ICRU, secondary protons contribute to approximately 10 % of the absorbed dose in a high-energetic proton beam[20]. The theory of nuclear interactions are complex and largely phenomenological, in contrast to the well-described theory for the two other main proton interactions, stopping and MCS. Luckily, these interactions happens relatively infrequent. Burigo[21] found that in a 152.6 MeV proton beam, approximately 20% of the protons participated in nuclear reactions before they stopped. Therefore, ignoring nuclear interactions when computing the evolution of a primary proton can give a fair approximation[18].

2.1.3 Physical properties of a proton beam

The Bethe-Bloch formula in Equation (2.5) gives the inverse relationship between the traversing particles velocity (energy) and its linear energy loss. As the particle is slowed down, it will deposit more energy per unit length travelled. This relationship explains the shape of the dose-depth curve for a proton beam with the characteristic *Bragg peak*, which can be seen in Figure 2.1. This sharp dose fall-off behind the point of maximum energy-deposition, is the physical property of proton beams which enables a highly conformed dose to the tumor volume while sparing the surrounding normal tissue. The region behind the Bragg peak is often referred to as the *distal dose fall-off* (DDF).

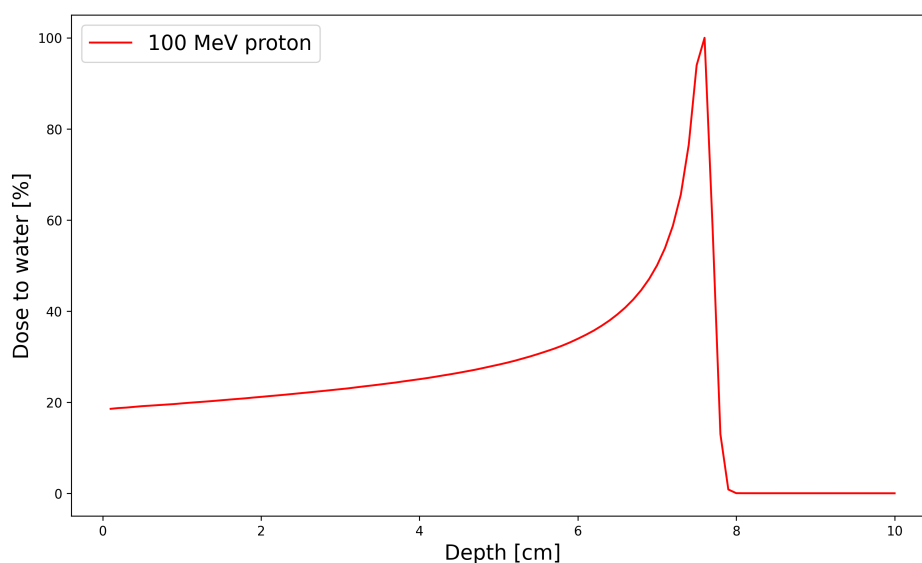


Figure 2.1: Dose-depth profile of a 100 MeV proton beam consisting of 1 million primaries traversing water simulated in FLUKA. The Bragg peak is located at ~ 7.7 cm.

The position of the Bragg peak in a water phantom is determined by the incident energy of the proton beam. The proton beam in Figure 2.1 is simulated by 1 million primary protons and in any proton beam, there will be a distribution of path lengths among the protons even though they all have the same initial energy. This concept is known as *range straggling*. It is caused by the fluctuation in the amount of energy lost by the proton in each collision and the fluctuation in the number of collisions per unit path length. Therefore, tables converting between proton energy and range applies to a proton beam and not individual protons, as range is an average quantity which becomes valid in a proton beam where the statistics are high and the *continuous slowing down approximation* (CSDA) given by the Bethe-Bloch equation is valid. Range straggling is visible at the end of the dose-depth curve for a proton beam as a small tail after the Bragg peak before the dose falls completely to zero.

Furthermore, the Bethe-Bloch formula describes how the stopping power of a particle is dependent on its charge (z). The stopping power is proportional to z^2 and therefore heavier ions than protons, e.g. carbon ions in carbon therapy, will have a much larger

stopping power than protons. For this reason, carbon ions have a shorter range than protons with the same energy.

Additionally, the stopping power increases with increasing density (ρ) of the material it is traversing. The density of the tissue that a clinical proton beam is traversing varies with tissue type given bones have a much higher density than air cavities within the body, such as in the lungs. Water is seen as a good tissue-equivalent material as it mimics the properties of tissue when considering energy loss, MCS and nuclear interactions, and is therefore used as phantom material for dose and range calculations[17].

The *pristine* Bragg peak, i.e. the dose-depth curve from a monoenergetic beam, is too narrow to cover the whole target volume in clinical cases. In order to widen the treatment depth range and ensure a homogenous coverage of the target volume, several Bragg peaks placed at different depths are superimposed. By varying the energy and thus the range of the proton beam during the irradiation of the patient, the *Spread-out Bragg peak* (SOBP) is created[22]. The SOBP delivers a homogenous dose to the target and it preserves the sharp dose fall, of enabling sparing of normal tissue located behind the tumor. However, the total entrance dose is increased with a SOBP compared to a monoenergetic proton beam.

Secondary electrons

As a proton beam traverses tissue, rays of secondary electrons, so called *delta rays*, will appear along its path. These arise from stopping interactions described earlier where a proton and an atomic electron collide. Consequently, the electron is excited from its original state, and if a sufficient amount of energy is transferred in the collision, the atom becomes ionized. The ejected electron can have sufficient energy to perform further ionizations in the tissue, creating a cascade of ionizing events. Delta rays are highly relevant when studying proton therapy as they contribute substantially to the production of biological damage[23, 24]. Liamsuwan et al.[25]

found when simulating a 160 MeV proton track in water using Monte Carlo track structure methods, that the secondary electrons contributed to more than 70 % of the total absorbed dose at any depth.

2.1.4 Treatment planning in proton therapy

The aim of radiotherapy is to deliver a high enough dose in order to kill the tumor cells while at the same time limiting the dose to the surrounding normal tissue to prevent severe damage either in the form of acute effects or effects that will occur later in the patient's life, such as second primary cancer which is the most severe form of late effect after a cancer treatment[26]. *The therapeutic window*, illustrated in Figure 2.2, is a concept in radiotherapy describing this tight gap between the dose needed to ensure a high probability of killing the cancer cells (tumor control probability TCP) and the dose that gives a high probability of severe damage to normal tissue (normal tissue complication probability NTCP).

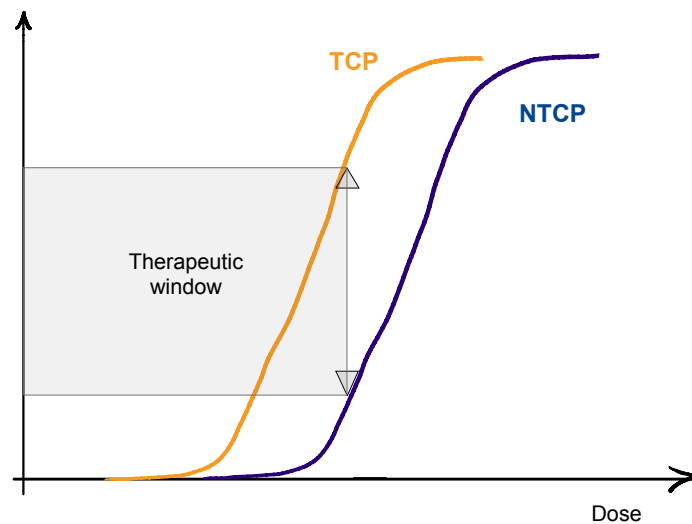


Figure 2.2: The therapeutic window is a concept in radiotherapy illustrating the gap between tumor control probability (TCP) and normal tissue complication probability (NTCP).

Planning is a critical step in all radiotherapies and defining the regions in which the treatment is to be delivered, is fundamental. Several helping structures, illustrated in Figure 2.3, are delineated in the CT-images of the patient, in order to guide the

treatment planning. Around the macroscopic identifiable tumor, the gross tumor volume (GTV), a clinical target volume (CTV) is contoured to include areas where there is risk of tumor spread. An extra margin, the planning target volume (PTV), is added to account for several uncertainties. Additionally, any OARs need to be segmented.

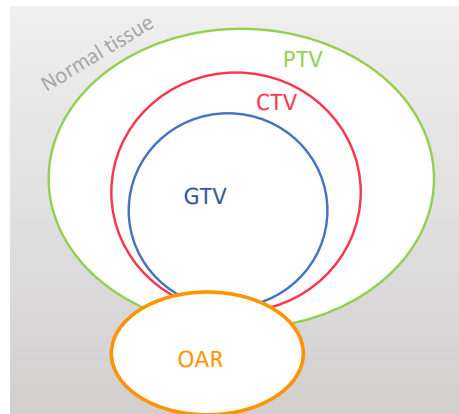


Figure 2.3: Illustration of the helping structures GTV, CTV, PTV and OAR, applied in treatment planning.

Pencil beam scanning

Pencil beam scanning (PBS) is the most common proton delivery technique as it is considered the most flexible method[18]. In PBS, the proton beam can be directly sent into the patient without the need for interacting with energy modulation devices. The dose is delivered at one depth at a time, known as a layer, and magnets are used to steer the thin pencil beam across the target to reach the full lateral extent of the target. After one layer is covered, the beam energy is altered to reach another depth. As there is no need for energy modulation devices with this technique, the beam can efficiently be altered and in theory deposit dose at any desired position within the patient.

Robust optimization

The weight (the relative number of protons delivered by each spot) of each pencil beam needed to obtain the desired dose distribution, is typically computed by an

optimization algorithm within the treatment planning system(TPS). Before running the optimization algorithm, the planner has to choose the number of fields and the angle of these[27]. Additionally, in inverse planning, the plan objectives, including the upper and lower dose limits to target and the upper dose limits for OARs, needs to be defined prior to optimization. The algorithm is based on a penalty function which scores how far the current dose distribution is from meeting the plan objectives.

The treatment plan needs to be robust, i.e. designed in such a way that light deviations from the plan due to various uncertainties during treatment delivery will not affect the quality of treatment outcome[18]. Today it is common practice in many proton therapy clinics to account for the uncertainties by applying *robust optimization* of the dose to CTV, discarding the practice of the PTV where the uncertainties are embedded in the plan via margins. In robust optimization the optimization algorithm investigates several scenarios with possible combinations of setup and range uncertainties to create a plan that would even in the worst-case scenario give an acceptable dose distribution.

2.2 Radiobiology

The principal target for radiotherapy is the DNA of the cancer cells. Even though all molecules in a cell is affected by ionizing radiation, it is DNA damage, which occurs mainly in the form of single- (SSB) or double-strand breaks (DSB), that is crucial for mutation induction and killing of cells for most cell types[18, 28]. While the vast majority of SSBs are repaired by the cell, a DSB is a non-repairable damage possibly leading to cell death and therefore the most relevant biological damage in radiobiology. In order to annihilate cancer cells, enough energy must be deposited in the DNA so that a sufficient number of DSBs occurs. A higher ionization density, increases the probability of harming the DNA.

Radiation can act on the DNA either indirectly by ionizing water molecules in the cell and liberating highly reactive radicals, or via direct deposition of energy. Low LET radiation (such as X-rays, gamma-rays and beta-particles), and high LET radiation (such as alpha-particles and neutrons) can both cause DNA damage through these interaction channels[29] it is the low LET radiation that do indirect damage and the high LET radiation that causes direct damage[30]. In a proton treatment field, the delta rays play an important role in inducing biological damage, as outlined in 2.2.2. The energy of the delta electrons is typically much lower than the electrons produced in photon beams[18] and thus the range of the delta electrons is shorter, and ionizations can occur more densely. The spatial distribution of DNA damage is important, as clusters of strand breaks that are more concentrated in space seems to hinder the repair mechanisms of the cell[31]. This means that even if a photon beam and a proton beam might cause the same number of DSB per unit dose, the distribution of the damage will be more densely for the proton beam and hence the biological effect per dose is higher for protons than photons.

Linear Quadratic model

The linear quadratic (LQ) model is a dose-response model and it is one of the key tools in radiation biology because it provides a simple relationship between cell survival and delivered dose[32]. The fraction of surviving cells, SF, after absorbing a dose D is described by the LQ model as:

$$SF(D) = e^{-(\alpha D + \beta D^2)} \quad (2.6)$$

where α and β are the linear and quadratic survival parameters, representing DNA damage through single hit and multiple hit, respectively. At low doses a linear relationship between dose and SF is seen and α gives the initial slope of the cell surviving curve[12].

Figure 2.4 displays cell survival curves from work by Chaudhary et al.[33], where human glioma cells were irradiated with a photon beam and proton beams with various LET. The cells were irradiated with the same proton beam, placed at different positions along the Bragg curve of the proton beam and thus experiencing different levels of LET. The figure illustrates how higher levels of dose is needed to kill the same fraction of cells with low LET radiation as compared to high LET radiation. As protons are more densely ionizing than photons, the cell survival curve based on the LQ model will be steeper for proton therapy than photon therapy.

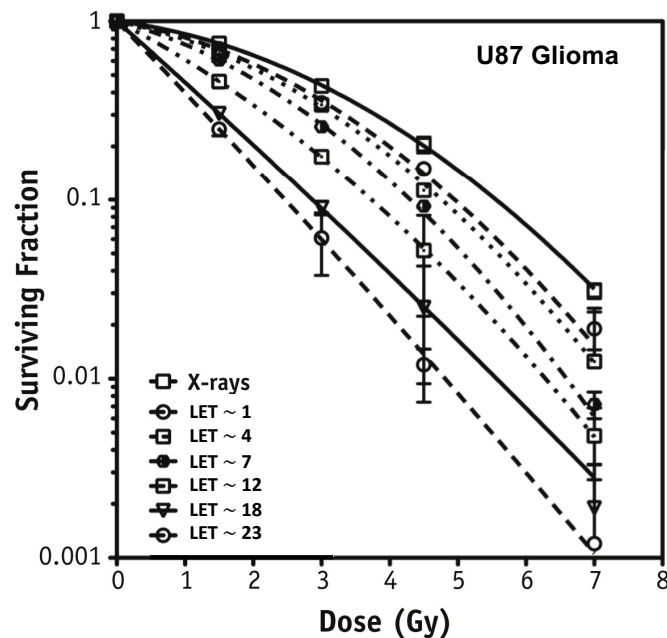


Figure 2.4: Survival curves for human glioma cells (U87) irradiated with x-rays (photons) and proton beams with various levels of LET. The figure is reprinted (edited) from Chaudhary et al. (2014)[33] with permission from Elsevier.

The radiosensitivity differs among tissue types and the surviving fraction of cells can therefore vary if two cell cultures of different cell type are irradiated with the same beam. The α/β ratio is often used as a measure of radiosensitivity. It is found by drawing a line with the initial slope α in the cell survival curve and locate the dose where the linear and quadratic components are equal. Tumor tissue is in general

considered to have a higher α/β ratio than normal tissues. This is exploited in fractionation of treatment delivery as the normal tissue will to a larger extent than the tumor cells repair themselves between the fractions.

RBE-models in proton therapy

To account for the potential effect of a variable RBE along the proton treatment field, numerous RBE models for proton therapy have been developed. As summarized by Rørvik et al.[34], the majority of suggested models are phenomenological models, meaning that they are based on empirical data from *in vitro* proton irradiation of various cell lines fitted to the LQ model.

Rørvik et al. investigated the differences between a large collection of phenomenological RBE-models. They found considerable differences between the input data to the models and assumptions made in the models. Resultingly the models gives different RBE estimates and RBE-weighted doses as illustrated in Figure 2.5.

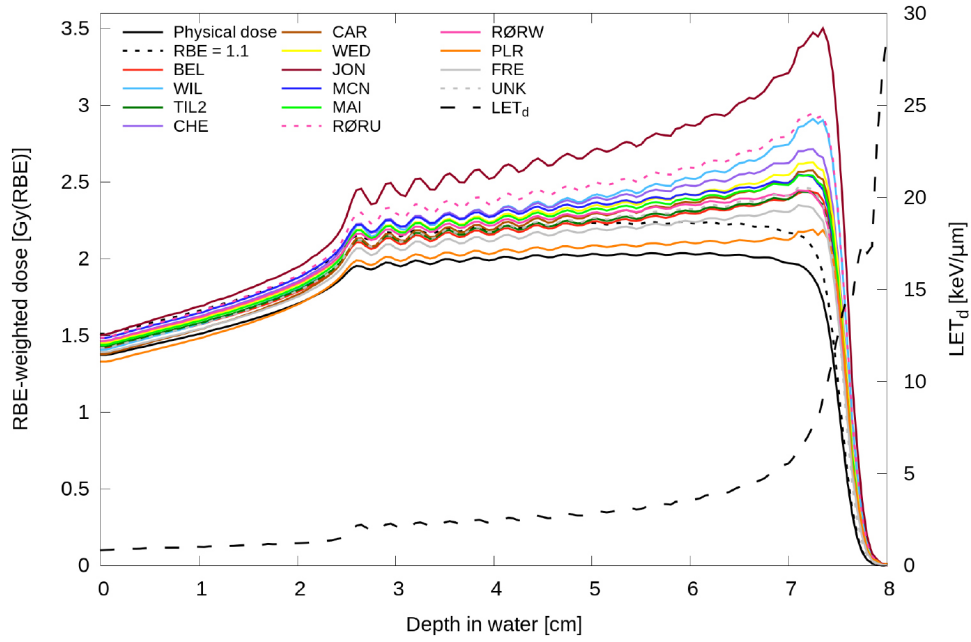


Figure 2.5: Depth dose distribution of a SOBP in water with model estimates in color curves. Uppermost curves represent the RBE-weighted dose given by the left axis, while the black dashed curve represents the LET_d given by the right axis. $(\alpha/\beta)_x = 3.67$ Gy was applied in the calculations. The figure is reprinted from Rørvik et al. (2018)[34] with permission from IOP publishing.

In general the phenomenological models RBE as a function of the LQ model parameters and physical proton dose[34]:

$$RBE[D_p, \alpha, \alpha_x, \beta, \beta_x] = \frac{1}{2D_p} \left(\sqrt{\left(\frac{\alpha_x}{\beta_x}\right)^2 + 4D_p \frac{\alpha_x}{\beta_x} \frac{\alpha}{\alpha_x} + 4D_p^2 \frac{\beta}{\beta_x} - \frac{\alpha_x}{\beta_x}} \right) \quad (2.7)$$

where D_p is the physical dose deposited by protons per fraction, α and β are the radiosensitivity parameters from the LQ model for protons, and α_x and β_x are the LQ parameters for the reference photon radiation.

The increase in RBE towards the end of the SOBP, which is seen for all the curves in Figure 2.5, except the curve of $RBE = 1.1$, is due to the dependency of RBE on LET. The unrestricted LET, LET_∞ , is simply the stopping power and as described by the Bethe Bloch equation in Equation (2.5), the stopping power increases before the

proton stops. Thus, the LET increases in the distal end of a proton beam, as seen in Figure 2.5. This also explains why the cells placed along different positions in the Bragg curve in the study by Chaudhary et al.[33], experienced different levels of LET.

Rørvik et al. found that the differences in the definitions of the radiosensitivity parameters, α and β , causes the different RBE estimates between the models. As the models are derived by fitting cell survival data, the size of data included will have an impact on the derived model. Furthermore, most phenomenological models use LET_d as a measure of beam radiation quality but their weighting of the LET_d differs.

2.3 Microdosimetry

The fundamental idea underlying microdosimetry is to explore whether taking the stochastic nature of radiation interaction into account will improve our understanding of the relationship between physics and results observed in radiation biology and radiotherapy.

The sites concept

Microdosimetry concerns the measurement and study of the stochastic energy deposition by charged particles in volumes of microscopic size called *sites*. A site is a region with a user defined shape and size, in which the distribution of energy depositions by particles are studied[35]. When passing through matter, a particle interacts with atoms at *transfer points*. In Figure 2.6 the dashed lines represents transfer points and the figure illustrates the difference between a *single event* and a *multi-event*. If all transfer points are correlated, meaning that they originate from the same primary particle or its secondaries, it is a single event. If a site is influenced by several particle tracks, it is a multi-event.

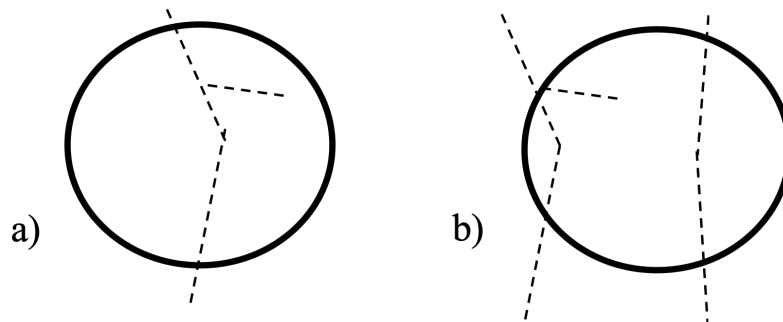


Figure 2.6: Illustration of a single event in a) and a multi-event in b). The dashed lines represent transfer points. The figure is redrawn from Lindborg (2017)[12].

Which site sizes most relevant for describing biological effects of radiation in tissue has been a constant theme in the field of microdosimetry. It is well established in radiobiology that the cell nucleus is a principal target for radiation injury as it contains essentially all the DNA in the cell. A cylinder with a 2 nm diameter has therefore often been used to imitate the shape of the DNA molecule[36] and site sizes in the range 3-10 nm[29] are viewed as relevant targets for describing DNA damage by radiation tracks. However, Goodhead[29] points out in his review on the topic, that in recent years so-called 'non-targeted' effects have gained increasing attention. These are processes where biological effects are observed in a biological system separated from the immediate action of the radiation tracks, possibly due to inter-cellular signaling. An example is genomic instability in parts of the genome that were not directly damaged by the radiation and which becomes visible in subsequent generations of derived cells. While processes of radiation-induced DNA damage are now relatively well understood and their biological relevance is clear, less is understood about these non-targeted effects both in terms of how they are initiated and how they propagate in space and time[29]. Furthermore, for normal tissue toxicity, the damage to the tissue microenvironment from radiation-induced inflammatory responses play an important role[3]. Considering all this, it is clear that site sizes resembling whole cells and populations of cells must also be considered when modelling biological effect of radiation. Thus, in addition to the subcellular site

sizes in the nanometer scale, possibly well suited for describing the clustering of DNA damage, site sizes in the micrometer range are also relevant in microdosimetry to account for intercellular signaling.

2.3.2 Microdosimetric quantities

The quantities in microdosimetry are not meant to replace existing macroscopic quantities in conventional dosimetry, but to complement them with information about the probability for the deposited energy to reach a certain value within a specified volume when an ionizing particle interacts with the volume[12].

While the absorbed dose is merely the average (macroscopic) energy absorption per unit mass, most of the biological effects of radiation in fact depends on the spatial and temporal distribution of single energy depositions, i.e. the microscopic pattern of energy deposition[28]. The most fundamental quantity in microdosimetry is the *energy deposited* in a single interaction i .

$$\varepsilon_i = E_{in} - E_{out} + Q \quad (2.8)$$

where E_{in} is the energy of the particle arriving the transfer point and E_{out} is the sum of energies of all particles leaving the transfer point. Both energies exclude rest energy and Q is any change in rest energy of the nucleus or the elementary particles involved in the interaction.

The *energy imparted*, ε , to the matter in a given volume is the sum of all energy deposits in the volume:

$$\varepsilon = \sum_i \varepsilon_i \quad (2.9)$$

The *specific energy*, z , is the energy imparted in a volume divided by the mass of that volume:

$$z = \frac{\varepsilon}{m} \quad (2.10)$$

Both ε and z are independent on the number of events involved.

To illustrate the presented quantities, Figure 2.7 shows a volume of mass m where the energy deposits $\varepsilon_1, \varepsilon_2$ and ε_3 has taken place at three transfer points. Energy imparted to this volume is $\varepsilon = \varepsilon_1 + \varepsilon_2 + \varepsilon_3$ and specific energy is $z = (\varepsilon_1 + \varepsilon_2 + \varepsilon_3)/m$.

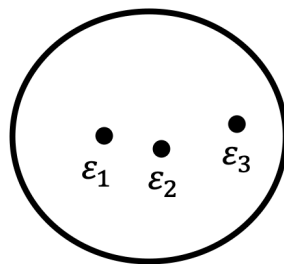


Figure 2.7: Representation of a mass m with mean chord length \bar{l} where one or several ionizing particle has performed three energy deposits $\varepsilon_1, \varepsilon_2$ and ε_3 . The figure is redrawn from Lindborg (2017)[12].

Specific energy has the same unit as absorbed dose, $\text{Gy} = \text{J/kg}$. But while absorbed dose, D , is a deterministic quantity, specific energy is a stochastic one. This means that two identical microscopic sites within the same homogenous radiation field will not have the same specific energy. By taking the mean of a specific energy distribution within a region of several sites, one attains the absorbed dose for this region:

$$D = \bar{z} \quad (2.11)$$

The microdosimetric equivalent to the LET is the lineal energy, y . It is the quotient of the energy imparted by a single event to a site, ε , and the *mean chord length* through that volume, \bar{l} :

$$y = \frac{\varepsilon}{\bar{l}} \quad (2.12)$$

The choice of route through the site is random, and therefore an event will have a number of possible chord lengths l . The average length of these chords is represented by the parameter \bar{l} [37].

Probability density functions (PDFs) are necessary in order to describe the stochastic variables of microdosimetry, such as the lineal energy. If one were to set up a microdosimetric experiment and the lineal energy were measured several times, it would give a frequency function, $f(y)$, describing the probability of the different lineal energies in that specific experiment. $f(y)$ is typically termed the *lineal energy distribution*. The shape of $f(y)$ would be the same as the distribution of energy depositions, since the lineal energy depends on the stochastic energy depositions. The expectation value of $f(y)$, is the *frequency-mean lineal energy* \bar{y}_F :

$$\bar{y}_F = \int_0^{\infty} yf(y) dy \quad (2.13)$$

It is often useful to see how the different lineal energies contribute to the absorbed dose. Since the high lineal energy events contributes more to the dose than the low linear energy events, the high linear energy events are more important when considering the dose. For this reason, the dose distribution $d(y)$ needs to be defined:

$$d(y) = \frac{y}{\bar{y}_F} f(y) \quad (2.14)$$

The *dose-mean lineal energy*, \bar{y}_D , is the expected value from $d(y)$:

$$\bar{y}_D = \frac{1}{\bar{y}_F} \int_0^{\infty} y^2 f(y) dy \quad (2.15)$$

The expectation values \bar{y}_D and \bar{y}_F are non-stochastic values.

Figure 2.8 (left) illustrates how the $d(y)$ shifts towards higher lineal energies than $f(y)$.

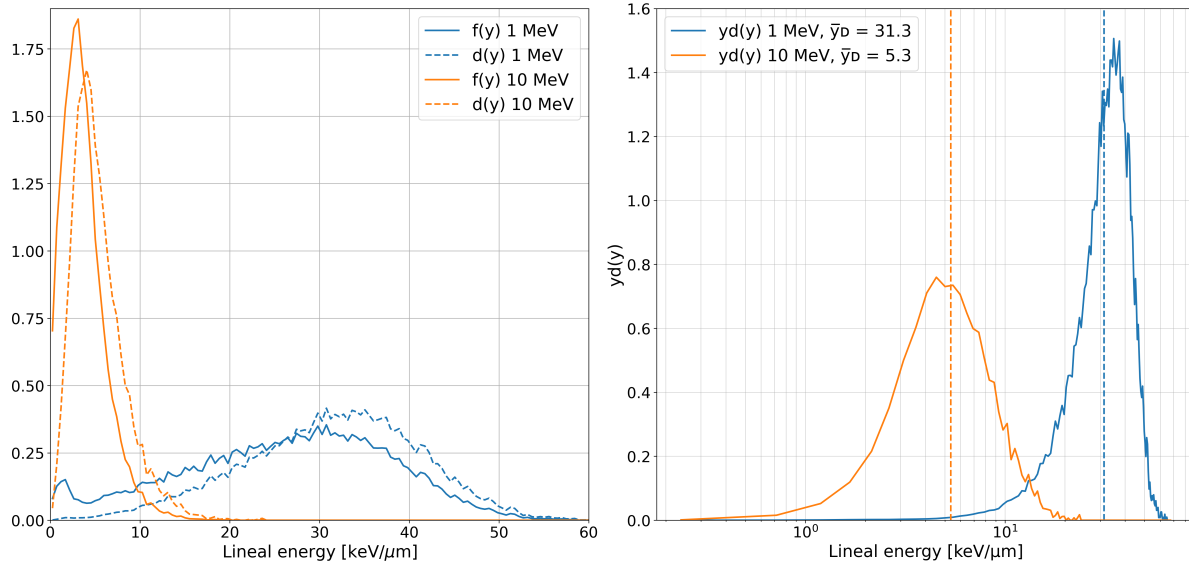


Figure 2.8: $f(y)$, $d(y)$ (left), $yd(y)$ and \bar{y}_D (right) for 1 and 10 MeV proton track in a $1 \mu\text{m}$ site. Plotted with simulation data from Geant4 DNA from Folkedal[7].

Furthermore, the figure exemplifies that the spread in the measured lineal energies can be large between experiments and therefore it is often more practical to display the results as a so-called $yd(y)$ dose distribution. This is often referred to as the microdosimetric spectra as it is the standard way of presenting lineal energies. This is a semi-logarithmic representation that is useful because the area under the curve defined by a specific range of lineal energy values represents the dose delivered by events in that specific lineal energy range[12]. Thus, equal areas under the curve represents equal contributions to the absorbed dose.

2.3.3 Relationship between LET and lineal energy

It is relevant to discuss the relationship between LET and y since they are both quantities that characterizes particle tracks and are measures of radiation quality. LET is useful for defining the radiation quality of a radiation field itself, but when radiation quality in a small volume needs to be characterized, y is useful. We can

expect LET and y to be numerically close in large volumes, because it is more likely that the energy is completely deposited inside a large sphere than in a small one in the nanometer scale. Figure 2.9 illustrates how the stochastic particle path through the sphere is pivotal for the amount of energy imparted in the volume.

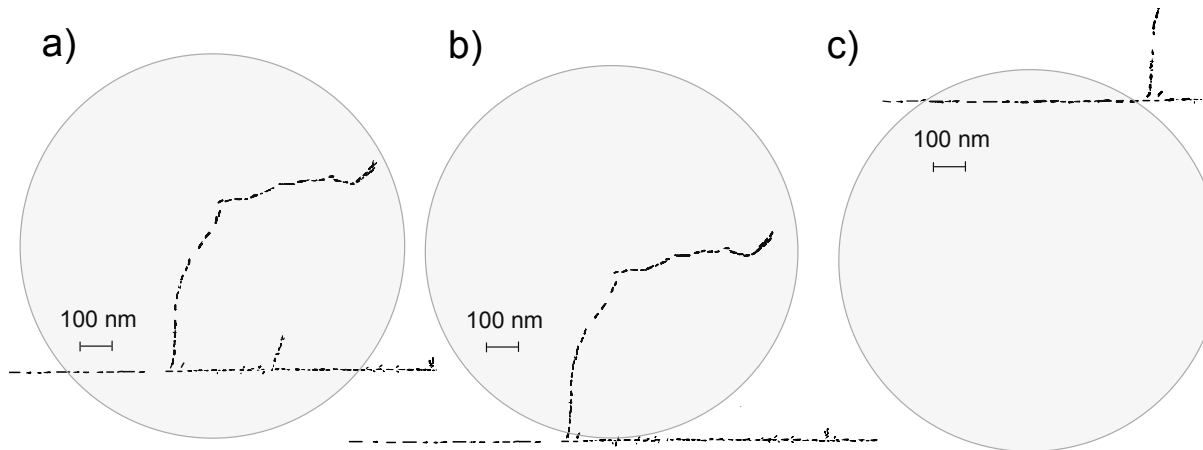


Figure 2.9: Sketch of a particle track in a 300 MeV carbon beam passing through a sphere with a diameter of approximately $1 \mu\text{m}$. The figures a), b) and c) illustrate three different paths the particle might take. The horizontal line is energy depositions by the primary particles and the tracks outside this line are delta rays. The figure is redrawn from Lindborg (2017)[12].

In Figure 2.9a), both the main particle track and some delta electrons deposits energy. In Figure 2.9b), only the delta electrons contribute to the energy deposition because the main track is passing outside the sphere. The main track in Figure 2.9c) is passing through the sphere with a short chord length and no delta rays are located inside the sphere. Little energy is therefore deposited in this situation. These particle tracks are simulated for carbon ions. Although protons do not deposit energy as densely as carbon ions, the figures serves to illustrate how the stochastic particle paths results in various amounts of energy deposited in the site and consequently variations in y .

The number of collisions between the incoming particle and the medium for a given chord length is Poisson distributed and the expectation value is proportional to the LET of the radiation and the mean chord length[12]. In a collision it is more likely

with a small energy transferal than a large one and thus, when many collisions occur, extreme values of energy transferal in a single collision become less influential. Consequently the \bar{y}_D in larger site sizes will be less extreme.

When the site size is decreased, the delta electrons will become more important, as gradually more volumes are only intercepted by delta electrons. This is illustrated in Figure 2.10 with 100 nm sites. In a clinical proton beam, the delta electrons will often have a larger lineal energy than the protons themselves, as most of the energy imparted in a high-energetic proton beam is due to secondary particles, as discussed in chapter 2.1.3. Hence the \bar{y}_D tends to become increasingly larger than the LET as the volume of the site decreases.

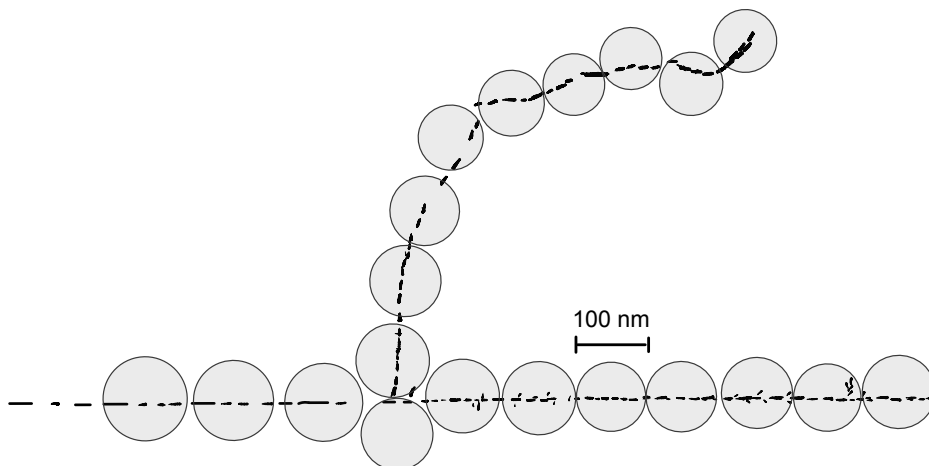


Figure 2.10: Sketch of a particle track in a 300 MeV carbon beam. Spheres of approximately 100 nm cover the track. In 8 of the 19 spheres, energy is deposited by delta electrons. The figure is redrawn from Lindborg (2017)[12].

2.3.4 The Microdosimetric-Kinetic Model

In addition to the phenomenological models described in chapter 2.2, microdosimetry-based models for predicting RBE is also of great interest among researchers today in the quest to estimate the variable RBE.

One such model, which is applied in carbon-ion therapy clinics in Japan[38], is the *microdosimetric-kinetic model* (MKM). It was initially proposed by Hawkins in 1994[39] and has then been explored and extended till nowadays[40]. The model provides a quantitative explanation for the relation between RBE and LET for reproductive cell death in mammalian cells[12].

The MKM assumes that within each cell there is a sensitive nucleus volume that contains the DNA[41]. The nucleus is divided into hundreds of sub-units called domains with a diameter in the range 0.5 to 1 μm . Radiation can give rise to two different types of DNA damages, according to MKM, and they are named type I and type II. Type I lesions are lethal lesions that cannot be repaired and are typically thought of as complex double strand breaks (DSB) in the DNA. Type II, so called potentially-lethal lesions, are lesions that can be repaired or end up as lethal lesions by spontaneous conversion or binary combination with another type II lesion. A pair of type II lesions can combine to form a type I lesion only if they are created in the same domain. The whole cell is considered to be dead if at least one domain contains a lethal lesion[40].

2.4 Monte Carlo method and its application in radiotherapy

Monte Carlo (MC) can be defined as a numerical method to solve equations or to calculate integrals based on random number sampling[42]. The technique was utilized for the first time in the field of radiotherapy in the late 1970s, and since then it has become an essential part of research and treatment planning[42]. MC method is applicable to particle physics because of its ability to describe a system with many coupled degrees of freedom, as an interacting particle system is. Through simulations of the systems microscopic particle interactions, the MC method provides a solution to the macroscopic system, for example the dose to a volume in the patient.

Additionally, performing real life experiments with actual particle beams requires that you have a particle accelerator available and is time-consuming and expensive. Therefore MC simulations is a great tool for researchers and for dosimetric calculations in treatment planning systems.

Furthermore, MC simulations have been important for the evolution of microdosimetry by enabling the study of energy depositions in the nanometer scale. While experimental measurement techniques for microscopic volumes are well established, techniques for measuring energy depositions in nanometers volumes are few[12] and MC simulations is an essential tool in the field of microdosimetry especially when considering DNA-sized sites.

2.4.1 Monte Carlo radiation transport simulation

A MC radiation transport simulation starts with a primary particle sampled from a source distribution[18]. The destiny of this primary particle, depends on the beam angle, the patient anatomy given by CT images and the properties of the materials included in the simulation, which are characterized by their physical properties such as electron density and mean excitation energy[18]. Using differential cross sections, the distance to the first interaction, the type of interaction, secondary particle energies and scattering angles are determined. These steps are repeated until the simulation is stopped when all particles has left the simulation geometry or their kinetic energies has fallen below a user-defined minimum. The tracking of one primary particle, including its secondary particles until their complete absorption, is termed a particle history.

During MC simulation, huge sequences of random numbers must be generated in order to solve the complex problems[42]. These random numbers are generated based on probability density functions (PDFs). A PDF is a formula, table or graph that provides the probability associated with each value of a random variable. At each step

of the particle transport through the geometry, different PDFs represent the probability of their associated physics interactions and their outcome[18]. The generated random numbers should more precisely be denoted pseudorandom numbers due to the fact that output from any program is by definition predictable and thus not truly random. Pseudorandom numbers appears to be statistically random although they have been produced by a deterministic and repeatable process.

Condensed History approach and track structure models

There are two main categories of MC models in radiation transport simulation, condensed-history (CH) and track structure (TS) models. Whereas TS models simulates particle transport collision-by-collision, CH models is an alternative approach allowing for more efficient simulations. CH models are especially applicable for particle transport simulation as the simulation time for one particle history is much longer for a charged particle than for a photon. While the mean free path length of a photon is typically 10 cm in human tissue[42], protons undergo a very large number of interactions for radiotherapy energies. Additionally, many of the photons in a therapeutic beam pass through the body. Whereas in proton therapy the protons stop in the body, desirably in the cancerous tumor. Most of the interactions along a proton track is inelastic collisions with atomic electrons where the proton lose a small amount of its energy and continues to travel in a nearly straight line. These properties allows us to group many of these interactions into one CH step. In contrast to reality, a particle moves in a straight line during a CH step. Only at the end of the step the direction of the particle is changed due to multiple scattering as shown in Figure 2.11. The simplification that the particle moves in a straight line, causes an overestimation of the particle range as well as a transversal displacement. To account for these problems CH algorithms usually include a path length correction algorithm and a transverse displacement algorithm.

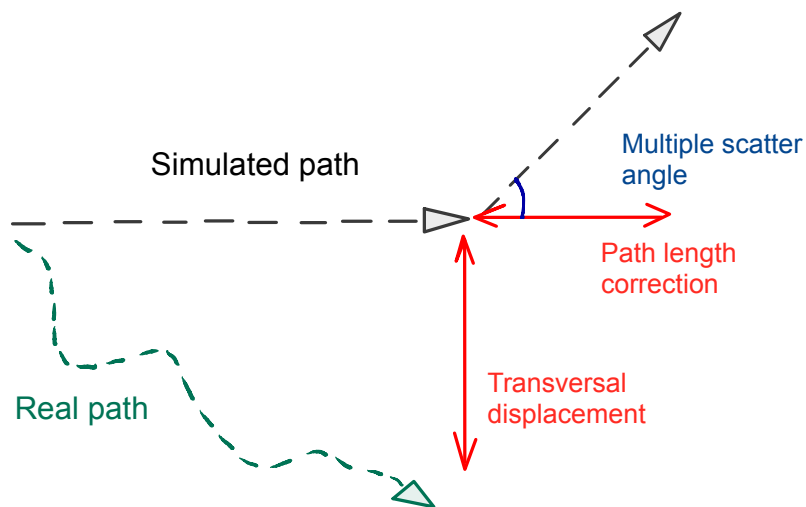


Figure 2.11: The black dashed line is the simulated path where the CH technique is used. The green dashed line is the possible real path or the path simulated with the analogue technique. The red lines shows how the CH technique overestimates the path length. Figure is redrawn from Seco et al. (2013)[42].

Explicit tracking of electrons might not be crucial for dose calculations on a typical CT-grid, but simulating low energetic particle tracks, as delta-tracks, is essential to study microdosimetric dose depositions which is postulated to be relevant for biological modelling in particle therapy[25, 43, 44]. For this reason, TS codes as Geant4 DNA has been developed. This code specializes on simulating low-energy particle tracks with a collision-by-collision approach. Since its release in 2007, Geant4 DNA has become an important and much utilized tool in radiotherapy and radiobiology research and it has been benchmarked against other TS MC codes and, where available, against experimental data[43].

FLUKA

FLUKA[45] is a general-purpose MC code for calculations of particle transport and interactions with matter. Its applications range from cosmic ray dosimetry to radiotherapy. Results from FLUKA MC simulations are checked against experimental data at single interaction level and the validity of the physical models

implemented in FLUKA has been benchmarked against a variety of experimental data over a wide energy range[46].

FLUKA is a user friendly tool that offers the possibility for scoring a variety of quantities without the user having to write a single line of code[46]. Nevertheless, if the user has a specific problem that reaches beyond the standard settings included in its graphical user interface (FLAIR), one can apply the so-called user routines that are available in the FLUKA software. In these, one can add custom code to obtain the information that one needs from the simulation in order to investigate more specific problems. User routines are, as the rest of the FLUKA MC code, written in the programming language Fortran.

3. Methods

To obtain microdosimetric information when recalculating a proton treatment plan, as outlined in the project objectives, the first step was to generate lookup tables containing lineal energy distributions, $f(y)$ s, for a range of clinical relevant proton energies. Next, the proton energy spectrum, $f(E)$, is scored in scoring volumes, that will be referred to as *voxels*. The $f(E)$ is further used to find the lineal energy distribution in each voxel, $f(y)_{voxel}$, by weighting the $f(y)$ s of the monoenergetic proton beams in the lookup table according to the energy spectrum. Finally, microdosimetric quantities are calculated from $f(y)_{voxel}$ and explored together with the dose and LET_d for different ROIs. This workflow is illustrated in Figure 3.1.

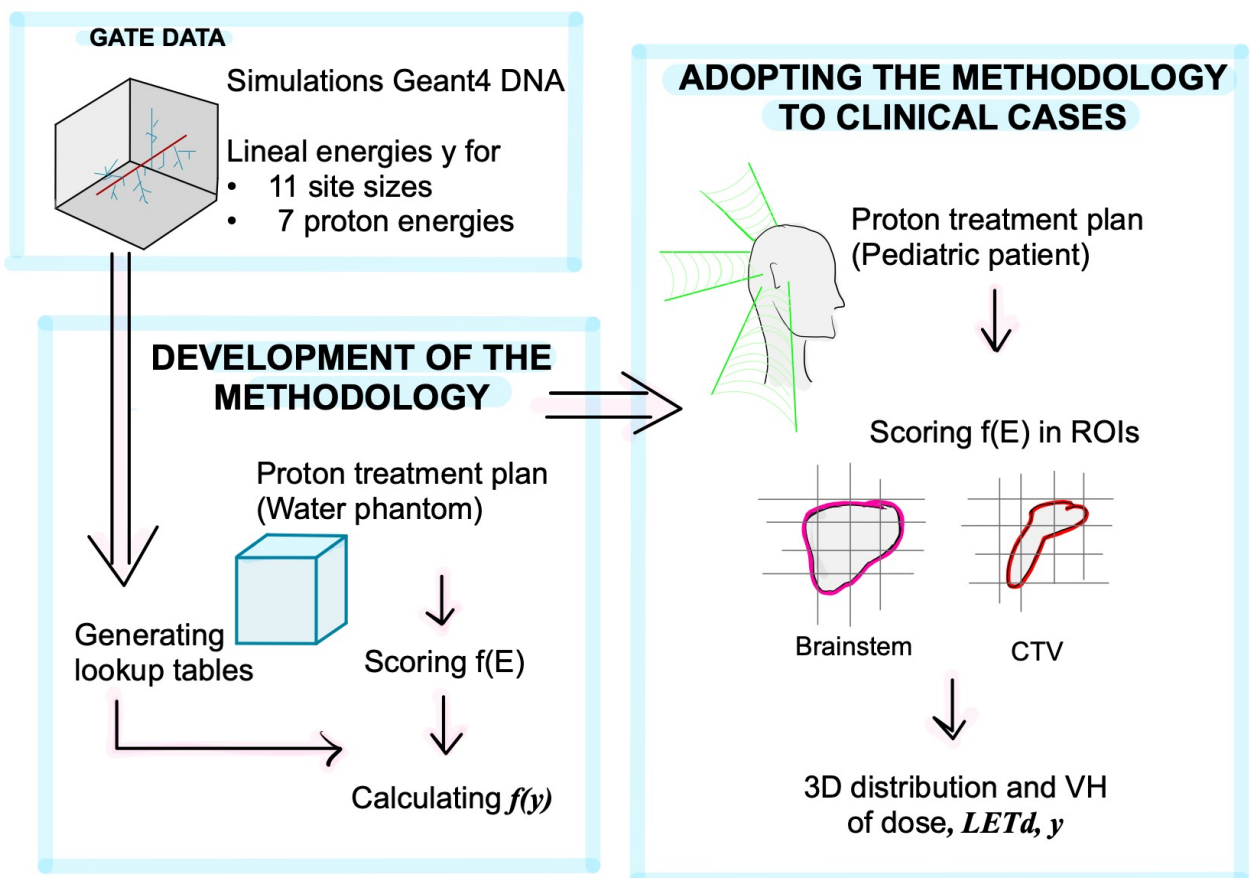


Figure 3.1: Flow chart summarizing the workflow in this project.

Former work at the department was utilized to generate the lookup tables connecting proton energy to lineal energy for a range of different site sizes and proton energies[7]. This work consisted of MC simulations of monoenergetic proton beams, recording the energy depositions along their tracks in spherical sites, for seven different proton energies. From the energy depositions, the lineal energies of these proton tracks were calculated. Recordings were performed in 11 different spheres with diameters ranging from 10 nm to 20 μm . For simplicity, these 11 different sphere diameters will be referred to as sites. The MC simulations were performed in the GATE software with the physics list Geant4 DNA and therefore the data from this work will be referred to as *GATE data*.

During testing and development of this methodology, a simple proton treatment plan for a water phantom was used. Once the method for accessing microdosimetric quantities was verified in the water phantom, the same methodology was applied to a clinical case, a proton treatment plan for a pediatric brain tumor patient. However, several adaptations to the method had to be done when moving from the water phantom to the patient. In particular, the larger amount of data in the clinical case, demanded more practical and efficient data handling.

3.1 Generation of lookup tables from $f(E)$ to $f(y)$

Lookup tables were generated in order to allow for conversion between a proton energy spectrum, $f(E)$, and a lineal energy distribution, $f(y)$.

As outlined in chapter 2.4.1, the lineal energy of a proton track will vary slightly between experiments, as it is a stochastic quantity. It is not like the LET, where there is a corresponding LET value for a given proton energy. However, with good statistics, the variation in $f(y)$ for a given proton track and site size is very little. The $f(y)$ is a probability density function describing which lineal energies a proton track

with this energy is expected to have for this site size. The lookup tables in this project are therefore collections of $f(y)$ for 100 proton energies. As the $f(y)_e$ for a proton energy e varies between site sizes, there is one lookup table for each of the 11 site sizes that were considered in this project. The 11 site sizes included are the same as in the GATE data. No interpolation between the site sizes was performed.

The $f(y)_e$ of a proton track with initial energy e can be obtained through MC simulations. The energy imparted by this track to a site is recorded and divided by the mean chord length of the site, giving the lineal energy y of the track (see chapter 2.4.1. for details). To obtain sufficient statistics, this track is simulated multiple times. Next, the recorded y -values are binned to create the $f(y)$. Recordings like this was performed when the GATE data was created. As it is very time consuming to record the stochastic energy depositions of proton tracks, it was an ambition to utilize the GATE data in this project to generate the lookup tables. As earlier described, only seven monoenergetic proton beams with energies 1, 2, 5, 10, 20, 50 and 100 MeV were simulated in the GATE data. Therefore, interpolation was performed between these proton energies to obtain a lookup table for all proton energies between 1 and 100 MeV.

Interpolation

The interpolation model in this project only considers two $f(y)$ s simultaneously. The interpolated $f(y)$ for a missing proton energy, $e_{missing}$, i.e. one that was not simulated in GATE, is based on the $f(y)$ s of the closest lower and higher proton energy, e_{low} and e_{high} , among the simulated energies. The interpolation model assigns weights, w_{low} and w_{high} , to $f(y)_{low}$ and $f(y)_{high}$ based on their distance in MeV from the missing energy:

$$w_{low} = \frac{|e_{low} - e_{missing}|}{|e_{low} - e_{missing}| + |e_{high} - e_{missing}|} \quad (3.1)$$

$$w_{high} = \frac{|e_{high} - e_{missing}|}{|e_{high} - e_{missing}| + |e_{low} - e_{missing}|} \quad (3.2)$$

In this way the sum of the weights equals one:

$$w_{high} + w_{low} = 1$$

The interpolated $f(y)$, $\widehat{f(y)}$, is a list of n interpolated values from $f(y)_{low}$ and $f(y)_{high}$:

$$\widehat{f(y)} = (\widehat{y}_1, \widehat{y}_2, \dots, \widehat{y}_n)$$

The interpolated values are found by looping through the n lineal energy bins in $f(y)_{low}$ and $f(y)_{high}$ and multiplying each value by their weights. The interpolated value for lineal energy bin i is the sum of the two weighted values:

$$\widehat{y}_i = f(y_i)_{low} * w_{low} + f(y_i)_{high} * w_{high} \quad (3.3)$$

This interpolation is repeated until a $f(y)$ is predicted for each of the missing energies between 1 and 100 MeV. Then the lookup table for that site size is complete. Finally this process is repeated for each of the 11 site sizes. Resultingly, 11 lookup tables are generated.

All calculations described in this chapter is performed with the python script “interpolation_lookuptables.ipynb” included in Appendix C.

Bin width

Between microdosimetric experiments, one preferably adjust the bin width for good resolution in the microdosimetric spectrum. For example, high proton energies have wide spectra and the bin width is then increased compared to the more narrow spectra

of low proton energies. As interpolation is performed between the bins of two $f(y)$ s for different proton energies in this project, the bin width had to be fixed for a site size. A bin width of $0.5 \text{ keV}/\mu\text{m}$ was found to be a bin width that could work fine for all proton energies and site sizes.

The maximum lineal energy for a site size varies greatly between the smallest and largest site size. Therefore the value of the maximum lineal energy bin was varied between the site sizes. The maximum lineal energy observed for a site size in the GATE data is used as maximum lineal energy bin for that site size. In this way the number of bins vary between site sizes. E.g., the $f(y)$ for 10 nm sites have 1336 bins while 20 μm and 1 μm sites has 153 and 122 bins, respectively.

3.2 Treatment planning

Proton treatment plans were made in the treatment planning system (TPS) Eclipse (Varian Medical Systems, Palo Alto, CA, USA).

3.2.1 Water phantom

In the development and testing of this methodology a 20x20x20 cm square cubical water phantom with a 4x4x4 cm square cubical PTV in center was used, see Figure 3.2. In Eclipse, a basic proton treatment plan with one field and prescription dose to the PTV of 2 Gy(RBE) was created. The minimum beam energy delivered was 105 MeV, maximum beam energy was 131 MeV and the number of individual pencil beam spots were 2599.

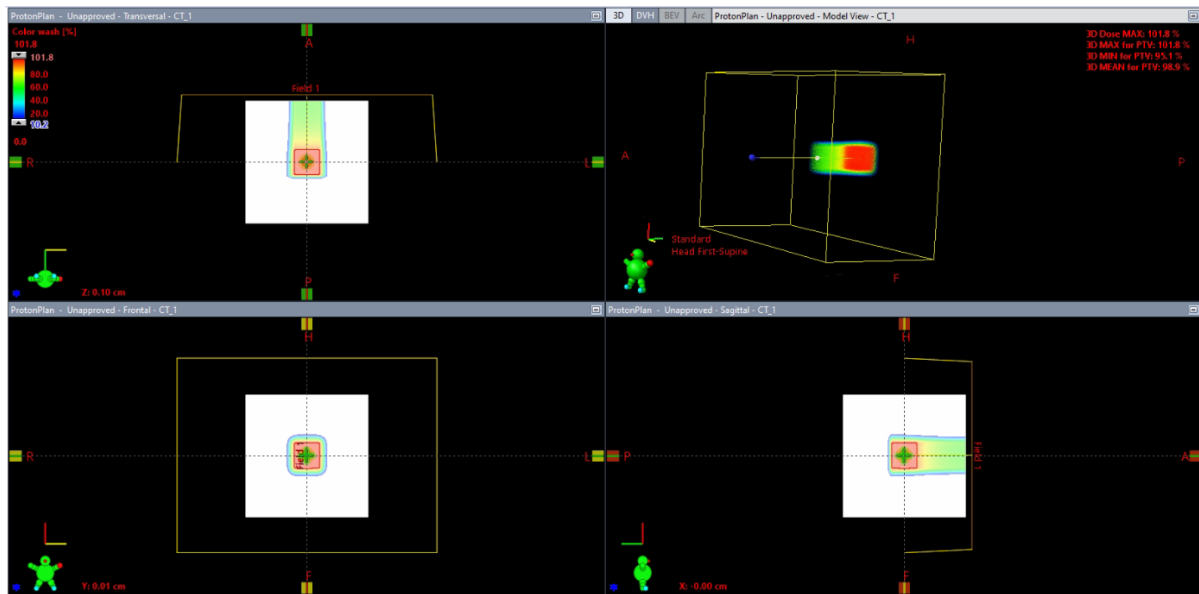


Figure 3.2: Water phantom with PTV in red shown in Eclipse treatment planning system. The dose distribution from Field 1 is visualized with a color wash.

3.2.2 Patient

A proton treatment plan was created for a pediatric patient with a CTV lying anterior of the brainstem. The plan consisted of three fields (90, 180 and 270 °) and the prescription dose was 54 Gy(RBE) to CTV. The plan was optimized, using multifield optimization, with two objectives to the target and two objectives considering OARs. Details about the optimization objectives can be viewed in Table 3.1.

Table 3.1: The objectives used in the optimization of the patient treatment plan.

Structure	Robust	Limit	Vol [%]	Dose [Gy(RBE)]	Priority
<i>Brainstem</i>	No	Upper	0	54.0	200
<i>Brainstem core</i>	No	Upper	0	53.0	200
<i>CTV</i>	No	Upper	0	54.5	100
<i>CTV</i>	Yes	Lower	100	53.5	100

In Figure 3.3 the optimization window in Eclipse is included and the dose volume histograms (DVHs) calculated by the optimization algorithm can be seen. The upper limit objectives are illustrated with downwards arrows and the lower limit with an upwards arrow. The target objective claiming that 100% of the target should receive 53.5 Gy(RBE), was robustly optimized with 12 perturbations involving a 2 mm isocenter shift and a 3% range error. The band around the CTV curve in magenta, represents the dose from the different scenarios included in the robust optimization. Furthermore, the DVH in red illustrates that the dose constraint to the brainstem, claiming that 0 % of the brainstem should receive 54.0 Gy(RBE), is met by the optimization algorithm.

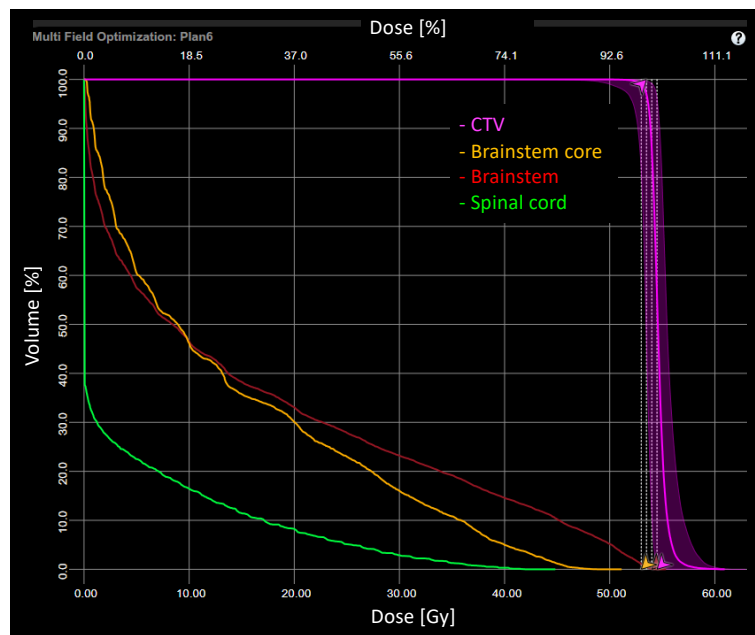


Figure 3.3: Optimization window in Eclipse when optimizing the patient plan. The band around the DVH curve for CTV shows the dose from the different scenarios included in the robust optimization.

The plan was normalized, in such a way that the D50% (median dose) for the CTV was equal to the prescribed dose of 54 Gy(RBE).

3.3 MC simulations with FLUKA

The FLUKA software was used to score energy spectra as well as dose and LET_d in proton treatment plans. Recalculation of treatment plans in FLUKA is a much utilized tool at the department.

The recalculation of dose and LET_d was performed in a separate simulation to the one scoring energy spectra. This was done because two different versions of a user routine was used for each simulation.

3.3.1 Defining the scoring grid

Water phantom

1 million primary protons were simulated and energy spectra $f(E)$ was scored in 100 voxels placed along the beam direction as illustrated in Figure 3.4. As the objective with the water phantom case was to develop and test the methodology, the voxels were relatively large and placed only in the beam direction. In this way it was easy to interpret the scored $f(E)$, as the proton energy will decrease with depth as the proton travels through the water phantom and deposits energy. The voxels were relatively large in order to ensure sufficient statistics. A small voxel size demand more primaries in the simulation compared to a large one for obtaining the same amount of statistics.

The voxels had a size of 0.2 cm along the beam direction and 1 cm in the other two directions. Thus, the spatial resolution of the energy scorings along the beam direction was prioritized as the purpose of these voxels was to observe the energy decrease with depth and especially the sudden decrease in dose and proton fluence after the Bragg Peak. Please note that the height of the voxels (1 cm) are smaller relative to the height of the PTV (20 cm), than it appears in the sketch in Figure 3.4.

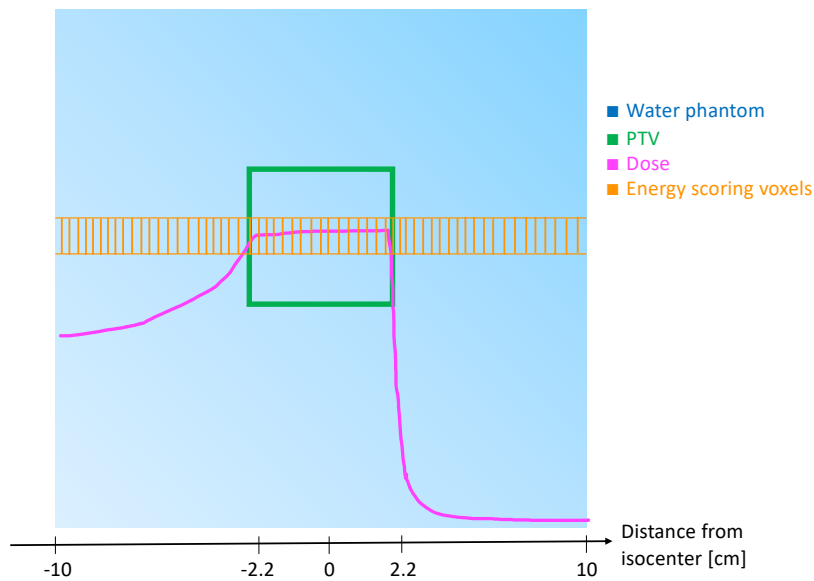


Figure 3.4: Sketch of the water phantom (in blue) with the PTV (in green) showing the location of the 100 scoring voxels (in orange) as well as the position of the SOBP (in magenta). The height of the voxels are smaller relative to the height of PTV in reality. The width of the voxels, which is 2 mm, as well as the number of voxels is not truly represented in the figure.

Patient

For the patient plan, $f(E)$ was scored in two ROIs, the brainstem and the CTV.

480 million primary protons were simulated when scoring $f(E)$ in the brainstem voxels. A smaller amount of primaries is sufficient for recalculating the dose and LET_d as these macroscopic quantities require less statistics than the scoring of $f(E)$. Therefore, the number of primaries was reduced to 48 million to save simulation time. Also, when scoring $f(E)$ in the voxels of the CTV, reducing the number of primaries to 48 million gave sufficient statistics, as this is the target region and there will certainly be more hits per primary compared to the brainstem, located behind the target and outside the primary treatment field.

The size of the simulation data for scoring $f(E)$, the number and dimension of voxels as well as the number of primary protons for the ROIs that were studied in this project are given in Table 3.2. It outlines that the size of the simulation data increased

when moving from the water phantom with 0.1 GB to the clinical case with 24.0 and 59.0 GB in the CTV and brainstem, respectively.

Table 3.2: Overview of the number of voxels, number of primaries simulated and the size of the simulation data for scoring energy spectra in the ROIs.

<i>ROI</i>	Number of voxels	Voxel dimension (x,y,z) [mm]	Number of primaries	Data size [GB]
<i>PTV (water phantom)</i>	100	10.0, 10.0, 2.0	$1 \cdot 10^6$	0.1
<i>Brainstem</i>	13 456	1.3, 1.3, 3.0	$480 \cdot 10^6$	59.0
<i>CTV</i>	39 886	1.3, 1.3, 3.0	$48 \cdot 10^6$	24.0

In treatment planning, DICOM files containing CT images and structure sets are used. The CT images contains information about the attenuation in each voxel in the image, which is used by FLUKA to calculate how the energy is deposited in the patient. When recalculating the plan, we need to locate the voxels that belong to the ROI in which we want to score lineal energy. For this purpose an in-house tool was used to read the DICOM files and locate the relevant voxels for the ROIs. As the voxels need to be defined in a rectangular grid, the script creates the smallest rectangular shape that covers the ROI. The resulting scoring grid for the brainstem consists of 13 456 voxels, while the CTV scoring grid has 39 886 voxels of the same size. The dimension of these voxels reported in Table 3.2, is the same as the voxel dimension used in the TPS.

3.3.2 Energy spectra scoring in FLUKA

To score the voxel-wise proton energy spectra $f(E)$, two detectors that score the same identical fluence of protons, Φ , are applied. Figure 3.5 shows the part of the graphical user interface where the detectors are defined. The detectors are both of type

EVENTBIN, which is a detector type that outputs data for each primary history. Details about the detector can be found in[46].



Scoring fluence of protons in voxels in ROI (brainstem)					
 EVENTBIN			Unit: 22 BIN ▼	Name: fluence	
Type: X-Y-Z ▼	Xmin: -1.6644	Xmax: 2.2438		NX: 29	
Part: PROTON ▼	Ymin: -5.3405	Ymax: -1.4323		NY: 29	
Print: Non-Zero Cells	Zmin: -2.9826	Zmax: 1.8174		NZ: 16	
Scoring fluence of protons x kinetic energy of the protons in voxels in ROI (brainstem)					
 EVENTBIN			Unit: 23 BIN ▼	Name: fluenceE	
Type: X-Y-Z ▼	Xmin: -1.6644	Xmax: 2.2438		NX: 29	
Part: PROTON ▼	Ymin: -5.3405	Ymax: -1.4323		NY: 29	
Print: Non-Zero Cells	Zmin: -2.9826	Zmax: 1.8174		NZ: 16	

Figure 3.5: Graphical user interface for FLUKA where detectors of type EVENTBIN are defined. In the top is the detector scoring fluence and in the bottom the detector scoring fluence multiplied with proton kinetic energy. The area that the scoring grid covers, is defined by the variables $xmin$, $xmax$, $ymin$, $ymax$, $zmin$ and $zmax$ and the number of voxels in the x-, y- and z-direction are decided by the variables NX , NY and NZ . In this example the detectors were set up for scoring the energy in the brainstem of the patient case.

In one of the detectors, Φ is multiplied with the kinetic energy E of the protons. For this purpose, the user routine *fluscw.f* is applied as it enables multiplication by a desired factor of the fluence scorings in a detector. Resultantly, the output from this detector is $\Phi \cdot E$. The version of the *fluscw.f* routine written for this project “fluscw_Hedda.f”, can be found in Appendix A.

With this approach, energy scorings can be obtained by dividing the output from the two detectors on each other as described in chapter 3.4.1. This division is carried out in python after the simulation is finished.

3.3.3 Dose and LET_d scoring in FLUKA

The dose and the LET_d in the treatment plans were recalculated in FLUKA with three detectors of the type USRBIN, shown in Figure 3.6. These detectors score LET multiplied with the fluence of protons, LET squared multiplied with the fluence of protons and dose to water for all particles, respectively. To multiply the fluence scorings, the earlier described *fluscw.f* user routine is again applied here in another

version that has been developed at the department. The background for this method for LET_d scoring is given in the following paragraphs.

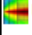
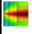
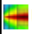
Scores LET x Fluence for protons			
 USRBIN		Unit: 40 BIN ▼	Name: LET
Type: X-Y-Z ▼	Xmin: -9.9995243	Xmax: 10.0004756	NX: 100
Part: PROTON ▼	Ymin: -10.006514	Ymax: 9.99348519	NY: 100
	Zmin: -10.100105	Zmax: 9.899894	NZ: 100
Scores LET*2 x Fluence for protons			
 USRBIN		Unit: 41 BIN ▼	Name: LETsq
Type: X-Y-Z ▼	Xmin: -9.9995243	Xmax: 10.0004756	NX: 100
Part: PROTON ▼	Ymin: -10.006514	Ymax: 9.99348519	NY: 100
	Zmin: -10.100105	Zmax: 9.899894	NZ: 100
Scored dose to water for all particles			
 USRBIN		Unit: 50 BIN ▼	Name: DoseH2O
Type: X-Y-Z ▼	Xmin: -9.9995243	Xmax: 10.0004756	NX: 100
Part: ALL-PART ▼	Ymin: -10.006514	Ymax: 9.99348519	NY: 100
	Zmin: -10.100105	Zmax: 9.899894	NZ: 100

Figure 3.6: Graphical user interface for FLUKA where USRBIN detectors are defined for scoring of dose and LET_D . In this example dose and LET_D are scored in the water phantom.

Absorbed dose can be estimated based on the CSDA by scoring the fluence of particles (Φ)[13]:

$$D(E, i) = \frac{S_{el}(E)\Phi(E, i)}{\rho(i)} \quad (3.4)$$

where E is the energy of the particle at location i , S_{el} is the electronic stopping power for this energy and ρ is the mass density of the material. $S_{el}(E)$, which is essentially the LET, is obtained from the built-in function in FLUKA named GETLET.

Equation (2.4) from chapter 2.1.1 can be rewritten so that the LET_d at location i is:

$$LET_d(i) = \frac{\int_0^\infty S_{el}(E)D(E, i)dE}{\int_0^\infty D(E, i)dE} \quad (3.5)$$

where S_{el} is the electronic stopping power for energy E and $D(E, i)$ is the absorbed dose.

Inserting (3.4) into (3.5), the LET_d is given as:

$$LET_d(i) = \frac{\int_0^{\infty} S_{el}^2(E)\Phi(E, i)dE}{\int_0^{\infty} S_{el}(E)\Phi(E, i)dE} \quad (3.6)$$

The preprocessing of the data scored by the USRBIN detectors were handled by an in-house python script[48]. After recalculation of the dose in FLUKA, the dose was again normalized so that the median CTV dose equals the prescribed dose.

3.4 Processing of simulation data in python

3.4.1 Calculating the energy spectra $f(E)$

During the FLUKA simulation, two fluence detectors write their scorings to binary files, as described in chapter 3.3.2.

In python, the scorings from the first detector, $\Phi \cdot E$, is divided by the scorings from the second detector, Φ :

$$E = \frac{\Phi \cdot E}{\Phi} \quad (3.7)$$

The result is a matrix containing all energy scorings by each primary in each voxel in the ROI. However, after the division is performed, the information about which primary had which energy scoring, is not of interest anymore. This label was only kept in order to divide the corresponding scoring values from the detectors.

Therefore, the data size can now be reduced by binning the energy data into energy spectra $f(E)$. The energy scorings are binned in 99 bins of size 1 MeV. In each bin the protons with that energy and up to the energy of the next bin, are stored. E.g. bin “3 MeV” contains protons with energies from 3 MeV and up to 4 MeV. However, protons with energy below 1 MeV are put in the lowest energy bin “1 MeV” and protons with energy higher than 100 MeV are put in the last bin “99 MeV”. Figure

3.7 illustrates how the $f(E)$ in all voxels are stored in a data frame with the energy bins as index.

Energy bin [MeV]	0	1	2	3	4	5	6	7	8	9	...	13446	13447	13448	13449	13450	13451	13452	13453	13454	13455
1	21	24	21	26	24	23	18	22	20	30	...	3839	3823	3644	3804	3915	3943	3935	3524	3029	2833
2	0	2	2	0	2	1	1	2	2	4	...	3826	3767	3600	3737	3745	3812	3746	3434	2941	2704
3	1	1	3	0	0	1	2	1	4	0	...	4872	4938	4826	4852	4907	4940	4707	4104	3705	3383
4	2	2	1	1	3	0	1	1	2	1	...	5922	6057	5932	5925	5969	5773	5309	4675	4218	4002
5	2	1	1	1	2	1	3	1	1	0	...	6448	6760	6863	6811	6759	6542	5964	5060	4453	4422
...
95	0	0	0	0	0	0	0	0	0	0	...	0	0	0	0	0	0	0	0	0	0
96	0	0	0	0	0	0	0	0	0	0	...	0	0	0	0	0	0	0	0	0	0
97	0	0	0	0	0	0	0	0	0	0	...	0	0	0	0	0	0	0	0	0	0
98	0	0	0	0	0	0	0	0	0	0	...	0	0	0	0	0	0	0	0	0	0
99	0	0	0	0	0	0	0	0	0	0	...	0	0	0	0	0	0	0	0	0	0

99 rows x 13456 columns

Figure 3.7: Data frame containing the energy spectra in each voxel in the brainstem of the patient case. The shape of the data frame is 99 times 13 456, as this is the number of energy bins and voxels for the brainstem, respectively.

For details about the data handling in python described in this chapter, see the script “energyspectra_binary_sparse.py” in Appendix C.

3.4.2 Microdosimetric calculations

The ambition is to find in any voxel in the treatment field a lineal energy distribution, $f(y)_{voxel}$, that can be used to calculate microdosimetric quantities as the \bar{y}_D in the voxel.

The $f(E)$ scored in a voxel will be used for this purpose by looping through the energy bins and for each proton energy, e , finding the corresponding lineal energy distribution, $f(y)_e$, for such a monoenergetic proton beam in the lookup table. The $f(y)_e$ is weighted according to the number of protons with that energy e in the voxel relative to the total number of protons in the voxel. In other words, it is weighted by the $f(E)$ in the voxel. The final $f(y)_{voxel}$ is the sum of all the weighted $f(y)_e$:

$$f(y)_{voxel} = \frac{\sum_e f(y)_e \cdot f(E)_e}{\sum_e f(E)_e} \quad (3.8)$$

From $f(y)_{voxel}$ the microdosimetric quantities $d(y)$, \bar{y}_F and \bar{y}_D can be calculated for the voxel by using the equations given in chapter 2.3.2.

A simple and theoretical example will be given here to illustrate the method. In Table 3.3 the energy spectrum in “Voxel 1” is given. For simplicity this voxel only has three different energy bins and there are in total 1000 protons that have been registered in the voxel. The second column of the table contains the weights.

Table 3.3: Illustrative example of an energy spectrum and the weights for each energy in a fictive voxel.

Energy [MeV]	Voxel 1 proton counts	Voxel 1 weights
1	450	450/1000 = 0.45
2	350	350/1000 = 0.35
3	200	200/1000 = 0.20

With the data given in the table, the $f(y)$ in voxel 1 can be calculated like this:

$$f(y)_{voxel\ 1} = f(y)_{1\ MeV} * 0.45 + f(y)_{2\ MeV} * 0.35 + f(y)_{3\ MeV} * 0.20$$

Where $f(y)_{1\ MeV}$, $f(y)_{2\ MeV}$ and $f(y)_{3\ MeV}$ are the $f(y)$ functions for energies 1, 2 and 3 MeV found in the lookup table.

All calculations described in this chapter are performed in python with the script “find_microdosimetry_voxel.py” which is included in Appendix C.

4. Results

First, I will evaluate the lookup tables that were generated from the *GATE* data. Secondly, the results found when testing and developing the method with the use of the water phantom will be presented. Here I want to investigate if the energy spectra that we found in the water phantom shows realistic values. It is also relevant to assess whether the microdosimetric values calculated from the energy spectra seem reasonable. Finally, the results from the patient case will be presented. This includes displaying the \bar{y}_D -values that were calculated in the brainstem and CTV and compare these values with the dose and the LET_D . How the lineal energy varies between different site sizes will also be presented.

4.1 Lookup tables

Interpolation was performed between the data points in the *GATE* data in order to generate lookup tables for all discrete proton energies from 1 to 100 MeV. These are included in Appendix C.

4.1.1 Interpolated $yd(y)$ distributions

In Figure 4.1 - 4.3 examples of the interpolated microdosimetric spectra, $yd(y)$, are shown. The interpolated spectra are plotted between the original *GATE* data 2 and 5 MeV (Figure 4.1), 10 and 20 MeV (Figure 4.2) and between 20 and 50 MeV (Figure 4.3). The distributions are plotted for site sizes 10 nm, 100 nm, $1\mu\text{m}$ and $10\mu\text{m}$.

Please note that the scale of the x-axis has been changed between the plots to improve visibility.

The first thing to notice from the figures is that the vertical lines of each spectrum, the y_D -values, are (as expected) ordered in the way that the y_D -values decrease when site sizes increases. Secondly, the interpolated spectra are always located between the

two spectra from the GATE data that they were interpolated from. Especially the rising edges seem evenly separated between the two. Thirdly, in all plots one can see a difference between the two interpolated spectra. The spectra of 3 and 4 MeV, which are both interpolations from the spectra of 2 and 5 MeV, are in fact different. This indicates that the weighting in the interpolation has worked. However, there are some clear limitations in the interpolated spectra.

The interpolated spectra seem to adopt the shape of the lowest energy rather than the highest energy among the two energies that it is interpolated from. This is seen both in the falling edge of the interpolated spectra and the peak position. In Figure 4.1 it is visible that the falling edge of the interpolated spectra, 3 and 4 MeV, are both closer to the 2 MeV spectra than the 5 MeV spectra for the site sizes above 10 nm. It was expected that the true falling edges of the intermediate energies would lie closer to the middle between the two spectra. The same problem with the falling edges, although to a lesser extent, is seen for the high energies in Figure 4.2 for site sizes 1 and 10 μm . E.g. the falling edges of 13 and 17 MeV lie unexpectedly close to that of the 10 MeV spectra. For the smallest site size, 10 nm, the falling edges are quite similar for all energies and the error is therefore less prominent. Regarding the peaks of the interpolated spectra, they are often almost identical to the peak of the lowest energy spectra. And as the distance between the peaks of two GATE energies increase with site size, this error is more outstanding for the largest site sizes. Both these symptoms, the falling edges and the peak position of the interpolated spectra, indicate that the interpolation model might give a slight overestimation of the lineal energy.

The $yd(y)$ distributions for energies between 20 and 50 MeV in Figure 4.3 are generally wider than for the lower energies. This is due to a greater variance in how much energy each event deposits for higher energy protons [7]. With wider spectra, the falling edges become more similar, and that is why the falling edge error is less

problematic for the high proton energies compared to the low proton energies. $yd(y)$ distributions for energies between 50 and 100 MeV are included in Appendix B.

The double peak in 4 MeV spectrum for site size $10\ \mu\text{m}$ in Figure 4.1 needs to be discussed. It appears that when the distance between the peaks of the two spectra from GATE data becomes large, as happens for large site sizes and low energies, the interpolation model creates a spectrum that is much wider than the original spectra. And this wide spectrum will have two separate peaks if the distance is very large. The same effect is seen in Figure 4.2 in the 17 MeV spectrum with two soft peaks at site size $10\ \mu\text{m}$. This is yet another weakness of the interpolation model as microdosimetric spectra with several distinct peaks deviate from reality.

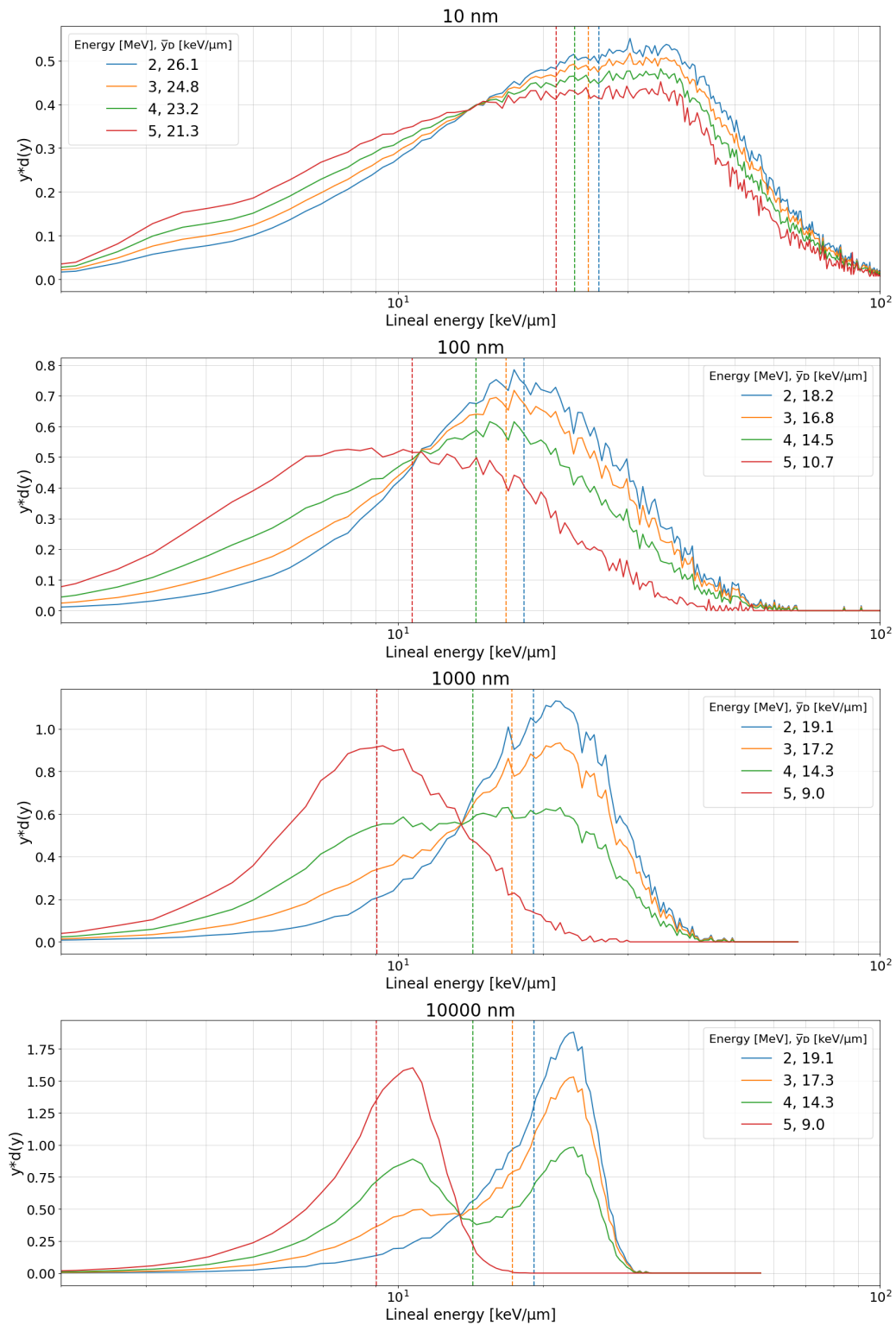


Figure 4.1: $y^*d(y)$ distributions proton energies 2 - 5 MeV and site sizes 10nm - 10 μ m. The spectra for 2 and 5 MeV are from the GATE data and the two other spectra are interpolated from these. The \bar{y}_D value of each spectrum is plotted as a vertical line.

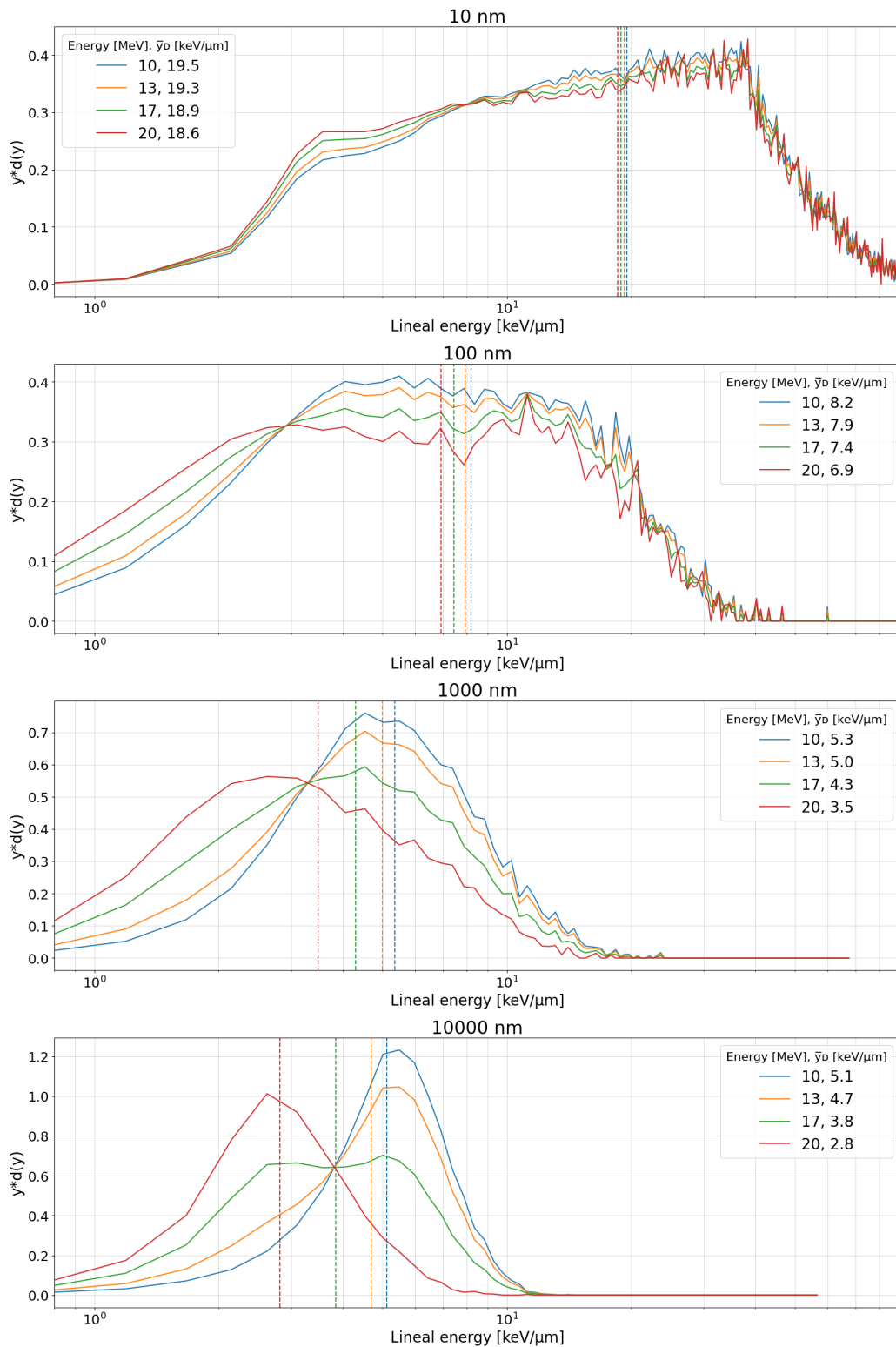


Figure 4.2: $y^*d(y)$ distributions for proton energies 10 - 20 MeV and site sizes 10nm - 10 μ m. The spectra for 10 and 20 MeV are from the GATE data and the two other spectra are interpolated from these. The \bar{y}_D value of each spectrum is plotted as a vertical line.

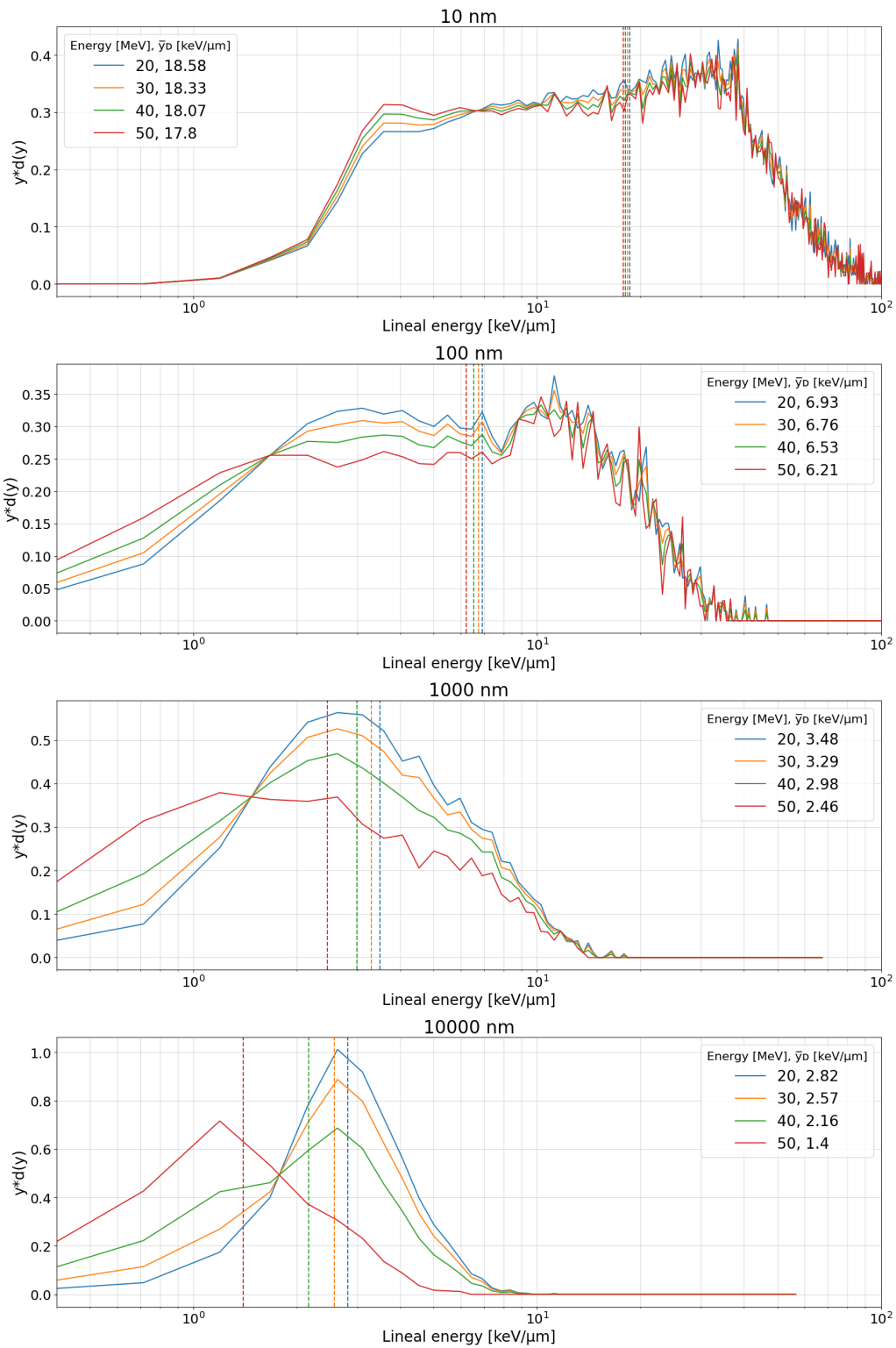


Figure 4.3: $y^*d(y)$ distributions for proton energies 20 - 50 MeV and site sizes 10nm - 10 μm . The spectra for 20 and 50 MeV are from the GATE data and the two other spectra are interpolated from these. The \bar{y}_D value of each spectrum is plotted as a vertical line.

4.1.2 Interpolated \bar{y}_D - and \bar{y}_F - values

For each microdosimetric spectrum, the dose-mean lineal energy \bar{y}_D and frequency-mean lineal energy \bar{y}_F is calculated. This gives 1100 \bar{y}_D - and \bar{y}_F -values, as there is one spectrum for each discrete proton energy from 1 MeV to 100 MeV and for each of the 11 studied site sizes.

\bar{y}_D -values

The \bar{y}_D -values are plotted against proton energy in Figure 4.4 and the data points from the GATE data are plotted as dots in the curves. Please note that as proton tracks of both 1 and 2 MeV were simulated in GATE data, there is no interpolation between these energies.

A tendency of the curves to bend upwards between the dots is observed. This is explained by the interpolated spectra presented in chapter 4.1.1, revealing that the interpolation model tends to weigh the spectra with the highest lineal energies the most. Resultingly, the \bar{y}_D -values between the dots are overestimated and the curve bends upward. The bending effect appears to be largest for the 20 μm site size and to be more prominent for the lower proton energies. The bending effect decreases with increasing energy and decreasing site size and it is probably negligible for energies above 20 MeV and site sizes below 0.1 μm (100 nm).

As expected, the LET is lower than the \bar{y}_D -value for all site sizes and all proton energies. However, for the largest site sizes the \bar{y}_D becomes increasingly similar to the LET with proton energy.

Finally, a comment on the \bar{y}_D -values seen for 1 MeV protons must be given. The values deviate from the overall trend of increasing \bar{y}_D with decreasing site size. This is explained by the fact that for low energies, the range of the protons are short. A proton with energy 1 MeV has a range in liquid water of approximately 24.6 μm [49].

Thus, the proton deposits a considerable amount of its initial energy inside the larger sites and as the energy deposit from a proton is higher the longer it travels due to the increase in stopping power with decreasing energy, the \bar{y}_D becomes high for the large site sizes at 1 MeV.

In Figure 4.5 the interpolated \bar{y}_D -values for proton energies 3, 4, 8, 17, 35 and 65 MeV are plotted as a curve against site size. Each proton energy in the GATE data is plotted as dashed curves. Firstly, one can notice that the interpolated curves lie between the curves of the GATE data. Even though not all the interpolated curves are plotted here, this implies that the interpolation is working. Secondly, the curves of 3 and 4 MeV lie closer to the curve of 2 MeV than 5 MeV, especially for site sizes larger than $0.1 \mu\text{m}$ (100 nm). The true curve of 4 MeV is expected to lie closer to 5 MeV than it does in this figure. This is the same interpolation error that was observed in the $yd(y)$ of 3 and 4 MeV, possibly leading to an overestimation in the \bar{y}_D .

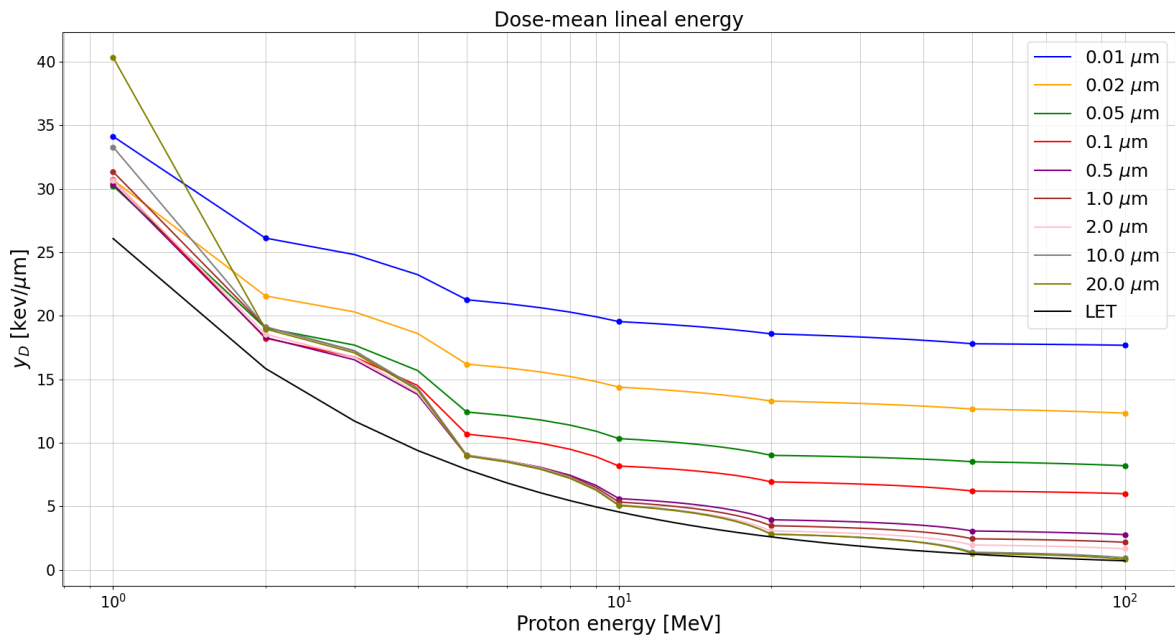


Figure 4.4 The dose-mean lineal energies (\bar{y}_D) for proton energies 1 -100 MeV for site sizes 10 nm - 20 μm . The dots in the curves are the data points from the GATE data and the curves between them is the interpolated data. The LET for the proton energies is plotted as a black curve with data from PSTAR [49].

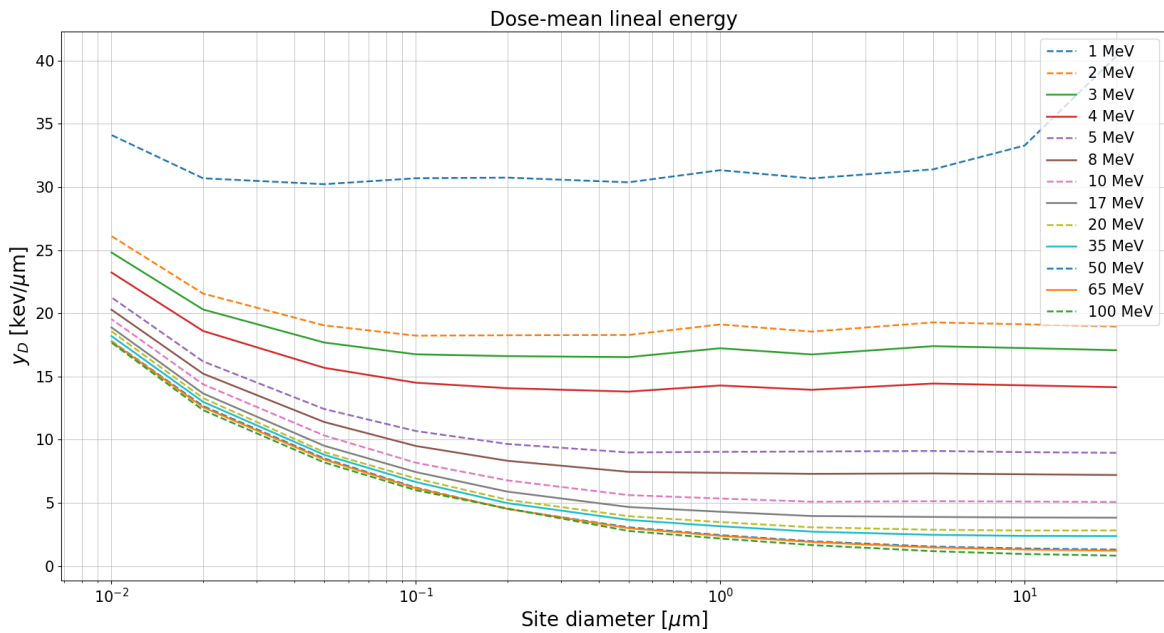


Figure 4.5: Dose-mean lineal energies (\bar{y}_D) for site sizes 10 nm - 20 μm for proton energies 1 MeV - 100 MeV. The dashed lines are plots from the GATE data and the other lines are interpolated data.

\bar{y}_F -values

The same plots were made for the frequency mean lineal energies and can be seen in Figure 4.6 and 4.7.

In figure 4.6 the curves are more overlapping than in the corresponding plot of \bar{y}_D (Figure 4.4). Some upwards bending of the \bar{y}_F -curves is observed and it is most prominent for proton energies between 2 and 10 MeV and for the largest site size (20 μm). This indicates that the interpolation model slightly overestimates the \bar{y}_F -values of low proton energies and large site sizes. Furthermore, the calculated \bar{y}_F -values are lower than the \bar{y}_D -values for all proton energies and site sizes. This is as expected from theory described in chapter 2.3.2.

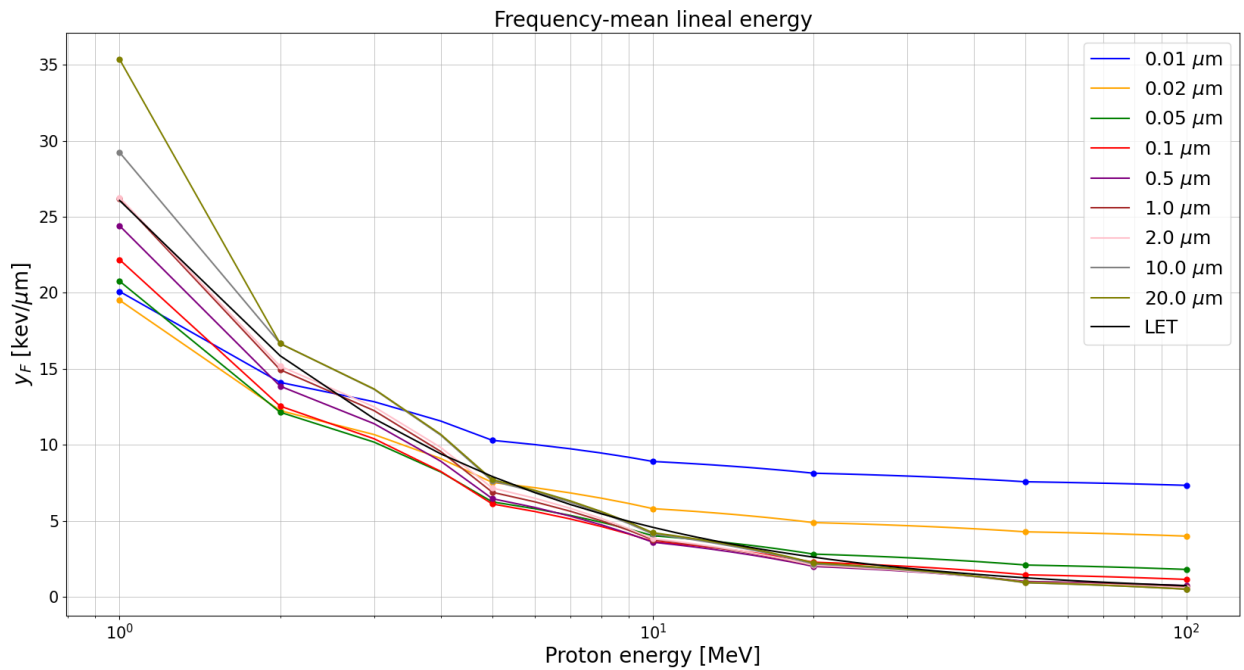


Figure 4.6: Frequency-mean lineal energy (\bar{y}_F) for proton energies 1 - 100 MeV for site sizes 10 nm - 20 μm . The dots in the curves are the data points from the GATE data and the curves between them are the interpolated data. The LET for the proton energies is plotted as a black curve with data from PSTAR [49].

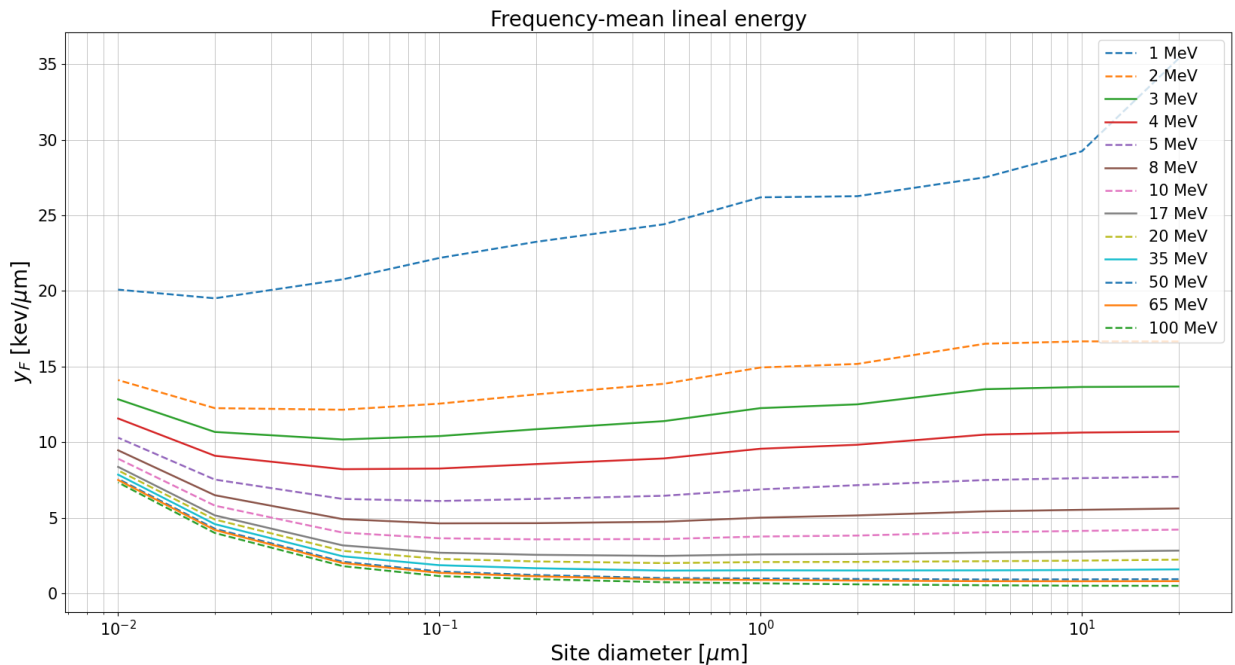


Figure 4.7: Frequency-mean lineal energy (\bar{y}_F) for site sizes 10 nm - 20 μm plotted for proton energies 1 - 100 MeV. The dashed lines are plots from the GATE data, whereas the solid lines are interpolated data.

4.2 Water phantom

4.2.1 Energy spectra in water phantom

Energy spectra scoring in the water phantom gave a proton energy spectrum ($f(E)$) in each voxel. For the sake of visibility only a few of the $f(E)$ s scored in the water phantom are presented Figure 4.8. The plotted $f(E)$ s are all from voxels within the target region of the treatment plan, the PTV.

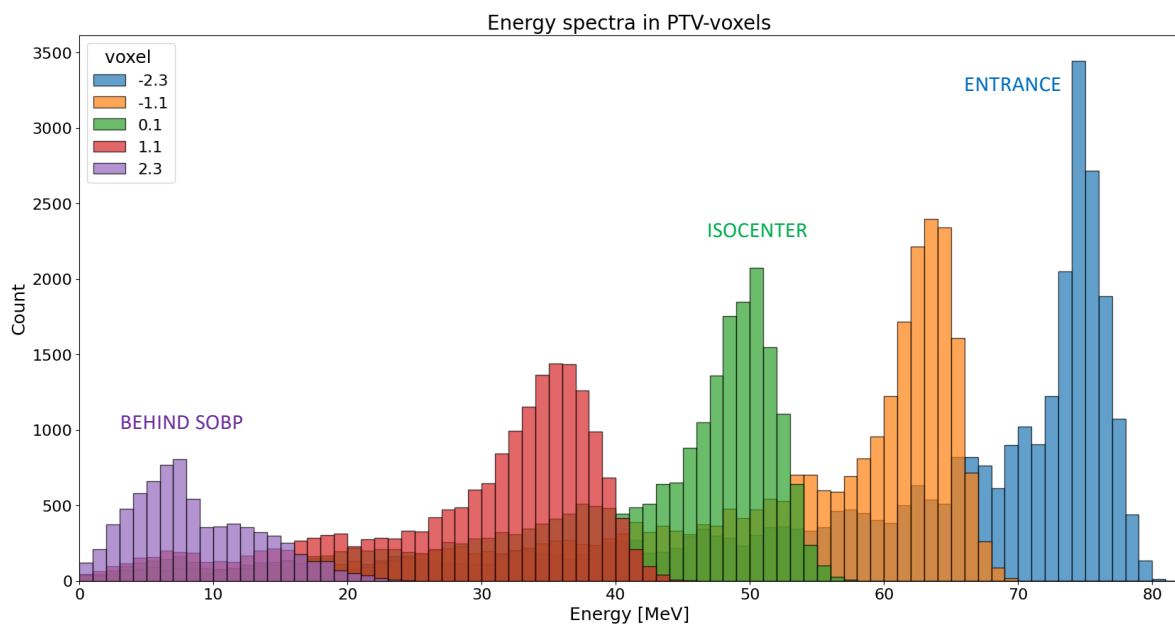


Figure 4.8: Proton energy spectra, $f(E)$, scored in some of the voxels in the PTV of the water phantom when recalculating the treatment plan in FLUKA. The voxel positions are given in cm from isocenter, where isocenter is in the center of the PTV. The voxels at -2.3 cm (blue), 0.1 cm (green) and 2.3 cm (purple) gives an example on the $f(E)$ in the entrance region of the SOBP, the isocenter and behind the SOBP, respectively.

The $f(E)$ in Figure 4.8 shows that the energy and the number of protons decreases with depth, as expected. Indicating that our method for energy scoring is working.

Even though all voxels had at least one registered hit, only 5.8 % of the one million primaries that were simulated in the water phantom, had a registered energy scoring in one of the voxels. As the treatment field is designed to cover the whole PTV, its

lateral size is larger than the lateral size of the voxels as illustrated by Figure 3.4. Thus, many of the primaries are not registered in the voxels. This emphasizes the need for high statistics when scoring $f(E)$ with our method.

In Figure 4.9 the proton energy scored for 500 randomly chosen protons is plotted against depth, visualizing the range of the protons in the treatment field. Scorings are plotted as dots and a line is drawn between each dot. The CSDA range is plotted for 105 and 131 MeV, the minimum and maximum beam energy in the treatment plan, showing a match with the location of the SOBP between -2.2 and 2.2 cm. The figure illustrates that the majority of the primaries behave according to Bethe Bloch theory, having a continuous energy loss before a more rapid decrease in energy in depth and finally stopping somewhere in the SOBP. Furthermore, the figure illustrates the stochastic pattern of energy deposition in the proton beams as some of the curves deviate from trend of the majority by having a large decrease in energy already in the entrance of the water phantom. Additionally, the figure illustrates that secondary protons are also scored with our method as one can see a few short curves that does not start at -10 cm. The red curve with three scorings at -4 cm is an example.

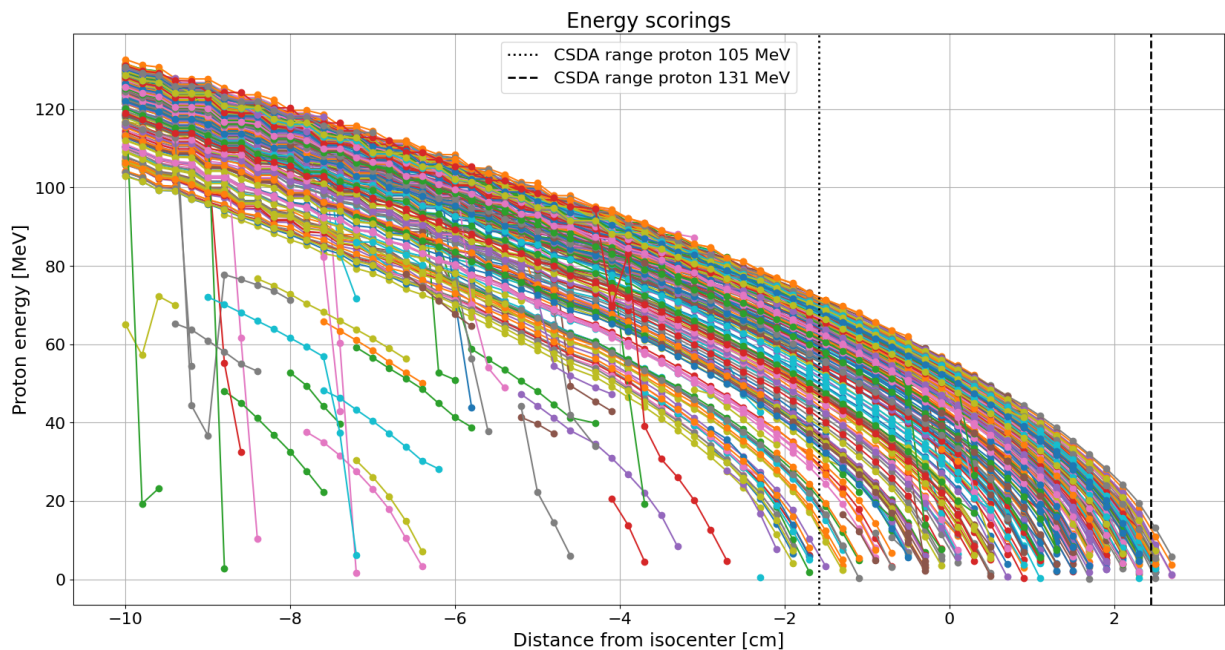


Figure 4.9: The energy scorings of 500 randomly chosen protons in the beam irradiating the water phantom. The CSDA range of the minimum (105 MeV) and maximum (131 MeV) beam energy in the treatment field is plotted with data from PSTAR[49]. The SOBP of the treatment plan is located between -2.2 and 2.2 cm from isocenter.

The mean energy among all energy scorings in the voxels is also decreasing with depth, as illustrated with the blue curve in Figure 4.10. In the depth beyond the SOBP, which ends at 2.2 cm from isocenter, there are some peaks in the curve showing proton energy scorings up to 20 MeV. As can be seen from the orange dotted curve in the plot, which is the number of protons present in the voxels, there is approximately zero protons in these voxels, meaning that the majority of the protons stop in the SOBP and that these relatively high energy scorings beyond the SOBP originate from a few single protons. As the high-energetic proton beams in the treatment field traverses water, neutrons are produced through nuclear interactions[50-52]. These neutrons can travel beyond the Bragg peak and might produce secondary protons through collisions with hydrogen atoms in the water molecules. It is assumable that the energy scorings in the depth in Figure 4.10 originate from such secondary protons.

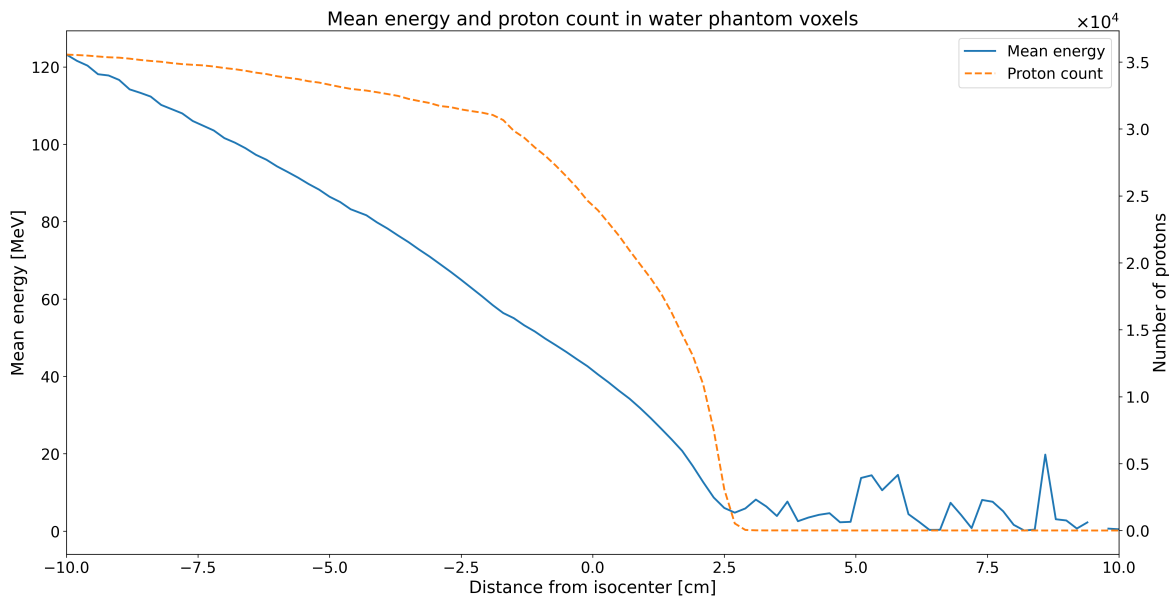


Figure 4.10: The mean energy in each of the 100 voxels in the water phantom is plotted in blue together with the number of protons in each voxel in orange. The x-axis is the location of the voxels in distance from isocenter.

4.2.2 Microdosimetric calculations in water phantom

The $f(E)$ scored in the water phantom voxels are used to calculate the microdosimetric spectra and their averages, \bar{y}_F and \bar{y}_D . In Figure 4.11 $yd(y)$ for three different voxels are plotted for site sizes between 10 nm and 20 μm . \bar{y}_D -values for the spectra are shown as vertical lines. The voxels are located at -2.3 cm, 0.1 cm and 2.3 cm from isocenter, thus the microdosimetric spectra found in these voxels represent the microdosimetric spectra found at the entrance, at isocenter and behind the SOBP. The $f(E)$ in these voxels were presented in Figure 4.8.

For the voxel located in the entrance, the \bar{y}_D is increasing with decreasing site size. For the two other voxels this is not the case and especially not for the voxel behind the SOBP where the \bar{y}_D of the largest site size, 20 μm , becomes higher than many of the smaller site sizes. This is explained by the \bar{y}_D -curves in Figure 4.4 where it can be seen that for 1 MeV protons, the \bar{y}_D of site size 20 μm is the largest among all site

sizes. The $f(E)$ for the deepest voxel, given in Figure 4.8, shows that most protons in this voxel have an energy below 10 MeV. Additionally, as shown in chapter 4.1.1, \bar{y}_D is slightly overestimated by the interpolation model for proton energies 2-10 MeV. Therefore, although it is expected that the \bar{y}_D becomes high for site size 20 μm in a voxel where proton energies are very low, the values seen here are probably slightly higher than the true values.

In the voxel behind the SOBP, the 20 μm $yd(y)$ -distribution stands out from the other site sizes, as it has some very distinct peaks rather than a smooth spectrum. These peaks can, to a lesser extent, be observed in the two other voxels as well for this site size. An experimental microdosimetric spectrum would not have this multi-peak appearance, but rather a broad and smooth distribution.

In Figure 4.11 the $yd(y)$ -distributions for the same voxels are plotted, but the spectra for the largest site sizes are removed, enabling inspection of the smaller site sizes. The figure shows that as the energy decreases from the voxel at entrance to the voxel behind the SOBP, the peaks of the $yd(y)$ -distributions move towards higher lineal energies. Also, the figure displays higher lineal energies and \bar{y}_D -values for the smallest site sizes.

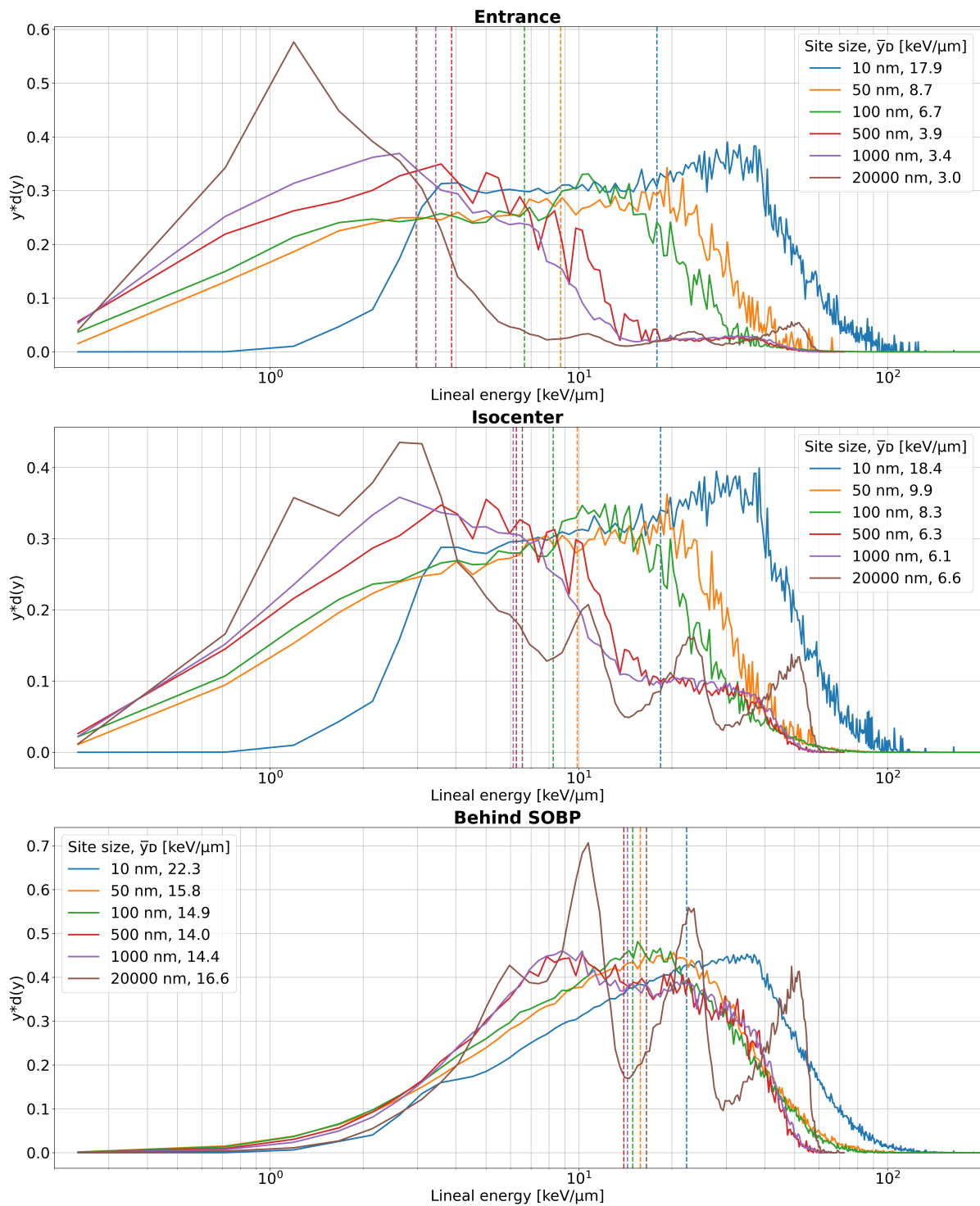


Figure 4.11: $y_d(y)$ -distributions for voxels at entrance, isocenter and behind the SOBP in the water phantom for site sizes 10 nm – 20 μm .

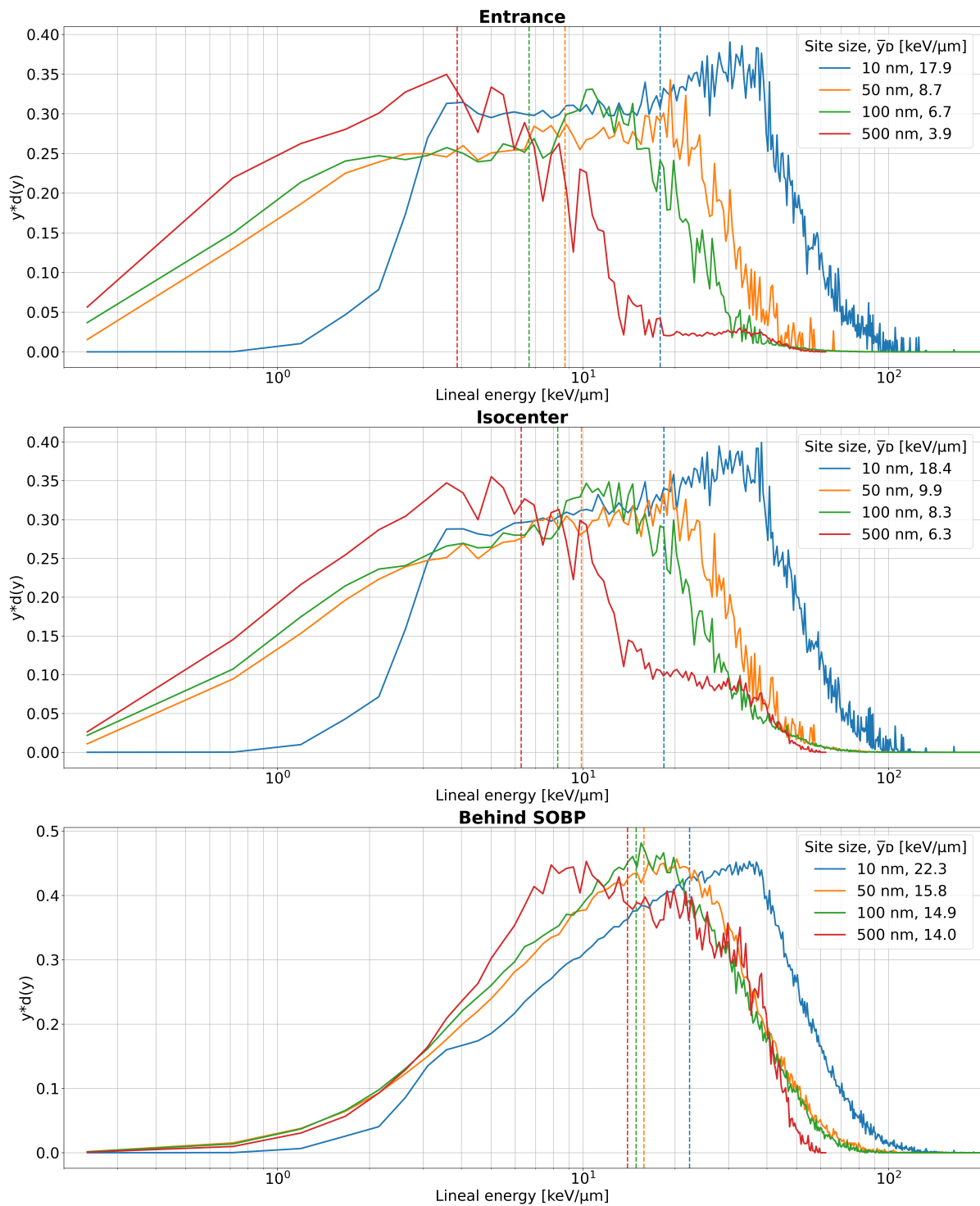


Figure 4.12: $y d(y)$ -distributions for voxels at entrance, isocenter and behind the SOBP in the water phantom for site sizes 10, 50, 100 and 500 nm.

In Figure 4.13 the \bar{y}_D -values are plotted along the beam direction (distance from isocenter) for six different site sizes. The dose-depth curve and the LET_d -curve is also shown in the figure. The dose curve shows how the SOBP delivers a more or less homogeneous dose distribution of 2 Gy(RBE) in the PTV and the LET_d -curve present rising LET_d values towards the end of the SOBP. The \bar{y}_D is for all site sizes calculated to be higher than the LET_d for all depths in the water phantom. Furthermore, the figure illustrates a large spread in the calculated \bar{y}_D among site sizes. This spread is reduced towards the end of the SOBP and smallest in the DDF. This is explained by earlier presented results showing that \bar{y}_D rises for the larger site sizes when proton energy is low, as in the DDF.

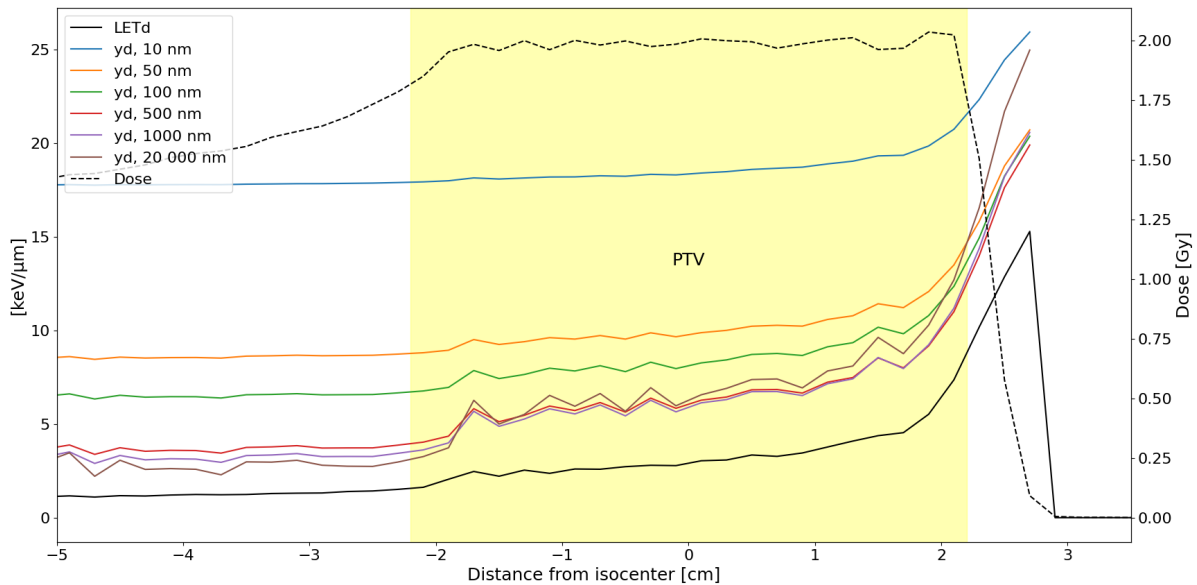


Figure 4.13: Shows the development of dose, LET_d and \bar{y}_D along the beam direction (distance from isocenter). The \bar{y}_D is plotted for six different site sizes.

The frequency-mean lineal energy, \bar{y}_F , is calculated for each voxel and plotted against depth together with the LET_d and the dose in Figure 4.14. The LET_d is greater than the \bar{y}_F for all sites except the 10 nm site. In the DDF the LET_d is greater than all site sizes, followed by the 20 μm and 10 nm sites.

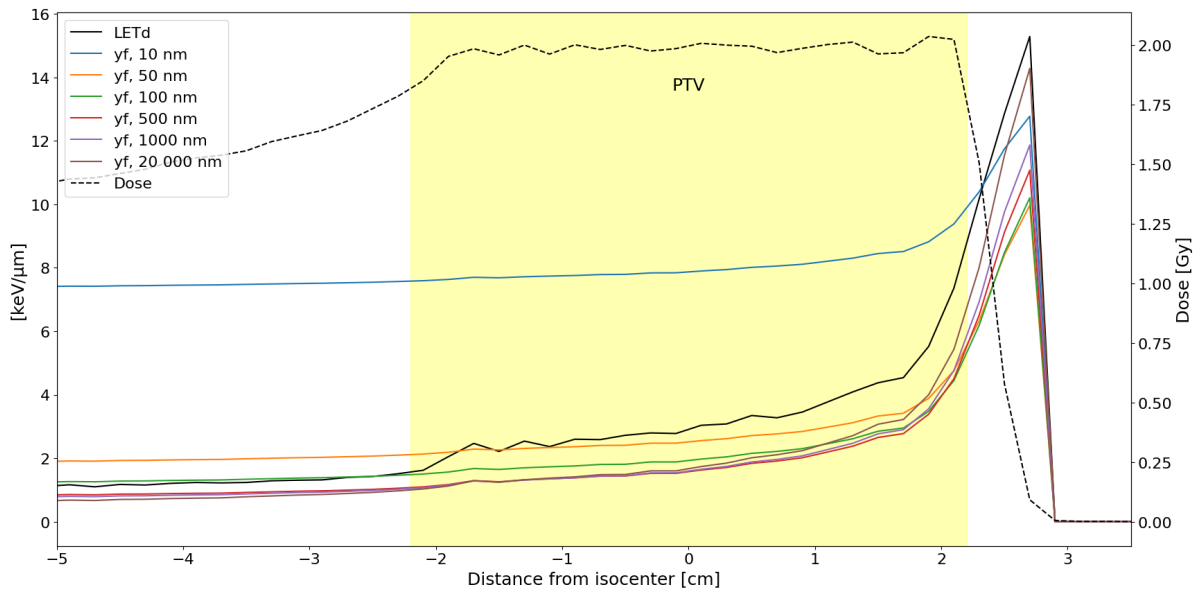


Figure 4.14: Shows the development of dose, LET_d and \bar{y}_F along the beam direction (distance from isocenter). The \bar{y}_F is plotted for six different site sizes.

4.3 Patient case

4.3.1 Plan evaluation

Recalculation of the treatment plan in FLUKA gave the dose and LET_d distributions given in Figure 4.15 when considering all three treatment fields in the plan. The plan delivers a homogenous dose of approximately 54 Gy(RBE) to the target (CTV) while spilling some dose outside in the surroundings of the target. This is as expected from the robust optimization which gives a treatment plan that ensures target dose coverage even with a 2 mm isocenter shift. For the same reason and because of its proximate location to the target, some areas of high dose are seen in the brainstem. The LET_d -distribution shows low LET_d values in the target region and increased values in some areas outside the target region. It appears to be three hot-spot regions of LET_d , probably one from each field due to protons with Bragg peak just outside the target.

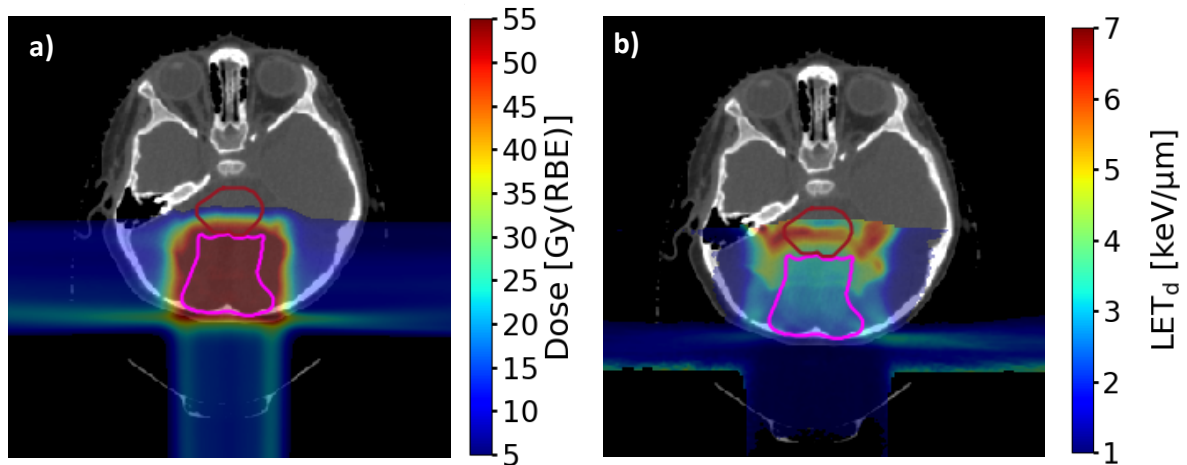


Figure 4.15: FLUKA recalculation of all fields in the treatment plan . The brainstem is contoured in red and the CTV (target) in magenta. a) Biological dose (RBE 1.1) and b) LET_d .

For all LET_d - and \bar{y}_D -values presented in this chapter, a dose cutoff at 0.5 Gy(RBE) has been applied, meaning that the LET_d and \bar{y}_D is only considered for voxels where the dose is greater than 0.5 Gy(RBE).

The DVH for the brainstem and the CTV is shown in Figure 4.16 to the left and it illustrates sufficient dose coverage to the CTV and an acceptable low dose to brainstem. The $D_{98\%}$ for the CTV equals 52.71 Gy(RBE) and the demand of $D_{98\%} \geq 95\%$ of prescribed dose (95% of 54 Gy(RBE) is 51.30 Gy(RBE)) is therefore met. For the brainstem dose evaluation criteria were $D_{0.03cc} \leq 60$ Gy(RBE) for the surface and $D_{0.03cc} \leq 54$ Gy(RBE) for the interior. As a $D_{0.03cc}$ of 53.43 Gy(RBE) is calculated for the brainstem, the constraints are held.

The LET volume histogram (VH) in Figure 4.16 to the right demonstrates that the LET is higher in the brainstem than in the CTV, which is explained by the fact that the LET rises toward the end of a proton beam and the brainstem is located behind the target.

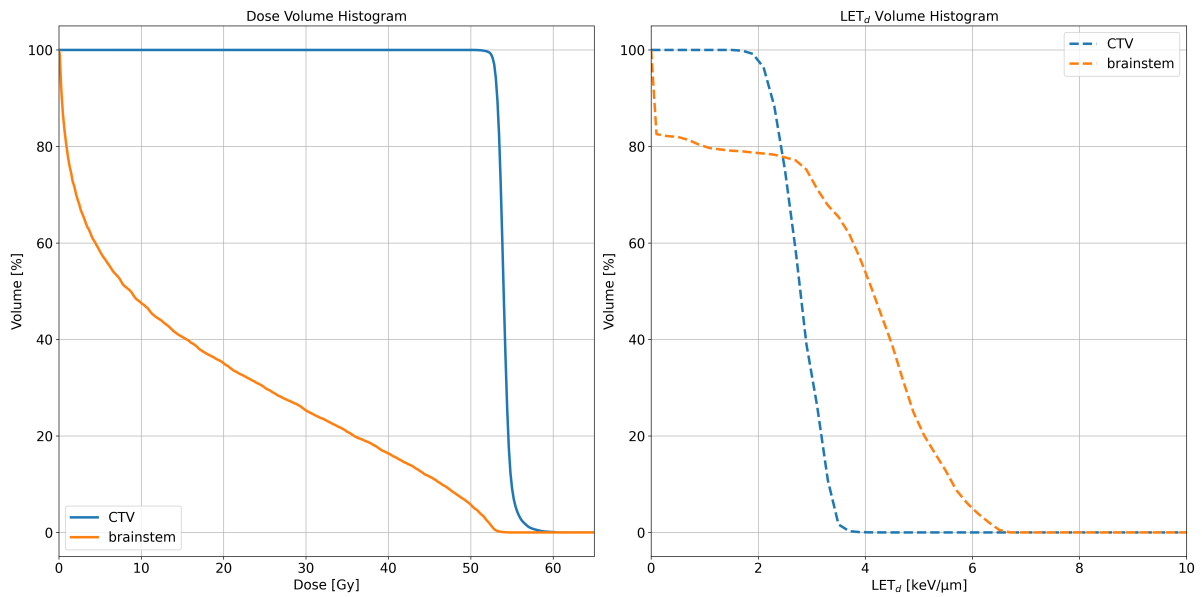


Figure 4.16: The dose volume histogram (left) and LET_d volume histogram (right) for the CTV and brainstem of the patient.

4.3.2 Single field evaluation of dose, LET_d and microdosimetry

It is useful to study one field at the time when interpreting the lineal energies. The dose, LET_d and lineal energies calculated in FLUKA for the field delivered posterior of the target, will now be presented.

In Figure 4.17 the dose- and LET_d -distributions calculated for the posterior field are displayed with a color wash for a slice in the patient. The figure shows high LET_d -values in the area beyond the range of the beams, illustrating that the LET_d rises towards the end of the SOBPs. A hot-spot of LET_d is seen in the brainstem.

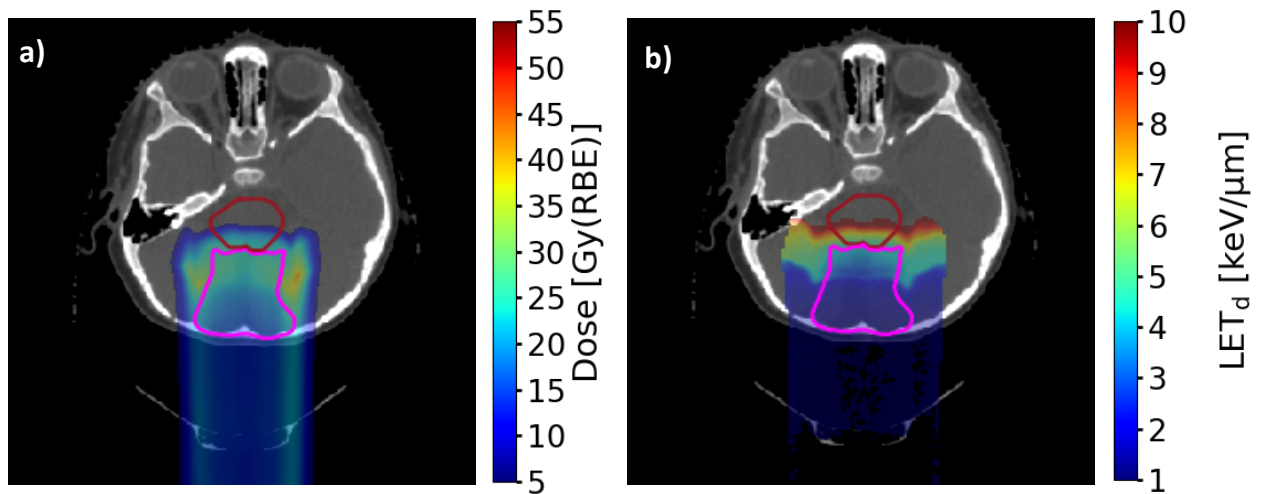


Figure 4.17: FLUKA recalculations of the posterior field in the patient treatment plan. The brainstem is contoured in red and the CTV in magenta. a) Biological dose (RBE 1.1) and b) LET_d .

In Figure 4.18 it can be seen that for all site sizes, the lineal energy rises from the CTV to the brainstem. Furthermore, it illustrates that the lineal energy in both ROIs decrease with site size. However, for the largest site size, it appears as if the lineal energy increases again in both ROIs.

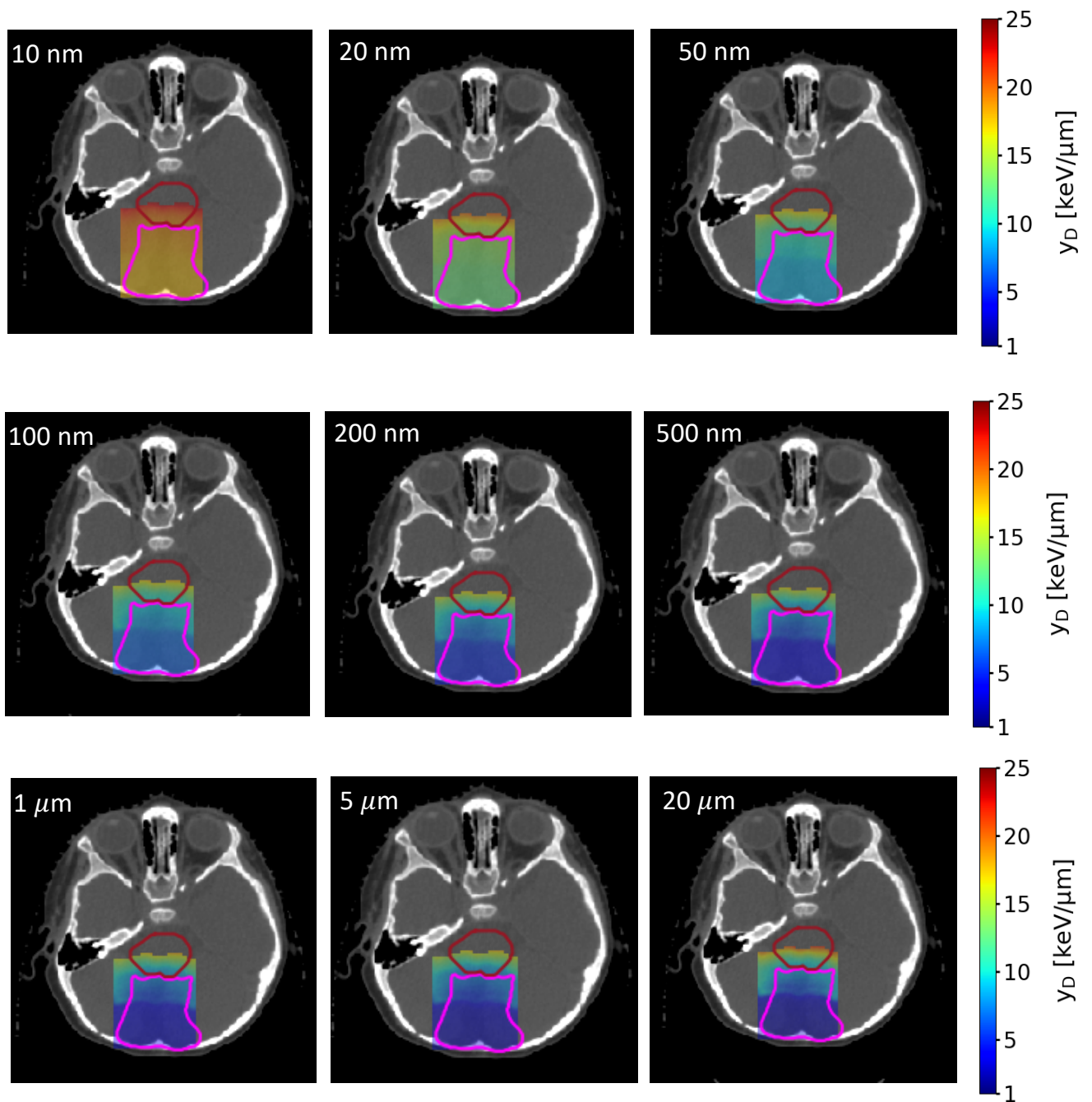
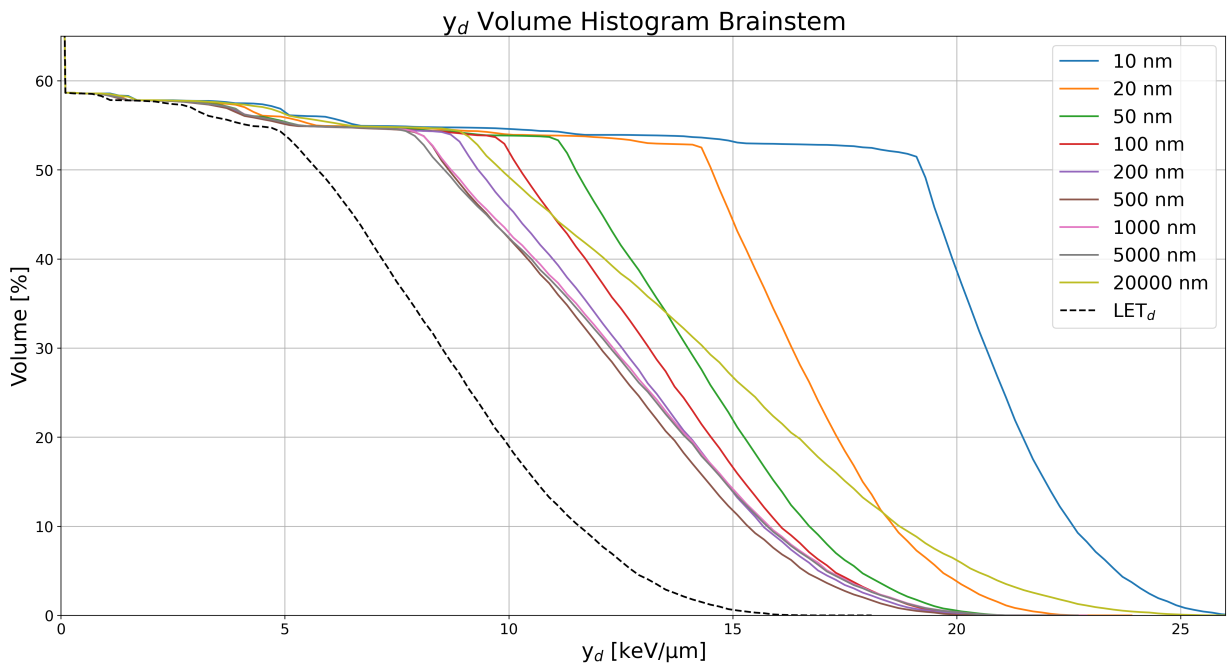


Figure 4.18: 2D distribution of the scored \bar{y}_D -values [keV/ μm] from the posterior field in the brainstem (red) and CTV (magenta) for site sizes 10 nm - 20 μm .

The \bar{y}_D VHs in the brainstem are calculated and plotted together with the LET_d VH for the brainstem in Figure 4.19. The \bar{y}_D and the LET_d to 50 % of the volume ($y_{50\%}$ and $L_{50\%}$) are summarized in Table 4.1.

Figure 4.19 confirms the observation from the 2D distributions, that the lineal energy rises again for the largest site size. The brainstem is located in the DDF, and as seen for the water phantom, the large site sizes have a drastic increase in \bar{y}_D in this area of the treatment field compared to the entrance. Furthermore, the $L_{50\%}$ of 5.7 keV/ μ m is remarkably lower than $y_{50\%}$ for all site sizes.



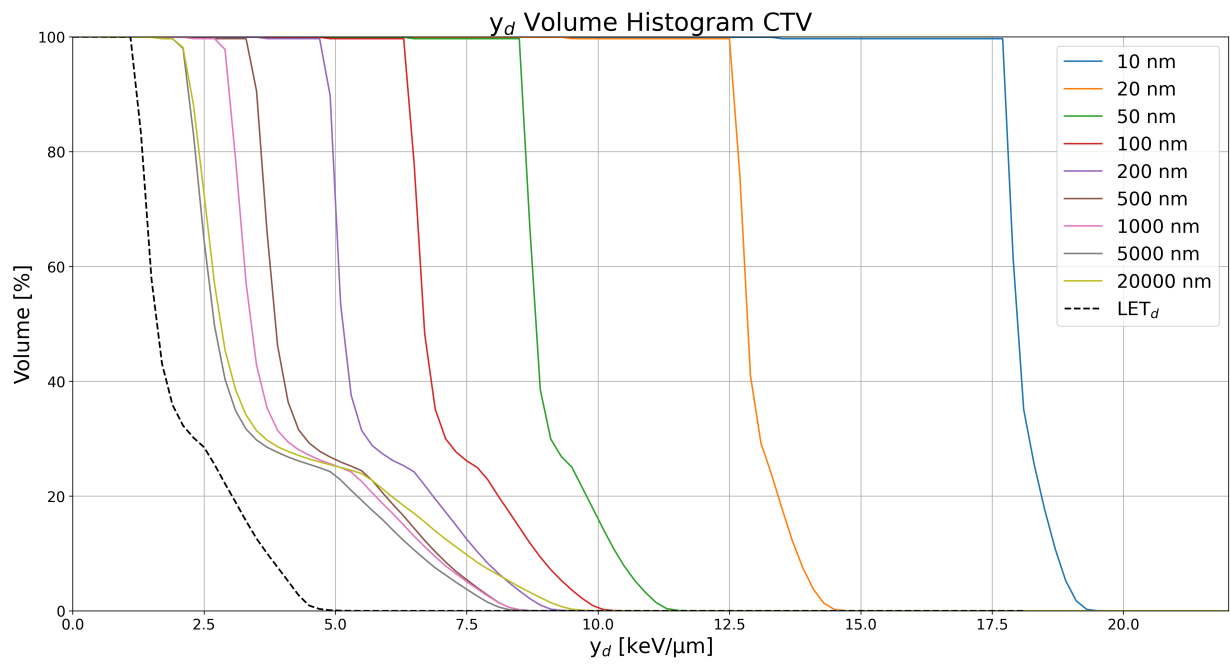
4.19: \bar{y}_D volume histogram for the brainstem for site sizes 10 nm – 20 μ m for the posterior field. The LET_d is plotted as a dashed line.

Table 4.1: The dose-mean lineal energy and the LET_d to 50 % of the volume ($y_{50\%}$ and $L_{50\%}$) for the brainstem and CTV. Values are given in keV/ μm .

	Brainstem	CTV
$y_{50\%}$ 10 nm	19.2	18.0
$y_{50\%}$ 20 nm	14.5	12.9
$y_{50\%}$ 50 nm	11.5	8.8
$y_{50\%}$ 100 nm	10.3	6.7
$y_{50\%}$ 200 nm	9.3	5.1
$y_{50\%}$ 500 nm	8.7	3.9
$y_{50\%}$ 1000 nm	8.7	3.4
$y_{50\%}$ 5000 nm	8.6	2.7
$y_{50\%}$ 20000 nm	9.8	2.8
$L_{50\%}$	5.7	1.6

In Figure 4.20 the calculated \bar{y}_D and LET_d VHs for the CTV are presented.

Firstly, $y_{50\%}$ is lower for the CTV than the brainstem for all site sizes, as shown in Table 4.1. Secondly, a larger spread in the \bar{y}_D between site sizes is seen in the CTV than in the brainstem. The $y_{50\%}$ for CTV ranges from 2.7 to 18.0 keV/ μm , while for the brainstem the range was from 8.6 to 19.2 keV/ μm . This agrees with the results found for the water phantom as the CTV is experiencing the entrance and the plateau of the SOBP, where a larger spread in \bar{y}_D between site sizes was seen compared to the DDF. Finally, $L_{50\%}$ of 1.6 keV/ μm is lower than the $y_{50\%}$ for all site sizes.



4.20: \bar{y}_D volume histogram for the CTV for site sizes 10 nm – 20 μm for the posterior field. The LET_d is plotted as a dashed line.

5. Discussion

A system for investigating the \bar{y}_D for multiple site sizes in OARs and other ROIs in clinical proton treatment plans has been developed in this project.

Lookup tables converting between proton energy and lineal energy distributions ($f(y)$) was created for proton energies from 1 to 100 MeV, by interpolating between data from former simulations in Geant4 DNA at the department[7]. 11 lookup tables were created, one for each of the studied site sizes ranging from 10 nm to 20 μm .

A methodology was developed for calculating the $f(y)$ in patient voxels based on the proton energy spectrum ($f(E)$) scored in the voxel. From the $f(y)$ s, the expectation values dose-mean lineal energy (\bar{y}_D) and frequency-mean lineal energy (\bar{y}_F) was calculated for the voxels. Finally, a mapping of the \bar{y}_D -values for different site sizes in the brainstem and CTV of a patient was provided.

5.1 Applicability of the developed system

As outlined in the project objectives (chapter 1.1), it is impractical and currently not feasible to recalculate a clinical proton treatment plan scoring the $f(y)$ in each clinical voxel. Therefore, many attempts to simplify the calculations of lineal energy in a clinical proton beam have been made.

Our approach to this was to use the proton energy spectrum in the voxel and “lookup” the $f(y)$ corresponding to these energies. It would be extraordinarily computationally demanding to simulate the $f(y)$ for all possible proton energies and site sizes[53].

Our solution to this was to interpolate between a few already existing $f(y)$ s to generate lookup tables for a wide range of proton energies.

5.1.1 Limitations of the lookup tables

Limitations of the interpolation model

A relatively simple approach was taken when interpolating between the $f(y)$ s from the GATE data. The interpolation method is described in chapter 3.1. Certainly, there exist more advanced methods for interpolation that possibly could have improved our lookup tables. The interpolation model shows errors for large sites and low proton energies, as presented in chapter 4.1. It appears that in the interpolation model the microdosimetric spectra with the highest lineal energies are weighted the most. We believe this fosters a slight overestimation of the \bar{y}_D -value calculated with our system. This possible overestimation needs to be taken into account when interpreting the lineal energies scored in the brainstem.

When it was discovered that the interpolation model possibly causes an overestimation, it was not prioritized to develop a new one. It was considered more important to build the framework of the methodology and test it, because the main purpose of this thesis was to implement a method for accessing lineal energy in recalculation of treatment plans in FLUKA. In future work, replacing the interpolation model would be an effective way to improve the method and increase the correctness of the calculated lineal energies. Alternatively, to avoid interpolation or at least reduce its attendance in the lookup tables, $f(y)$ for several energies must be simulated in Geant4 DNA.

When studying Figure 4.4 where the interpolated \bar{y}_D -values are shown, the question rises if we not would have gotten better values if we simply used linear interpolation between the \bar{y}_D -values in the GATE data. With linear interpolation, the curves would loose their bending seen for proton energies above 20 MeV and sites larger than 100 nm due to the overestimation in the applied interpolation model. Thus, we might obtain more accurate \bar{y}_D -values with linear interpolation. With these \bar{y}_D -values we could still have provided a mapping of the \bar{y}_D in the brainstem and CTV in clinical treatment plans. However, lineal energy is a stochastic quantity and the \bar{y}_D is simply

the expectation value from the dose distribution $d(y)$. Thus, we considered that we would preserve most of the physical information in the GATE data if we interpolated between the spectra. Furthermore, it was in our interest to be able to plot the microdosimetric distributions in voxels in the treatment plans.

In Figure 4.11 the microdosimetric spectrum, $yd(y)$, for site size $20 \mu\text{m}$ had an unexpected appearance with multiple peaks and this effect was most prominent in the low-energy region of the SOBP. The multi-peak appearance originates from the way these $yd(y)$ were calculated. The calculated spectra are the result from summation of several monoenergetic $f(y)$ s from the lookup table. The lookup table consists mainly of interpolated spectra that for low energies and large site sizes often has two distinct peaks, one from each of the two spectra it is interpolated from. As discussed in chapter 4.1.1 this happens when the distance between the original spectra is large, as it is for large sites and low energies. However, even though the appearance of the $yd(y)$ for large sites and low energies are wrong, the calculated \bar{y}_D -values might not be so far from a true value. Because the broad single peak of the true spectrum would probably lie in between the distinct peaks and \bar{y}_D is the average of the spectrum. We did not find any \bar{y}_D -values calculated in a clinical proton beam for site sizes above $1 \mu\text{m}$ to compare our values to. However, for the smallest site sizes we were able to compare our calculated \bar{y}_D -values to work of others.

Comparison to \bar{y}_D -values in work of others

Although, no mapping of the lineal energy from a proton treatment field in the brainstem was found in literature, several publications on microdosimetric calculations in clinical proton beams relevant for comparison to our work, were found [25, 54].

Liamsuwan et al. [25] used MC track structure models to investigate the frequency of energy depositions in nanometer size targets and calculated the \bar{y}_D and \bar{y}_F for proton energies overlapping with those studied in this project. Their work showed the same

trends as the \bar{y}_D - and y_F - values in our lookup tables (Figure 4.4 and 4.5). They found that \bar{y}_D and \bar{y}_F decreased with site size, except for proton energies below $\sim 3\text{MeV}$ where the \bar{y}_D of the largest site were highest. Additionally, the site dependency of the \bar{y}_D - and \bar{y}_F -values increased with proton energy. This agrees with our findings in the brainstem and CTV, where the spread in VHs of \bar{y}_D for different site sizes were larger in the high-dose region CTV (Figure 4.20) compared to the low-dose region brainstem (Figure 4.19).

In other published work[54], Liamsuwan et al. calculated through MC track structure codes, the microdosimetric properties in a 160 MeV proton beam irradiating a water phantom. As we simulated a SOBP with proton beam energies 105-131 MeV rather than a monoenergetic beam, a quantitative comparison is challenging. However, the overall trends and behavior found in the two studies can be compared. Liamsuwan et al. calculated \bar{y}_D and \bar{y}_F along the beam path for 10 and 100 nm site sizes and compared to the LET_d and dose-depth profiles. Their results are presented in Figure 5.1. In accordance to our results (Figure 4.13), they saw a relatively flat curve for both 10 and 100 nm, with a steeper rise toward the Bragg peak for the larger site size. Reading from the plot in Figure 5.1, the entrance value of \bar{y}_D for 10 nm site size is $\sim 18\text{ keV}/\mu\text{m}$ and peaks at $\sim 25\text{ keV}/\mu\text{m}$ and for 100 nm curve the entrance value is $\sim 6\text{ keV}/\mu\text{m}$ and the peak is at $\sim 19\text{ keV}/\mu\text{m}$. These values appear to be the same as in our results and thus it makes us confident that we have calculated reasonable \bar{y}_D -values in the SOBP of the water phantom for site sizes 10 and 100 nm.

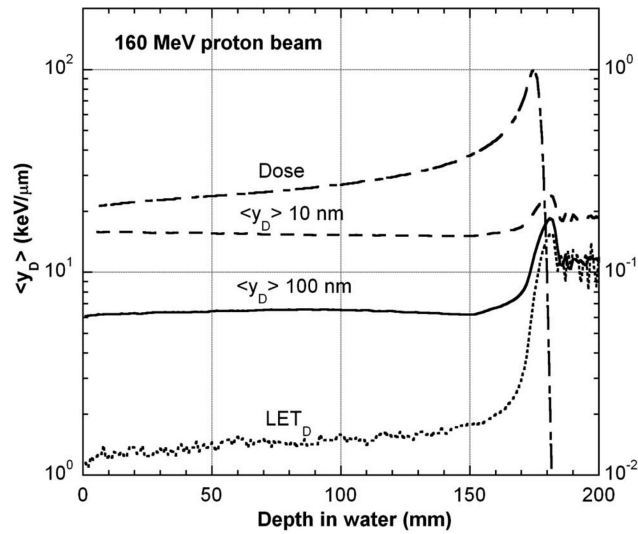


Figure 5.1: The dose mean lineal energy, \bar{y}_D , at depths relative to the Bragg peak. \bar{y}_D were determined in cylinders of equal diameters and lengths 10 and 100 nm for a 160 MeV/u proton beam. Also shown are the dose-averaged LET, LET_D , and absorbed dose depth profiles of the proton beam. The Figure is reprinted from Liamsuwan et al. (2014)[54] with permission from John Wiley and Sons.

Limitations of Geant4 DNA

The lookup tables are solely based on data from TS MC codes and in all such calculations, one must acknowledge the intrinsic uncertainty that comes with these models. Incerti et al. provided a review of the application of Geant4 DNA in TS simulations on the subcellular level[43]. They underline that even though Geant4 DNA has been benchmarked against other TS codes and experimental data, it operates in a very low energy region where there is significant theoretical and experimental complexity and that sometimes approximations, assumptions and semi-empirical models must be used by the code to simplify. Due to practical constraints, there is a lack of measurements in the energy region below 100 eV which is needed to fully validate the models in Geant4 DNA against experimental data. It is expected that Geant4 DNA and other TS codes will see further developments in the years to come and that they will continue to be indispensable tools in radiotherapy research. Furthermore, individual simulation choices in Geant4 DNA might foster differences between individual studies.

5.1.2 Limitations of the energy scoring

If the proton energy spectra, $f(E)$, is to be used in the clinic for microdosimetric assessment of proton treatment plans, there must be an efficient workflow for recording the energy spectrum and converting it to microdosimetric information through lookup tables.

The simulations in FLUKA where energy was scored in the voxels of the brainstem and the CTV, were time consuming. For example, it took seven hours to simulate the 480 million primary protons in the brainstem. This was even when the simulation was divided on 48 cores simulating ten million primary protons each. To split the simulation on several cores, even though it requires some extra preprocessing of the data afterwards, is essential.

It was expected that the FLUKA simulations would need to run for several hours. However, another part of our methodology was unexpectedly time consuming, namely the division of energy scorings into energy bins to obtain the $f(E)$. For example, for the brainstem, it took 13 hours to bin the 59 GB of simulation data and create the $f(E)$ in each of the 13 456 voxels of the brainstem. This process was performed in python and python documentation reports that the process of binning large amount of data is a time consuming process and it is hard to avoid long computational times.

In future work the creation of the $f(E)$ should be made more effective. Instead of writing each energy scoring to a file, the histograms should be built directly. When an energy is scored in a voxel in FLUKA, this energy should be added to the histogram for that voxel. Then when the simulation has run long enough, the $f(E)$ is complete. It should be investigated if the fluscw user routine could be designed to perform this operation. With this approach the memory issue would be solved as the size of the simulation data would be much smaller than in the current approach. The size would

be the number of voxels times the number of bins. We believe it is a good approach to continue with the 100 energy bins used in this project. Furthermore, the simulation data would not increase with more primaries, as it would only increase the count in each bin. Thus, high statistics could be obtained without the data size becoming impractically large.

5.1.3 Approaches by others

Parisi et al.[6] postulated that using a limited amount of lineal energy bins rather than storing the whole spectral information in a voxel, would be a reasonable approximation that could be used for calculating the RBE. In their work they summarized the microdosimetric spectra by dividing it into 10 lineal energy bins. They calculated the \bar{y}_D in a water phantom for input to an RBE-model with the whole spectral information as input and compared to the RBE values they calculated when the microdosimetric distributions were summarized with only the 10 lineal energy bins. Their work showed excellent agreement between the RBE values computed in the two different ways. Although this work was intended for clinical application in carbon therapy, their promising results showing that the \bar{y}_D calculated with limited spectral information might estimate the RBE well, can be adapted to proton therapy.

A different approach, resembling more to the method used in our project, was taken by Newpower et al.[55] and DeCunha et al.[53] They both used the proton energy spectrum to calculate the microdosimetric spectra with the intention of using this for calculating the lineal energy in patient voxels and as an input to RBE models. The method of summing the $f(y)$ s of monoenergetic proton beams to yield the $f(y)$ of a polyenergetic beam was proposed by Newpower et al. in the article published in 2019. DeCunha et al. applied this method in their methodology where they calculate the $f(y)$ in targets of interest by the use of a library of $f(y)$ for monoenergetic protons. The library is intended to be integrated in a TPS someday. The idea of such a

library to enable for rapid determination of microdosimetric spectra in a clinical environment, resemble the idea of the lookup tables in this project.

The lookup tables generated in our work map the $f(y)$ for proton energies 1 to 100 MeV and site sizes 10 nm to 20 μm . The library developed by DeCunha et al. included proton energies down to 0.1 MeV and site sizes down to 1 nm. Similar to our work, their library had 1 MeV increments between 1 and 100 MeV. Their library consisted of 8502 $f(y)$ s for different proton energies and site sizes, compared to the 1100 $f(y)$ s constituting the lookup tables in our work (11 site sizes and 100 energies for each site size). To overcome the computational challenge of creating such a collection of $f(y)$ s, they developed what they termed a GPU-accelerated method.

The energy range 1-100 MeV in our lookup tables was decided based on the energy range in GATE data, which was limited to this range because the physics package Geant4 DNA at the moment had an upper limit of 100 MeV for protons. As DeCunha et al. used the same simulation software and physics package, their library had the same upper limit for the same reason. 1 MeV was set as a lower limit when the GATE data was created because the energy deposition from protons with lower energies is so small that it is considered negligible for the dose[7]. This does not mean that the dose from protons with energy below 1 MeV is ignored in our system, but rather that no particular weighting factor is applied to these protons when describing the radiation quality.

Additional differences between our system and the one developed by DeCunha et al. is seen in the way the lineal energy of the monoenergetic proton tracks were recorded in Geant4 DNA. This difference might affect which system is most applicable for clinical use. The energy of a proton changes rapidly while it travels through tissue and it is thus a challenge to record the lineal energy of a proton before its velocity (energy) is changed. DeCunha et al. approached this by simulating the proton tracks in volumes with the same size as voxels in TPSs. They suggest that if the energy of a

proton entering a patient voxel is known, their system can calculate the lineal energy that this proton track will have as it traverses the patient voxel. This voxel was cubical with side length 3 mm.

In our methodology however, the proton is sent through a buildup region before its lineal energy is scored. The volume in which the lineal energy is scored is much smaller than a TPS voxel. The small voxel should ensure that the proton energy does not change very much while traversing it and thus the lineal energy scored can be considered the lineal energy of a monoenergetic proton track.

We compared our \bar{y}_D -values to those calculated by DeCunha et al. shown in Figure 5.2. These curves resemble ours in Figure 4.4, but a steep fall-off is seen in their curves at the 17 MeV which is the energy at which protons can escape the 3 mm long voxel. This drop in \bar{y}_D happens when the end of the protons range, where the lineal energy is highest, no longer occurs inside the voxel, as explained by DeCunha et al.

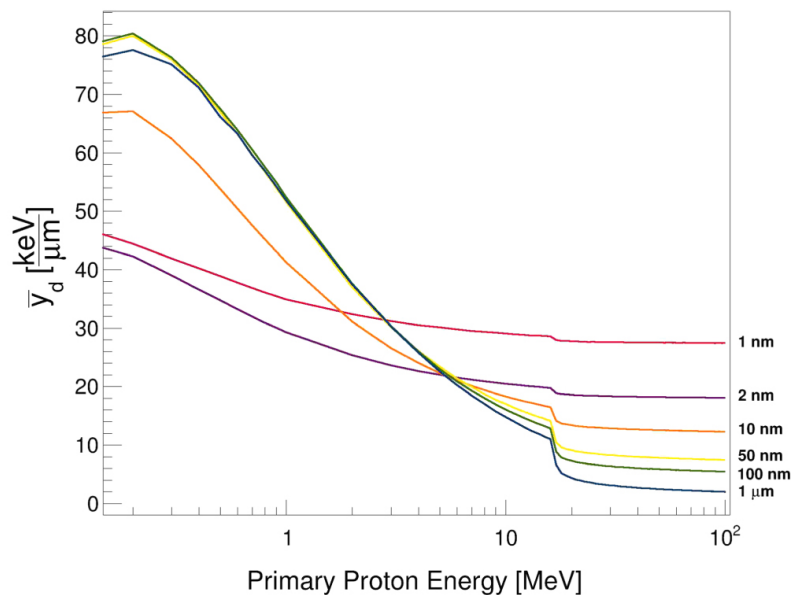


Figure 5.2: \bar{y}_D -values calculated for proton energies 0.1-100 MeV in a 3 mm cubical voxel by a methodology proposed by DeCunha et al [53]. Lines corresponding to different site sizes. A steep fall-off is seen at proton energy 17 MeV. The figure is reprinted from DeCunha et al. (2023) [53] with permission from IOP publishing.

Neither their nor our system is mature enough and ready for integration with a TPS. This made it challenging to perform any further comparison between the systems. It would be of great interest to recalculate the same treatment plan with both systems and investigate the calculated \bar{y}_D -distributions in the brainstem. Anyways, further investigations are needed to detect any eventual pitfalls of either methodology before collections of $f(y)$ s can be integrated in commercial TPSs for rapid determination of \bar{y}_D in clinical treatment plans.

5.2 Biological relevance of site sizes

11 site sizes ranging from 10 nm to 20 μm was studied in this project. When the GATE data was created, the ambition was to provide a mapping of lineal energies for a wide range of proton energies and site sizes. Microdosimetric research through the years has shown that there is apparently no single site size that can be used to describe all biological effects of radiation[12, 29]. And it is therefore of great interest to study a wide range of site sizes for a further understanding of the biological effects of radiation.

Fitting to biological models

In attempts to locate the site size that most readily can be associated with biological effect, numerous studies have investigated which size gives the best fit for biological models. Lindborg et al.[56] presented results supporting that site sizes in the range 10-15 nm are relevant for describing the rate of complex DSB of the DNA for different radiation qualities. They calculated the y_D for proton, carbon, neutron and photon beams and used it as input to the LQ-model for calculating the α -value. A proportional relationship was found between the α -ratio and the y_D -ratio (relative to the y_D of gamma radiation) for 10-15 nm sites. Larger site sizes, however still at the nanometer scale, appeared to be relevant in a study by Newpower et al.[55]. They studied proton RBE experiments for various cell lines, where the RBE was measured

at several locations along the Bragg curve. They calculated the y_D at the same positions and used it as input for the MKM to predict RBE. Site sizes between 200 and 500 nm gave the best agreement between the experimental RBE and the MKM-predicted RBE. Other studies have found similar site sizes when applying the MKM to proton RBE experiments[57, 58].

Site sizes below 10 nm

Other studies of microdosimetric properties of proton beams considers also site sizes < 10 nm. Liamsuwan et al.[25] simulated proton tracks and studied their microdosimetric properties in site sizes down to 2 nm, and other studies[53] included site sizes down to 1 nm. The smaller the site size is, the more computational demanding is the simulation as the level of precision needs to be extremely high. As the purpose of this project is to study a wide range of site sizes, it was prioritized in the creation of the GATE data to simulate many different site sizes in both nanometer and micrometer range, rather than simulating several sites below 10 nm. Zaider and Rossi[36] point to the fact that when distances become smaller than the ~ 2 nm long diameter of the DNA helix, one approaches quantum mechanical limits for the precise determination of the transfer points. And that these dimensions are uninteresting as one would find only single transfer points, which are essentially the same for all ionizing radiation. Thus, they argue that such site sizes are too small for microdosimetry as it studies the spatial aggregation of transfer points.

Variation between site sizes in this project

The results in this thesis presented a large spread between the calculated \bar{y}_D -values in the brainstem among the different site sizes studied (Figure 4.19). This illustrates that the biological effect is described unlike by these different radiation quality measures. Only one of them can truly represent the biological effect in the brainstem, but which one remains an unanswered question. However, what might provide more

insight to this question, is studying whether some of the site sizes show a linear relationship with the RBE.

In Figure 5.2 the curves from Figure 4.13, where the LET_d and \bar{y}_D measured in the SOBP in the water phantom was plotted against depth, is divided by their entrance value. The growth factor is shown for each curve. This plot clearly depicts how the \bar{y}_D measured in a 10 nm site reports a relatively constant ionization density with a growth factor of 1.5 from entrance to DDF. In contrast, the \bar{y}_D of the largest site, 20 μm , reports a dramatic increase with a growth factor of 8.4. The relative increase with depth is found to increase with site size. Furthermore, the LET_d -curve shows the largest increase among all with a growth factor of 13.7. This implies that the LET is much more variable along the SOBP than the lineal energy, even for large sites.

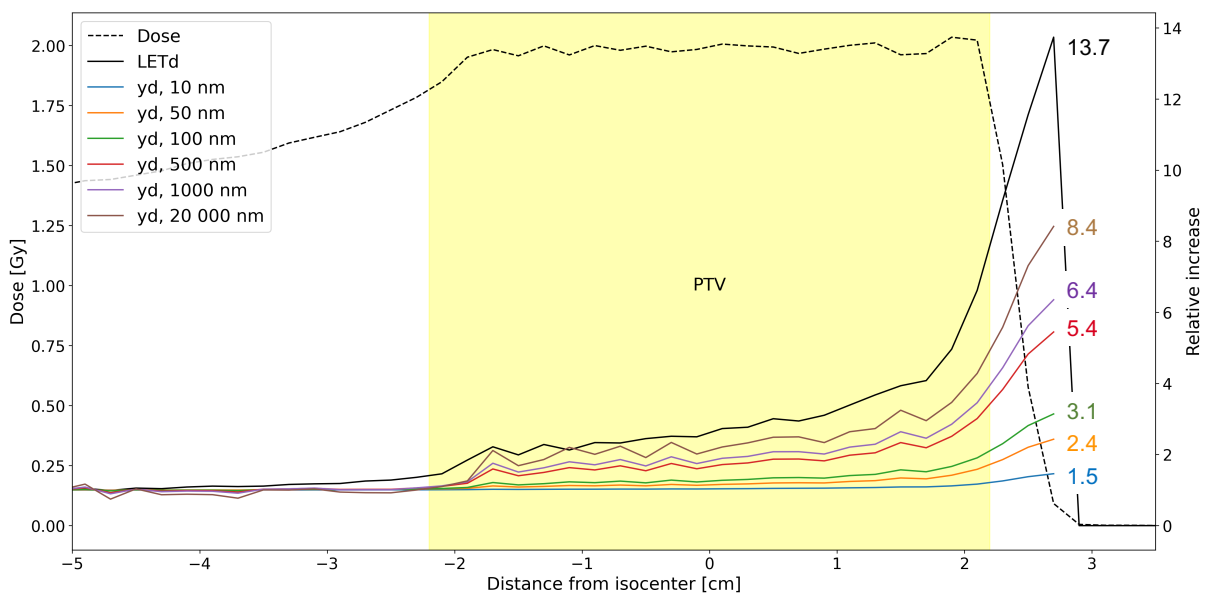


Figure 5.2: For the water phantom is shown the relative increase with depth in LET_d and \bar{y}_D for different site sizes 10 nm – 20 μm . The growth factor is printed for each curve. The dose from the SOBP is illustrated with a dashed line. *Abbreviations:* SOBP = Spread out Bragg Peak, LET_d = dose-averaged LET, \bar{y}_D = mean-dose lineal energy.

If we assume that an increase in radiation quality measured in $\text{keV}/\mu\text{m}$ corresponds to some increase in biological effect measured by RBE, the more or less flat curve in Figure 5.2, belonging to the 10 nm site, is in good accordance with the constant RBE

of 1.1 applied in proton therapy clinics. Furthermore, even though not clearly visible in the figure, the curve has a slight increase at the end of the SOBP, which is in accordance with research reporting an increase in the biological effect at the end of the proton beam[5, 8-11]. This might suggest that the 10 nm site is a better predictor of the RBE than large sites and possibly also the LET_d .

5.3 Macroscopic (LET_D) versus microdosimetric (\bar{y}_D) quantities for radiation quality

Figure 5.2 illustrates a particular difference in the variation in keV/ μm during the SOBP for the LET_d and the microdosimetric quantities.

In a study by Chattaraj et al.[59] they estimated the RBE with both microdosimetry-based RBE models and RBE models using the LET_d as input. Their calculated RBE-values at several positions along a 100 MeV proton SOBP in a water phantom is presented in Figure 5.3. Two microdosimetric models were included, one of them the MKM and the other, denoted as RBE_r in the figure, is a microdosimetric model for RBE that is independent of dose. The microdosimetric models, MKM for a prescribed dose of 2 Gy, $RBE_{MKM}(2 Gy)$, MKM for prescribed dose 4 Gy, $RBE_{MKM}(4 Gy)$, and RBE_r , reports a moderate increase in RBE. The other models, which are based on the LET_d , show a larger relative increase in RBE towards the end of the SOBP.

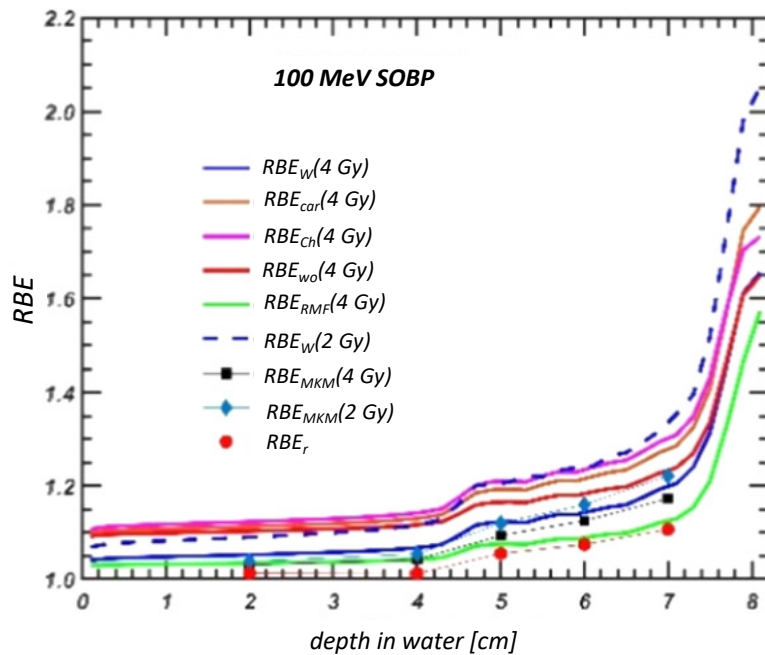


Figure 5.3: Calculated RBE values in a 100 MeV SOBP in a water phantom plotted against depth. Values are calculated for several RBE-models, there among the microdosimetry-based models MKM for a prescribed dose of 2 Gy (blue triangles), the MKM for a prescribed dose of 4 Gy (black squares) and RBE_r (red circles). The other curves belongs to LET_d -based models. The figure is reprinted from Chattaraj et al. (2024) [59] with permission from IOP Publishing.

Some similarities can be seen between the RBE-curves in Figure 5.3 and the curves illustrating relative increase in the radiation quality in Figure 5.2. The three RBE-curves calculated with the microdosimetric models show a more flat development in depth than the other curves. This might imply that the relationship between LET_d and RBE is more complex than between lineal energy and RBE. If so, the advantage of microdosimetry would be that it could provide easier RBE models which might be more precise than LET-based models with many complex parameters.

The figure illustrates a variation in the RBE estimated by the models and the question is still which of these models predicts values that are closest to the true effects in tissue. It is hard to find a clear answer to this, as experimental research with cell radiation reports different RBE values for the same cell lines[10]. This inconsistency

in the reported RBE hinders any consensus on the RBE-weighting factors to be used in clinics at any depth in the dose profile.

Magrin et al. states in a review[60] concerning the potential of microdosimetry in proton therapy, that it seems unfeasible to select a unique quantity, either LET or y , for the characterization of the radiation quality in clinics. They point to the advantages of y being that it provides a description of the radiation which resembles better with the behavior of the secondary electrons on a cellular target and that it is a directly measurable quantity while LET is not. The LET however, has the advantage of being already implemented in TPSs and it tends to become the standard way of referring to the radiation quality by the medical community. Furthermore, Magrin et al. point out that LET based optimization has become an important tool for the novel treatment technique proton arc therapy. In the review they therefore suggest that microdosimetry should be an experimental tool in clinics for validating the LET_d distributions calculated by TPS. They underscore the need for such validation by referring to a recent study[61] among eight European proton centers which reported variations in LET_d based on averaging technique, simulation environment and the secondary particles considered. Magrin et al. stresses that microdosimetry needs to overcome some practical challenges in terms of detector design before it is fully applicable in quality assurance of a clinical proton beam. The distal edge of the Bragg peak is very steep with a rapid change in radiation quality. It is practically impossible to achieve high enough position accuracy for different dosimeters relative to each other due to unavoidable beam positioning uncertainties.

Magrin et al. furthermore underscores the importance of microdosimetry in giving further insight to the clinical relevance of the increase in LET seen in the DDF. They suggest that retrospective studies considering the microdosimetric spectra, resembling recent retrospective studies[62, 63] based on LET_d should be conducted. This could

provide links between the clinical outcome and the microdosimetric spectra, possibly highlighting some effects that was hidden behind the average value LET_d .

It would be highly interesting to apply our system in a study on brainstem necrosis in pediatric proton therapy patients. The \bar{y}_D -distribution in the brainstem should be calculated and a potential correlation between \bar{y}_D and necrotic tissue in the voxels, should be investigated. Furthermore, the dependency on site size should be explored to reveal any possible links between site size and the observed biological effect.

6. Conclusions

In this project, a methodology for scoring microdosimetric quantities in voxels of a clinical proton treatment plan has successfully been developed. A method for scoring the proton energy spectra was established and allowed us to map microdosimetric quantities in the brainstem and CTV of a pediatric patient from a clinical proton treatment plan.

The computed microdosimetric spectra for small site sizes (10-100 nm) show agreement when comparing to microdosimetric calculations made by others in clinical proton beams. Furthermore, the trends of increased \bar{y}_D in the DDF and a shift in the microdosimetric spectra towards higher lineal energies towards the end of the SOBP, align with experimental measurements of clinical proton beams.

Some limitations of the system were detected. The interpolated \bar{y}_D -values were slightly overestimated for large site sizes and low proton energies. Furthermore, the method for energy scoring was too slow to be applicable in a clinical setting for rapid determination of the lineal energies in a patient treatment plan. However, this work provides an excellent framework for a system that can provide microdosimetric assessment of clinical proton treatment plans. The system could effectively be improved with updated lookup tables once such are available.

References

1. Robertson, J.B., et al., *Radiobiological studies of a high-energy modulated proton beam utilizing cultured mammalian cells*. *Cancer*, 1975. **35**(6): p. 1664-1677.
2. Urano, M., et al., *Relative biological effectiveness of modulated proton beams in various murine tissues*. *International Journal of Radiation Oncology*Biology*Physics*, 1984. **10**(4): p. 509-514.
3. Paganetti, H., *Relative biological effectiveness (RBE) values for proton beam therapy. Variations as a function of biological endpoint, dose, and linear energy transfer*. *Phys Med Biol*, 2014. **59**(22): p. R419-72.
4. Wang, C.C., et al., *End-of-Range Radiobiological Effect on Rib Fractures in Patients Receiving Proton Therapy for Breast Cancer*. *Int J Radiat Oncol Biol Phys*, 2020. **107**(3): p. 449-454.
5. Underwood, T., et al., *OC-0245: Clinical evidence that end-of-range proton RBE exceeds 1.1: lung density changes following chest RT*. *Radiotherapy and Oncology*, 2017. **123**: p. S123-S124.
6. Parisi, A., C.J. Beltran, and K.M. Furutani, *A methodology to abridge microdosimetric distributions without a significant loss of the spectral information needed for the RBE computation in carbon ion therapy*. *Journal of Applied Clinical Medical Physics*, 2023. **24**(7): p. e14049.
7. Folkedal, E.J., *Monte Carlo based mapping of proton microdosimetric properties*, in *Department of physics and technology*. 2022, University of Bergen.
8. Gerweck, L.E. and S.V. Kozin, *Relative biological effectiveness of proton beams in clinical therapy*. *Radiotherapy and Oncology*, 1999. **50**(2): p. 135-142.
9. Courdi, A., et al., *The depth-dependent radiation response of human melanoma cells exposed to 65 MeV protons*. *The British journal of radiology*, 1994. **67**(800): p. 800-804.
10. Britten, R.A., et al., *Variations in the RBE for cell killing along the depth-dose profile of a modulated proton therapy beam*. *Radiat Res*, 2013. **179**(1): p. 21-8.
11. Peeler, C.R., et al., *Clinical evidence of variable proton biological effectiveness in pediatric patients treated for ependymoma*. *Radiother Oncol*, 2016. **121**(3): p. 395-401.
12. Lindborg, L. and A. Waker, *Microdosimetry Experimental Methods and Applications*. 2017.
13. *Linear Energy Transfer* 1970, International Commission on Radiation Units and measurements (ICRU).
14. *Relative Biological Effectiveness in Ion Beam Therapy*. 2008, Vienna: INTERNATIONAL ATOMIC ENERGY AGENCY.
15. Paganetti, H., *Proton Therapy Physics*. 2012: CRC Press.
16. Newhauser, W., *International Commission on Radiation Units and Measurements Report 78: Prescribing, Recording and Reporting Proton-beam Therapy*. *Radiation Protection Dosimetry*, 2009. **133**(1): p. 60-62.
17. Newhauser, W.D. and R. Zhang, *The physics of proton therapy*. *Physics in Medicine & Biology*, 2015. **60**(8): p. R155.

18. Paganetti, H., *Proton Therapy Physics*. 2nd ed. 2020: CRC Press.
19. Leo, W.R., *Techniques for Nuclear and Particle Physics Experiments : A How-To Approach*. 1994, Berlin, Heidelberg, GERMANY: Springer Berlin / Heidelberg.
20. ICRU, *Secondary Electron Spectra from Charged Particle Interactions*. ICRU report, 1996. **55**.
21. Burigo, L., et al., *Microdosimetry spectra and RBE of 1H, 4He, 7Li and 12C nuclei in water studied with Geant4*. Nuclear Instruments and Methods in Physics Research Section B: Beam Interactions with Materials and Atoms, 2014. **320**: p. 89-99.
22. Mayles, P., A. Nahum, and J.-C. Rosenwald, *Handbook of Radiotherapy Physics: Theory and Practice*. 2007 Boca Raton: CRC Press.
23. de Vera, P., I. Abril, and R. Garcia-Molina, *Energy Spectra of Protons and Generated Secondary Electrons around the Bragg Peak in Materials of Interest in Proton Therapy*. Radiation Research, 2018. **190**(3): p. 282-297.
24. Alizadeh, E. and L. Sanche, *Low-energy-electron interactions with DNA: approaching cellular conditions with atmospheric experiments*. The European Physical Journal D, 2014. **68**(4): p. 97.
25. Liamsuwan, T., et al., *Physical and biophysical properties of proton tracks of energies 1 keV to 300 MeV in water*. International Journal of Radiation Biology, 2011. **87**(2): p. 141-160.
26. *Ny kreftsykdom (sekundær kreft)*. 08.11.23 [cited 2024; Available from: <https://kreftforeningen.no/om-kreft/senskader-voksne/ny-kreftsykdom-sekundaer-kreft/>].
27. Hoskin, P., *External Beam Therapy*. 2012: OUP Oxford.
28. Rossi, H.H. and M. Zaider, *Elements of microdosimetry*. Medical Physics, 1991. **18**(6): p. 1085-1092.
29. Goodhead, D.T., *Energy deposition stochastics and track structure: what about the target?* Radiat Prot Dosimetry, 2006. **122**(1-4): p. 3-15.
30. Baatout, S., *Radiobiology Textbook*. 2024: Springer International Publishing.
31. Goodhead, D.T., *Initial events in the cellular effects of ionizing radiations: clustered damage in DNA*. Int J Radiat Biol, 1994. **65**(1): p. 7-17.
32. McMahan, S.J., *The linear quadratic model: usage, interpretation and challenges*. Physics in Medicine & Biology, 2019. **64**(1): p. 01TR01.
33. Chaudhary, P., et al., *Relative biological effectiveness variation along monoenergetic and modulated Bragg peaks of a 62-MeV therapeutic proton beam: a preclinical assessment*. Int J Radiat Oncol Biol Phys, 2014. **90**(1): p. 27-35.
34. Rørvik, E., et al., *Exploration and application of phenomenological RBE models for proton therapy*. Physics in Medicine & Biology, 2018. **63**(18): p. 185013.
35. Bertolet, A., M.A. Cortés-Giraldo, and A. Carabe-Fernandez, *On the concepts of dose-mean lineal energy, unrestricted and restricted dose-averaged LET in proton therapy*. Physics in Medicine & Biology, 2020. **65**(7): p. 075011.
36. Zaider, M., B.H.H. Rossi, and M. Zaider, *Microdosimetry and its Applications*. 1996: Springer.
37. Ahmed, S., *Naeem Physics and Engineering of Radiation Detection* 2nd ed. 2015: Elsevier

38. Inaniwa, T., et al., *Reformulation of a clinical-dose system for carbon-ion radiotherapy treatment planning at the National Institute of Radiological Sciences, Japan*. *Phys Med Biol*, 2015. **60**(8): p. 3271-86.
39. Hawkins, R.B., *A statistical theory of cell killing by radiation of varying linear energy transfer*. *Radiat Res*, 1994. **140**(3): p. 366-74.
40. Bellinzona, V.E., et al., *Linking Microdosimetric Measurements to Biological Effectiveness in Ion Beam Therapy: A Review of Theoretical Aspects of MKM and Other Models*. *Frontiers in Physics*, 2021. **8**.
41. Hawkins, R.B., *A Microdosimetric-Kinetic Model for the Effect of Non-Poisson Distribution of Lethal Lesions on the Variation of RBE with LET*. *Radiation Research*, 2003. **160**(1): p. 61-69.
42. Seco, J. and F. Verhaegen, *Monte Carlo Techniques in Radiation Therapy*. 1st ed. *Imaging in Medical Diagnosis and Therapy*. 2013: CRC Press.
43. Incerti, S., et al., *Review of Geant4-DNA applications for micro and nanoscale simulations*. *Physica Medica*, 2016. **32**(10): p. 1187-1200.
44. Nikjoo, H.G., D T, *Track structure analysis illustrating the prominent role of low-energy electrons in radiobiological effects of low-LET radiations*. *Physics in Medicine and Biology*; (UK), 1991. **36**:2.
45. Böhlen, T.T., et al., *The FLUKA Code: Developments and Challenges for High Energy and Medical Applications*. *Nuclear Data Sheets*, 2014. **120**: p. 211-214.
46. Ferrari, A., P. Sala, and A. Fassò, *FLUKA: a multi-particle transport code (Program version 2023)*. 2023, CERN, INFN.
47. Papiez, L. and J.J. Battista, *Radiance and particle fluence*. *Physics in Medicine & Biology*, 1994. **39**(6): p. 1053.
48. Fjæra, L.F., et al., *Linear energy transfer distributions in the brainstem depending on tumour location in intensity-modulated proton therapy of paediatric cancer*. *Acta Oncol*, 2017. **56**(6): p. 763-768.
49. Berger, M.J., et al. *Stopping-Power & Range Tables for Electrons, Protons, and Helium Ions*. 2017 July 2017; Available from: <https://www.nist.gov/pml/stopping-power-range-tables-electrons-protons-and-helium-ions>.
50. Schneider, U., et al., *Neutrons in proton pencil beam scanning: parameterization of energy, quality factors and RBE*. *Phys Med Biol*, 2016. **61**(16): p. 6231-42.
51. Hälgl, R.A. and U. Schneider, *Neutron dose and its measurement in proton therapy-current State of Knowledge*. *Br J Radiol*, 2020. **93**(1107): p. 20190412.
52. Schneider, U. and R. Hälgl, *The Impact of Neutrons in Clinical Proton Therapy*. *Front Oncol*, 2015. **5**: p. 235.
53. DeCunha, J.M., M. Newpower, and R. Mohan, *GPU-accelerated calculation of proton microdosimetric spectra as a function of target size, proton energy, and bounding volume size*. *Physics in Medicine & Biology*, 2023. **68**(16): p. 165012.
54. Liamsuwan, T., et al., *Microdosimetry of proton and carbon ions*. *Medical Physics*, 2014. **41**(8Part1): p. 081721.
55. Newpower, M., et al., *Using the Proton Energy Spectrum and Microdosimetry to Model Proton Relative Biological Effectiveness*. *Int J Radiat Oncol Biol Phys*, 2019. **104**(2): p. 316-324.

56. Lindborg, L., et al., *Lineal energy and radiation quality in radiation therapy: model calculations and comparison with experiment*. *Physics in Medicine & Biology*, 2013. **58**(10): p. 3089.
57. Kase, Y., et al., *Biophysical calculation of cell survival probabilities using amorphous track structure models for heavy-ion irradiation*. *Physics in Medicine & Biology*, 2008. **53**(1): p. 37.
58. Mairani, A., et al., *Optimizing the modified microdosimetric kinetic model input parameters for proton and (4)He ion beam therapy application*. *Phys Med Biol*, 2017. **62**(11): p. N244-n256.
59. Chattaraj, A. and T.P. Selvam, *Calculation of biological effectiveness of SOBPs proton beams: a TOPAS Monte Carlo study*. *Biomed Phys Eng Express*, 2024. **10**(3).
60. Magrin, G., et al., *State-of-the-art and potential of experimental microdosimetry in ion-beam therapy*. *Radiotherapy and Oncology*, 2023. **182**: p. 109586.
61. Underwood, T.S.A., et al., *A systematic review of clinical studies on variable proton Relative Biological Effectiveness (RBE)*. *Radiother Oncol*, 2022. **175**: p. 79-92.
62. Hagiwara, Y., et al., *Influence of dose-averaged linear energy transfer on tumour control after carbon-ion radiation therapy for pancreatic cancer*. *Clin Transl Radiat Oncol*, 2020. **21**: p. 19-24.
63. Molinelli, S., et al., *How LEM-based RBE and dose-averaged LET affected clinical outcomes of sacral chordoma patients treated with carbon ion radiotherapy*. *Radiother Oncol*, 2021. **163**: p. 209-214.

Appendix A – fluscw user routine

```

63   INCLUDE '(SCOHLP)'
64   INCLUDE '(TRACKR)'
65   INCLUDE '(FHEAVY)'
66   INCLUDE '(PAPROP)'
67   INCLUDE '(FLKMAT)'
68
69   LOGICAL LFIRST !! To only print first time
70   SAVE LFIRST
71   DATA LFIRST /.TRUE./
72
73   IF(LFIRST) THEN
74     WRITE(30,*) "user routine fluscw_Hedda called"
75     LFIRST = .FALSE.
76   ENDIF
77 !-----Energy scoring-----
78 !Heavier fragment than 4He
79   IF(IJ.LT.-6)THEN
80     AMPART = AMNHEA(-IJ)
81     IF(PLA.LT.ZERZER)THEN
82       EKPART=ABS(PLA)
83       PLA=SQRT(EKPART*(EKPART+TWOTWO*AMPART))
84     ELSE
85       EKPART = SQRT ( PLA**2 + AMPART**2 ) - AMPART
86     END IF
87
88     ! Proton or heavy fragment (avoiding IJ 0 and 1)
89   ELSEIF((IJ.EQ.1).OR.((IJ.LE.-2).AND.(IJ.GE.-6)))THEN
90     AMPART = AM(IJ) ! Rest energy
91     ! when negative, PLA is kin.energy:
92     IF(PLA.LT.ZERZER)THEN
93       EKPART=ABS(PLA) ! converting to positive
94       PLA=SQRT(EKPART*(EKPART+TWOTWO*AMPART))
95     ELSE
96       EKPART = SQRT ( PLA**2 + AMPART**2 ) - AMPART
97     END IF
98
99     ! Electrons, neutrons etc...
100    ELSE
101      AMPART = AM(IJ)
102      IF(PLA.LT.ZERZER)THEN
103        EKPART=ABS(PLA)
104        PLA=SQRT(EKPART*(EKPART+TWOTWO*AMPART))
105      ELSE
106        EKPART = SQRT ( PLA**2 + AMPART**2 ) - AMPART
107      END IF
108    END IF
109
110    ! Eventbin 22 is not multiplied:
111    IF((ISCRNG.EQ.2).AND.(JSCRNG.EQ.1)) THEN
112      FLUSCW = ONEONE
113    ! Eventbin 23 is to be multiplied with E:
114    ELSEIF((ISCRNG.EQ.2).AND.(JSCRNG.EQ.2)) THEN
115      FLUSCW = EKPART
116    ENDIF
117
118    LSCZER = .FALSE.
119    RETURN
120 *=== End of function Fluscw =====*
121    END

```

Figure A-1: The user routine fluscw_Hedda.f used for multiplying one of the fluence detectors (23) with the kinetic energy of the protons (EKPART).

Appendix B – interpolated $y_D(y)$

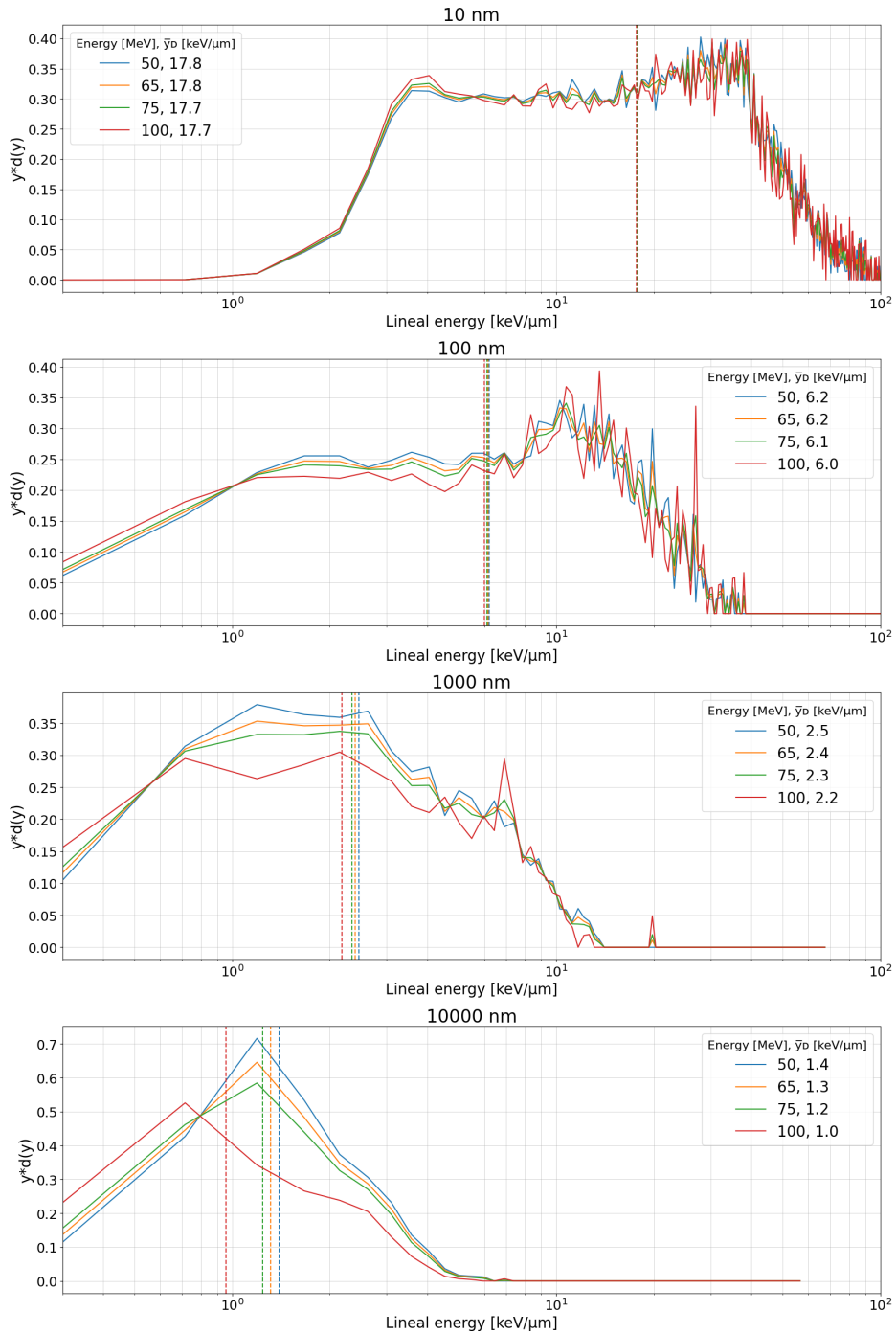


Figure B-1: $y_D(y)$ distributions for proton energies 50 - 100 MeV and site sizes 10nm - 10 μ m. The spectra for 20 and 50 MeV are from the GATE data and the two other spectra are interpolated from these. The y_D value of each spectrum is plotted as a vertical line.

Appendix C – python scripts and lookup tables

The python scripts and lookup tables developed in this project can be found on GitHub at this link: <https://git.app.uib.no/Hedda.Askheim/master-project-askheim.git>

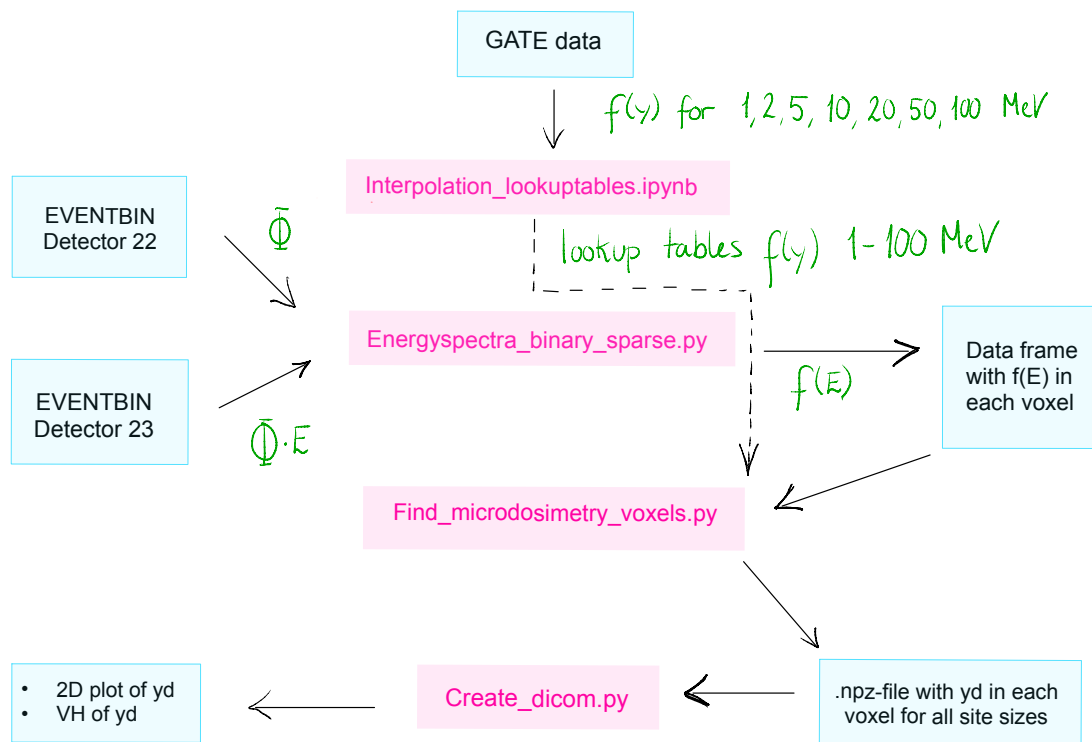


Figure C-1: Workflow between the scripts in this project.

Figure C-1 explains the workflow between the scripts. Here follows a short explanation of each script:

- *Interpolation_lookuptables.ipynb*: The GATE data is read and interpolation is performed to generate lookup tables.
- *Energyspectra_binary_sparse.py*: Read the files from the EVENTBIN detectors in the FLUKA simulation to create the energy spectrum ($f(E)$) in each voxel.

- *Find_microdosimetry_voxels.py*: Opens the data frame with $f(E)$ for each voxel and computes the microdosimetric quantities by using the lookup tables. The \bar{y}_D values for each voxel are saved as a numpy array. One .npz-file is saved containing the arrays for each site size.
- *Create_dicom.py*: Reads the .npz-file to insert the \bar{y}_D values in the DICOM images. Output DICOM files that can be used to plot the 2D distribution and the volume histograms of \bar{y}_D .